Angle-Resolved Photoemission Spectroscopy Studies of $Tl_2Ba_2CuO_{6+\delta}$ and $YBa_2Cu_3O_{7-\delta}$:

Analysis of recent results and the construction of a new system

by

Jeffrey Daniel Frederick Mottershead

B.Sc., The University of Alberta, 2001
M.Sc., The University of British Columbia, 2005

A THESIS SUBMITTED IN PARTIAL FULFILLMENT OF
THE REQUIREMENTS FOR THE DEGREE OF

DOCTOR OF PHILOSOPHY

in

The Faculty of Graduate Studies

(Physics)

THE UNIVERSITY OF BRITISH COLUMBIA

(Vancouver)

January, 2012

© Jeffrey Daniel Frederick Mottershead 2012

Abstract

Recent angle-resolved photoemission spectroscopy (ARPES) results, from experiments performed at the Swiss Light Source, Stanford Synchrotron Radiation Lightsource, and Advanced Light Source synchrotrons, on the high-temperature superconductors $Tl_2Ba_2CuO_{6+\delta}$ (Tl2201) and $YBa_2Cu_3O_{6.5}$ (YBCO6.5) are presented.

A very overdoped Tl2201 sample with a T_C of 30 K was found to have a Fermi surface, consisting of a large hole pocket centred at (π,π), which is approaching a topological transition. A superconducting gap consistent with a $d_{x^2-y^2}$ order parameter was detected. In contrast with the underdoped HTSCs, where the quasiparticle (QP) linewidth at the top of the band is maximal in the antinodal direction and minimal in the nodal direction, overdoped Tl2201 was revealed to have a reverse nodal-antinodal anisotropy, with sharp QP peaks in the antinodal region and broader peaks in the nodal region. The Tl2201 results establish Tl2201 as a valuable material for exploring the overdoped side of the phase diagram with ARPES.

Synchrotron experiments also yielded the first successful ARPES results on underdoped $YBa_2Cu_3O_{7-\delta}$ (YBCO), specifically on YBCO6.5. Surface-sensitive techniques were previously unsuccessful in studying YBCO because its cleaved surfaces are polar, resulting in an overdoped surface regardless of the doping level of the bulk. By doping the cleaved surfaces with potassium, the surface was progressively hole underdoped from as-cleaved continuously to the doping of the bulk, and subsequent ARPES experiments performed revealed a transition from a holelike Fermi surface on the as-cleaved surface to disconnected Fermi arcs when the surface doping matched the bulk.

In parallel with the synchrotron-based research, an in-house ARPES system was constructed at the University of British Columbia (UBC). Unlike conventional ARPES systems, the ARPES setup at UBC incorporates a molecular beam epitaxy (MBE) system, which allows novel materials to be grown, characterized, and transferred to the ARPES chamber in vacuo. Novel design tech-

niques to improve the accuracy of ARPES measurements are presented.

The in-house ARPES system also serves as a prototype for an ARPES–MBE endstation being constructed at the Canadian Light Source (CLS). Design studies of some potential improvements to the in-house system, to be implemented at the CLS, are also presented.

Preface

In this work I present photoemission experiments, done at synchrotrons, on two materials, $Tl_2Ba_2CuO_{6+\delta}$ (Tl2201) and $YBa_2Cu_3O_{6.5}$ (YBCO), as well as the design and commissioning of a new research system at UBC.

The Tl2201 and YBCO experiments consist of growing and characterizing the samples, measuring photoemission spectra at synchrotron and subsequent data analysis. Band structure calculations are also performed to compare with the measured spectra. All the work presented was done by the UBC Quantum Materials Group, to which I belong, and by the UBC Superconductivity Group. The UBC Quantum Materials Group is headed by Andrea Damascelli, and the UBC Superconductivity Group is headed by Walter Hardy and Doug Bonn. Both the Tl2201 and YBCO were grown by Ruixing Liang and Darren Peets. Band structure calculations for both systems were performed by Ilya Elfimov.

The Tl2201 measurements were done by Andrea Damascelli, Mauro Platé, and me. The subsequent analysis and manuscript preparation were led Andrea Damascelli and Mauro Platé, with the involvement of all coauthors.

I performed the potassium-doped measurements on YBCO. Suman Hossain and Andrea Damascelli led the data analysis and manuscript preparation, with the involvement of all coauthors.

The new system at UBC features a state-of-the-art cryostat and manipulator, a monochromatized light source with rotatable polarization and an advanced sample manipulation system.

The design of the cryostat was a joint project between Quantum Technologies and me, with Quantum Technologies concentrating on the helium circuit and me focusing on motion and coupling cooling power to the sample. The fabrication of the cryostat was split evenly between quantum technologies, the UBC Department of Physics machine shop and me.

I designed the vacuum chamber itself. Nicholas Ingle and I were the primary designers of the transfer system and hexapod ports used to align the transfer system.

The helium lamp and monochromator were designed and made by SPECS, and the motion stage for the monochromator was a joint project between SPECS and me.

This thesis contains text and figures adapted from previously published manuscripts.

Chapter 2 uses the following two papers:

"Fermi Surface and Quasiparticle Excitations of Overdoped Tl2201 by ARPES", *Phys. Rev. Lett.* **95** *(2005) 205114* by M. Platé, J. D. F. Mottershead, I. S. Elfimov, D. C. Peets, R. Liang, D. A. Bonn, W. N. Hardy, S. Chiuzbaian, M. Falub, M. Shi, L. Patthey, and A. Damascelli

"Tl2201 Brings Spectroscopic Probes Deep into the Overdoped Regime of the Cuprate HTSCs", *New Journal of Physics* **9** *(2007) 28*, by D. C. Peets, J. D. F. Mottershead, B. Wu, I. S. Elfimov, R. Liang, W. N. Hardy, D. A. Bonn, M. Raudsepp, N. J. C. Ingle and A. Damascelli

Chapter 3 uses the following paper:

"In situ doping control of the surface of high-temperature superconductors", *Nature Physics* **4** *(2008) 527* by M. A. Hossain, J. D. F. Mottershead, D. Fournier, A. Bostwick, J. L. McChesney, E. Rotenberg, R. Liang, W. N. Hardy, G. A. Sawatsky, I. S. Elfimov, D. A. Bonn and A. Damascelli

Table of Contents

List of Figures

List of Symbols

$\Gamma-$point	the origin in momentum space
ϵ	electron energy before excitation
ω	binding energy
A	distance from analyzer hemisphere centre to slit
$A(\mathbf{k}, \omega)$	spectral function
E_F	Fermi energy
E_{pass}	pass energy
$f(\omega)$	Fermi function
$I(\omega)$	photoemission intensity as a function of binding energy
k	electron momentum
$k_{\|\|}$	electron momentum parallel to the sample surface
k_F	Fermi momentum
k_x	electron momentum projected along $\hat{x}$
k_y	electron momentum projected along $\hat{y}$
k_z	electron momentum projected along $\hat{z}$
T	temperature
T_C	critical temperature
U	potential energy
v_F	Fermi velocity

Glossary

1D	one-dimensional
2D	two-dimensional
316	designation of an ultra-high-vacuum compatible stainless steel alloy
6061-T6	designation of an ultra-high-vacuum compatible aluminum alloy
AC	alternating current
AFI	antiferromagnetic insulator
AFM	atomic force microscopy
ALS	Advanced Light Source
AMRO	angular magnetoresistance oscillations
ARPES	angle-resolved photoemission spectroscopy
BCS	Bardeen-Cooper-Schrieffer
BHRSS	model number of magnetic transfer arm made by Transfer Engineering
Bi2201	$Bi_{2+x}Sr_{2-x}CuO_{6+\delta}$
Bi2212	$Bi_{2+x}Sr_{2-x}CaCu_2O_{8+\delta}$
BZ	Brillouin zone
CCD	charge-coupled device
CLS	Canadian Light Source
CNC	computer numeric control
DC	direct current
EDC	energy-dispersion curve
ErLEED	LEED instrument manufactured by SPECS
FS	Fermi surface
FS_{AB}	Fermi surface from the antibonding bands
FS_B	Fermi surface from the bonding bands
FS_{Ch}	Fermi surface from the copper-oxygen chain bands
FWHM	full-width half-maximum

HAAS	a brand of machine tool
HTSC	high-T_C superconductor
LCAO	linear combination of atomic orbitals
LDA	local density approximation
LDOS	local density of states
LEED	low-energy electron diffraction
LEM	leading-edge midpoint
LSCO	$La_{2-x}Sr_xCuO_4$
MBE	molecular beam epitaxy
MCP	microchannel plate
MDC	momentum-dispersion curve
ortho-I	an ordering of YBCO
ortho-II	an ordering of YBCO with alternating full and vacant oxygen sites
PES	photoelectron spectroscopy
Phoibos 150	an electron analyzer manufactured by SPECS
QMSC	Quantum Materials Spectroscopy Centre
QP	quasiparticle
R4000	an electron analyzer manufactured by Scienta
RHEED	resonant high-energy electron diffraction
SAES	manufacturer of getter pumps
SC	superconductor
SCP	superconducting peak
SES-2002	an electron analyzer manufactured by Scienta
SIS	Surface and Interface Spectroscopy beamline
SLS	Swiss Light Source
SPECS	manufacturer of surface-science equipment
SSRL	Stanford Synchrotron Radiation Lightsource
STM	scanning tunnelling microscopy
STS	scanning tunnelling spectroscopy
Ti-6Al-4V	designation of a titanium alloy
Tl2201	$Tl_2Ba_2CuO_{6+\delta}$
Tl2201-OD30	an overdoped sample of $Tl_2Ba_2CuO_{6+\delta}$ with a T_C of 30 K
Tl2201-OD63	an overdoped sample of $Tl_2Ba_2CuO_{6+\delta}$ with a T_C of 63 K
Tl2201-OD74	an overdoped sample of $Tl_2Ba_2CuO_{6+\delta}$ with a T_C of 74 K
UBC	University of British Columbia
UHV	ultra-high vacuum

UNS C10200	a designation of high-purity copper
YBCO	$YBa_2Cu_3O_{7-\delta}$
YBCO6.5	$YBa_2Cu_3O_{6.5}$
YBCO7.0	$YBa_2Cu_3O_{7.0}$
YBCOK1	a $YBa_2Cu_3O_{6.5}$ sample after one deposition of potassium
YBCOK2	a $YBa_2Cu_3O_{6.5}$ sample after one deposition of potassium

Acknowledgements

I would like to thank my supervisor, Dr. Andrea Damascelli, for his patience and dedication along the long and circuitous path I took with my studies. The opportunity to set up a lab space in what was an empty room was a very valuable and enjoyable learning experience. The chance to work in a variety of synchrotrons was also a unique and formative experience. I learned a great deal on a wide variety of topics, including my psychology [1, 2], from Dr. Damascelli as the nature of our work moved from lab building, to instrument construction, to scientific experimentation.

Ruixing Liang and Darren Peets grew all the samples that were used in this work. On top of the obvious importance of making samples of the highest quality readily available, Darren and Ruixing provided support after handing over the crystals, such as re-annealing after the samples had been glued to sample holders.

I owe Dr. Nicholas Ingle a great deal as well. On several occasions throughout my research I've found myself in a state of confusion trying to make sense of the theory relating to high-T_C superconductors because I was missing one or more prerequisite concepts. Dr. Ingle was always able to ask the questions he needed to in order to identify what I was missing and then give a well-structured explanation starting with the missing fundamentals and building every dependent concept on top of them to construct a solid understanding.

I would also like to thank my thesis committee of Dr. Doug Bonn, Dr. David Jones and Dr. Jess Brewer both for their patience during the seemingly interminable period of me being almost done and for their comments and suggestions, which improved the dissertation a great deal.

My wife, Iva Cheung, has been a tremendous support throughout the entire process. She has endured periods when I was spending an awful lot of time in the lab, has provided consistent moral support when things didn't seem to be progressing, and has been of great assistance editing my thesis and helping me with figures.

Scott Webster was of tremendous help whenever I was having any sort of issue involving a computer. He deserves some sort of trophy. When deadlines were approaching and the thesis was not compiling, he made several late-night house calls. I should buy him a cheeseburger.

Chapter 1

Introduction

Since high-temperature ceramic superconductors were discovered in 1986 [3], they have attracted attention both because of their potential technological uses and because they presented a scientific challenge. The Bardeen-Cooper-Schrieffer (BCS) theory, which satisfactorily explains superconductivity in Fermi liquid–like metals, does not have the correct starting assumptions to model the high-T_C superconductors (HTSCs). A theory of the HTSCs has been elusive, despite a long-term effort, owing to the difficulty inherent in modelling the strong electron-electron interactions present in these materials. The presence of these interactions makes the goal of finding a model for the HTSCs part of a larger objective—that being the construction of a model that explains the properties of systems with strong electron-electron interactions. Despite a strong effort for many years, however, there is no consensus on a theoretical model for the HTSCs, partially because of the fact that strong electron-electron interactions present a difficult system to model and partially for lack of a material family that can be grown at all doping levels that exhibit superconductivity and that does not have other material issues that complicate measurement; thus, forming a coherent picture of the experimental results is difficult. $Tl_2Ba_2CuO_{6+\delta}$ (Tl2201) and $YBa_2Cu_3O_{6.5}$ (YBCO6.5) offer an opportunity to do angle-resolved photoemission spectroscopy (ARPES) studies on materials that have high T_Cs, but, unlike the materials already extensively studied by ARPES, they are also sufficiently clean that they are suited to treatment as clean crystals, allowing measurements that require a long mean free path, such as quantum oscillations. Tl2201 can be grown from near-optimal doping to very overdoped, while YBCO is underdoped. Study of Tl2201 and YBCO allows ARPES data to be directly compared with transport measurements and allows the problem of high-T_C superconductivity to be approached from the two extremes: a Fermi-liquid on the very overdoped side and a charge transfer insulator on the very underdoped side. This thesis presents ARPES measurements taken to determine the Fermi surface, electronic dispersion, and superconducting gap of Tl2201 and YBCO6.5.

ARPES results from work done at the Swiss Light Source (SLS), using the Surface and Interface Spectroscopy (SIS) beamline; at the Stanford Synchrotron Radiation Lightsource (SSRL), at Beamline 5-4; and at the Advanced Light Source (ALS), on the Electronic Structure Factory endstation, are presented. In parallel with the work done at the synchrotrons, a new in-house ARPES system was constructed. The goals of the new ARPES system are two-fold: as well as achieving lower temperatures and higher resolution than the existing state of the art, we also are connecting a molecular beam epitaxy (MBE) system to our ARPES chamber, such that we can do ARPES studies of materials that either cannot be grown as crystals or do not cleave well enough to be studied by ARPES through conventional means. The in-house ARPES system is not only a valuable research tool in and of itself but also serves as a prototype for an ARPES system being constructed for the Quantum Materials Spectroscopy Centre (QMSC) at the Canadian Light Source (CLS). Design studies of potential refinements upon the in-house system for implementation at the CLS are presented.

1.1 Correlated systems

The physics of simple metals, semiconductors, and many ionic compounds is understood and modelled successfully by calculating the behaviour of free electrons interacting with a periodic potential of atomic nuclei and the average electronic density [4]. Theoretical modelling of these materials agrees well with measurements and can be used to predict an impressive array of properties, such as thermal conductivity, AC and DC electrical conductivity, the Hall coefficient, and magnetoresistance, to name a few. Elementary calculations of these quantities rest heavily on the free-electron approximation, and corrections due to electron-electron interactions are handled perturbatively [4].

At the other end of the spectrum, we are able to accurately model molecular chemistry in the paradigm of bound electrons [5]. Hybridization of molecular electronic orbitals provides a reliable method for computing electronic states in organic molecules.

Between these two canonical regimes, however, there is a wide range of materials that have electrons that are not bound to specific lattice sites but do interact heavily with each other. These materials, known as correlated systems, have a staggering range of properties that are unexpected on the basis of the independent particle picture, and these properties can change dramatically with

small changes in doping, lattice constants, temperature, and pressure, as a result of electron-electron and electron-phonon interactions giving rise to many different competing phases. While these interactions are responsible for the broad range of properties in correlated systems, their presence makes calculations notoriously difficult. Owing to the presence of strong correlations, calculations of the properties of these materials are inherently many-body problems, with no universally applicable technique for simplifying them. In order to effectively model the electron-electron interactions, an experimental model for the spectral function is needed, making spectroscopic studies of these materials one of the main thrusts of the current experimental effort.

1.2 The cuprates

Among correlated systems, the transition metal oxides stand out in particular, as they exhibit dramatic changes in properties with small changes in tunable parameters such as temperature, interatomic spacing, or doping.

Two-dimensional copper-oxide superconductors (cuprates) are of special interest, as they change from being antiferromagnetic insulators to HTSCs and finally to non-superconducting metals, ostensibly Fermi liquids, as a function of doping (see Figure 1.1). Common to all cuprate superconductors is a CuO_2 square plane; the band structure of this plane is where the superconducting gap opens.

From an atomic orbital perspective, in the cuprates, the $3d$ valence electrons overlap and hybridize with the oxygen $2p$ orbitals. Each $3d$ orbital neighbours four $2p$ orbitals, and each $2p$ orbital neighbours two $3d$ orbitals. Neighbouring $3d$ states can interact with each other through two nearest-neighbour hoppings mediated by the intermediate $2p$ orbital. Long-range interactions are mediated by many nearest-neighbour hoppings and hence depend on the hopping strength to a high order. Thus, with small changes in the material, arising from doping, temperature changes, applied fields, pressure, and in the case of thin films grown on a substrate, epitaxial strain, the $2p$–$3d$ states can vary from being predominantly localized to predominantly itinerant. Through this transition, a wide variety of competing orders are seen, which correspond to the different states seen in the cuprate phase diagram.

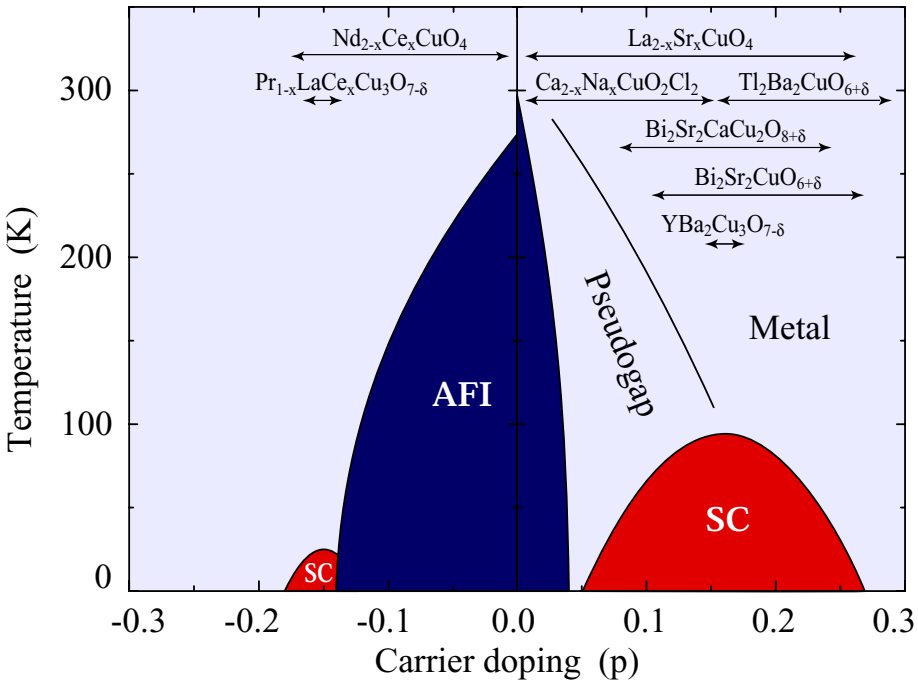

Figure 1.1: Generic temperature-doping phase diagram for both electron- ($p<0$) and hole-doped ($p>0$) cuprates. At low doping the system is an antiferromagnetic insulator (AFI), and at intermediate doping it is a superconductor (SC). The doping range actually explored by ARPES for those material families more extensively studied is indicated by the corresponding arrows [6].

1.3 Angle-resolved photoemission spectroscopy

While many different types of measurements have made important contributions to our understanding of the HTSCs [7], ARPES gives the most direct measurement of the momentum-resolved electronic structure, which contains spectral weight away from the bands that non-interacting electron calculations predict. This spectral weight is a direct consequence of many-body interactions; therefore, ARPES is a useful tool in an attempt to understand these interactions. To a first approximation, the copper d-electron states responsible for superconductivity have no dispersion perpendicular to the CuO_2 plane. Thus, the d-electrons can be thought of as two-dimensional (2D), making them ideal for studies by ARPES, in which the components of electron momentum parallel to the surface are conserved during photoemission, while the component perpendicular to the surface is more difficult to access. The perpendicular component can be reached by ARPES by repeating the measurements over a range of photon energies [8].

The simplest model of photoemission is as follows: a photon of known energy promotes an electron of a given energy ϵ and momentum k to a state with the same momentum k and an energy $\epsilon + \hbar\omega$. In what is known as the sudden approximation, the electron is assumed to immediately exit the surface of the material, without interacting with the photohole it leaves, thereby losing ϕ, the work function, from its energy, giving the electron a final energy of $\epsilon + \hbar\omega - \phi$. As the electron leaves the material, the momentum parallel to the surface of the sample is conserved, but the momentum perpendicular to the sample is not conserved, owing to a lack of symmetry. The fact that the momentum is not conserved in the perpendicular direction is not a problem in the analysis of 2D electrons, however, where there is no electronic dispersion perpendicular to the surface of the sample. By measuring the photoelectron energy, and the angle of emission, from which the parallel component of momentum is readily calculable, the electronic dispersion of a 2D material can be readily determined. The electronic structure of the CuO_2 band, thought to be responsible for superconductivity in the cuprates, is sufficiently close to 2D that it is often treated as 2D. As well as having a quasi-2D electronic structure, the cuprates further lend themselves to ARPES studies, as they naturally cleave parallel to the CuO_2 planes. Thus, ARPES data yield direct information about the single-particle spectral function for occupied states, and hence ARPES is a valuable and unique tool for determining the electronic origins of the exotic properties found in the cuprates.

Within the sudden approximation, ARPES probes the energy and momentum dependence of the electronic excitation spectrum of an $N-1$ particle system, the so-called electron-removal portion of the single-particle spectral function $A(\mathbf{k},\omega)$ [9]. In the non-interacting picture, this spectral function consists of delta-function peaks located at the precise energy and momentum given by the band structure, i.e. $A(\mathbf{k},\omega)=\delta(\omega-\epsilon_{\mathbf{k}})$. When interactions are considered, the single-particle spectral function is modified by the inclusion of the electron proper self energy $\Sigma(\mathbf{k},\omega)=\Sigma'(\mathbf{k},\omega)+i\Sigma''(\mathbf{k},\omega)$, which captures all of the many-body correlation effects. One can then write

$$A(\mathbf{k},\omega)=-\frac{1}{\pi}\frac{\Sigma''(\mathbf{k},\omega)}{[\omega-\epsilon_{\mathbf{k}}-\Sigma'(\mathbf{k},\omega)]^2+[\Sigma''(\mathbf{k},\omega)]^2}. \tag{1.1}$$

With respect to the non-interacting case, the peaks in the spectral function shift in energy and gain a finite width, in a manner dependent on the energy and momentum of the excitations. At those ω and k for which the spectral function is still characterized by a single pole, energy and lifetime renormalization are directly described by $\Sigma'(\mathbf{k},\omega)$ and $\Sigma''(\mathbf{k},\omega)$, respectively. The ARPES lineshape thus gives direct access to the lifetime of the excitation and can provide insights into the nature of the underlying interactions—for example, whether or not electron-electron interactions are Fermi liquid–like.

It is important to note that while ARPES gives a relatively direct probe of the single-particle spectral function, ARPES intensity is not equivalent to the single-particle spectral function. Putting aside resolution and temperature effects, the ideal ARPES intensity would be proportional to the spectral function only if the probability of the incoming photon exciting an electron were constant for all electrons, which is not the case. The ARPES intensity for a single-band system depends linearly on both the spectral function and the probability of the light promoting electrons in the initial state to the final state allowed by energy and momentum conservation. This probability is given by $\langle(\psi_f)^{\mathbf{k}}|H_{int}|(\psi_i)^{\mathbf{k}}\rangle$, where ψ_f is the final state of the photoelectron, ψ_i is the initial state and H_{int} is the interaction Hamiltonian for the electron and the photon.

Under the assumption that the vector potential, $\mathbf{A}$, is constant over atomic dimensions, in the Coulomb gauge, $H_{int}=-\frac{e}{m}\mathbf{A}\cdot\mathbf{p}$. The one-electron matrix element under the dipole approximation is now $\langle(\psi_f)^{\mathbf{k}}|H_{int}|(\psi_i)^{\mathbf{k}}\rangle$, denoted ${M_{f,i}}^{\mathbf{k}}$. Wherever the matrix element is zero, the photoemission spectrum will be completely suppressed. Matrix element effects need to be considered when

choosing the photon energy and especially the polarization, and to extract the spectral function from the data, the matrix elements must be calculated.

Note that the simple model described above does not take into account scattering or surface effects. For a more complete model of the photoemission process, see Hüfner [8], and for a review of ARPES on the cuprates, see Damascelli et al. [6].

1.4 $Tl_2Ba_2CuO_{6+\delta}$ as a material for ARPES studies

Certain families of cuprates, particularly $Bi_{2+x}Sr_{2-x}CuO_{6+\delta}$ (Bi2201), its bilayer cousin $Bi_{2+x}Sr_{2-x}CaCu_2O_{8+\delta}$ (Bi2212), and $La_{2-x}Sr_xCuO_4$ (LSCO) have been extensively studied by ARPES. While these studies have produced many valuable results [6], they have been complicated by material issues. Bi2201 and Bi2212, for instance, are standard materials for ARPES studies because they cleave very easily and thus offer ready access to a vacuum-clean surface on which to do photoemission work, but from a theoretical modelling perspective, they are not ideal: when investigating Bi-based cuprates, one is faced with the choice of studying either the single-layer compound Bi2201, which has a low T_C, or Bi2212, which has a much higher T_C but also has the problem of being a bilayer compound in which there is interlayer coupling between neighbouring CuO_2 planes, complicating both analysis of the ARPES spectra and the theoretical modelling of the compound. Furthermore, Bi2201 and Bi2212, due to their short mean free path, are not well suited to bulk-sensitive measurements, complicating the comparison of cuprate data from complementary techniques. LSCO is doped by substituting strontium for lanthanum, and thus the ions near the CuO_2 planes change as a function of doping. Also, the short mean free path of LSCO makes it not well suited to bulk-sensitive techniques. The requirement for long mean free paths is discussed by Ashcroft and Mermin [4].

The thallium compound $Tl_2Ba_2CuO_{6+\delta}$ (Tl2201) presents a unique opportunity to understand the physics of high-temperature superconductivity while sidestepping many material issues. Tl2201 is a single-layer compound with a very high T_C of 93 K at optimal doping [10] and can be grown with a clean crystal structure over a broad doping range. Tl2201 can be grown in the heavily overdoped side of the phase diagram, where very little ARPES work has been done. Further, Tl2201 has been studied by angle-dependent magnetoresistance

oscillations (AMRO) [11], allowing a direct comparison between bulk-sensitive and ARPES results.

Tl2201 has not been studied by ARPES extensively because of technical difficulties. At the required temperatures for growing Tl2201 crystals, the highly toxic TlO has a significant vapour pressure. Despite the hazards inherent in its growth, Tl2201 has been synthesized, but attempts at ARPES studies have been stymied by the fact that even void- and flux-free single crystals of the material are difficult to cleave. However, the unique opportunity provided by Tl2201 justifies the effort needed to overcome these difficulties. In this thesis, Tl2201 ARPES data taken at the SLS on the SIS beamline, as well as data taken at the SSRL, are presented.

1.5 $YBa_2Cu_3O_{6.5}$ as a material for ARPES studies

$YBa_2Cu_3O_{7-\delta}$ (YBCO) can be doped continuously from $\delta = 0$ to $\delta = 1$, although only some dopings will offer the possibility of stoichiometric ordered states. When $\delta = 1$, all oxygen sites in the copper chains are filled, yielding a nearly perfect ortho-I state. For $\delta = 0.5$, the YBCO6.5 sample can be annealed to yield an ordered (ortho-II) state of alternating full and empty CuO chains. The ortho-II state has a T_C of 62 K, 5 K higher than the quenched ortho-I state of the same oxygen content [12].

As YBCO is free of cation disorder, it is well suited for study by bulk-sensitive techniques. These studies detected de Haas–van Alphen and Shubnikov–de Haas quantum oscillations in oxygen-ordered ortho-II YBCO6.5, which indicate the existence of hole and/or electron pockets of 1.9% of the full Brillouin zone [13, 14, 15].

However, ARPES (and other surface-sensitive) studies of YBCO have previously been hampered by the fact that the material lacks a natural [001] cleavage plane and produces polar surfaces when cleaved.

The most basic model of the polar surface is a system with alternately charged layers. A cleave between any two layers will result in a diverging electric potential (see Figure 1.2). The polar surface problem is further discussed and illustrated by Nakagawa et al. [16].

YBCO cleaves on either side of the charged copper-oxygen chain layers, resulting in a polar surface and subsequent self-doping of the YBCO surface

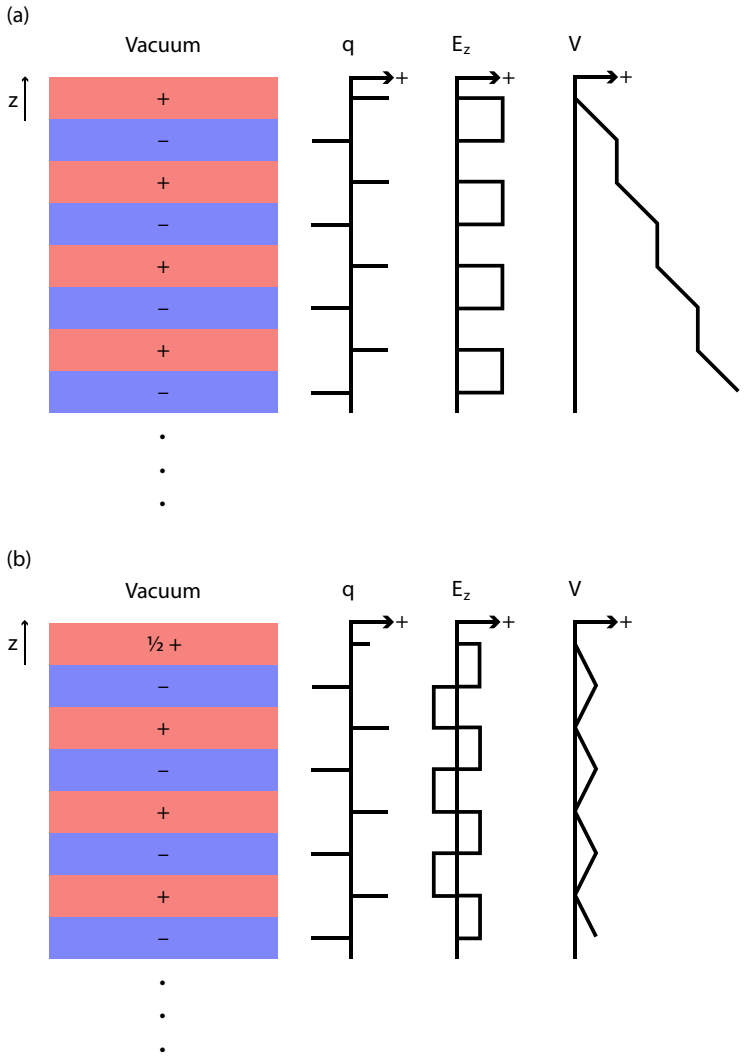

Figure 1.2: (a) The system of alternating charges lacks a natural cleavage plane. Cleaving between layers results in a diverging electric potential. (b) A change of the surface charge results in a non-diverging potential.

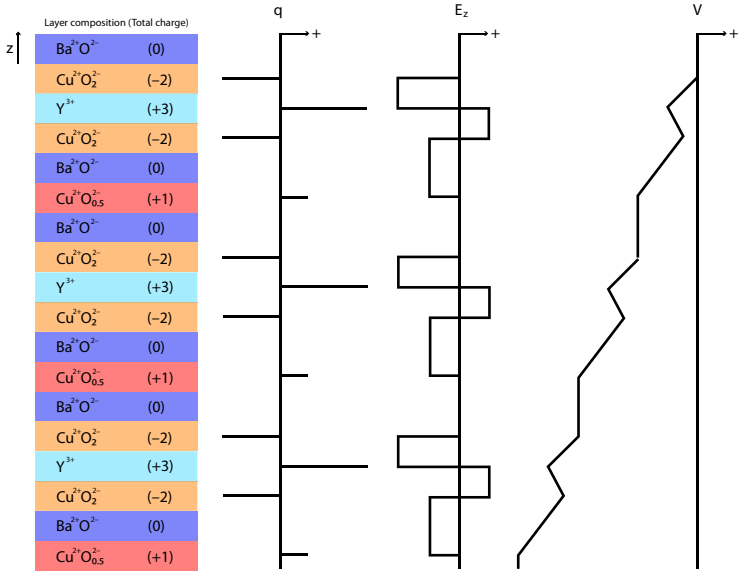

Figure 1.3: YBCO cleaves on either side of the $CuO_{1-\delta}$ chain layer. At photon energies used in ARPES, the mean free path of the photoelectrons is sufficiently short that the spectra of the CuO_2 planes is not detected for portions of the cleave where the $CuO_{1-\delta}$ chain layer is on the surface. We thus consider the cleaved surface where the $CuO_{1-\delta}$ chain layer is removed. Without charge reconstruction the electric potential of the system would diverge to $-\infty$.

(see Figure 1.3. For comparison, Tl2201 has a does not have a polar surface problem and has natural cleavage plane (see Figure 1.4).

By in-situ deposition of potassium atoms on cleaved YBCO, we can continuously control the surface doping and follow the evolution of the Fermi surface from the overdoped to the underdoped regime (see Figure 1.5). To the best of our knowledge, this was the first application of surface transfer doping [17] either to cuprates or to materials affected by polar cleaved surfaces. This approach opens the door to new systematic studies of high-T_C cuprates, such as creating new electron-doped superconductors from insulating parent compounds.

This thesis presents ARPES data taken on YBCO6.5 at the Electronic Structure Factory at the ALS.

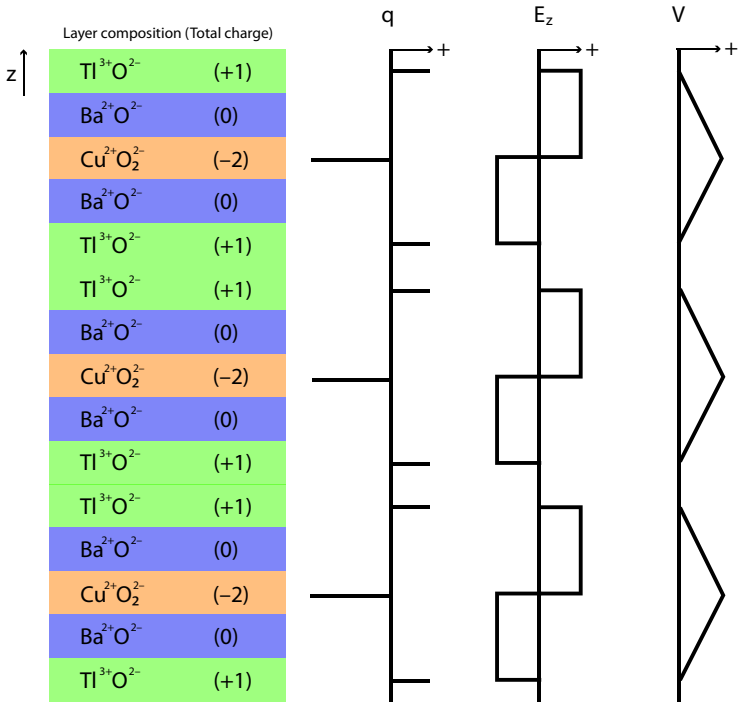

Figure 1.4: Tl2201 has a natural cleavage plane. The material cleaves between TlO layers and gives a non-diverging potential without self-doping.

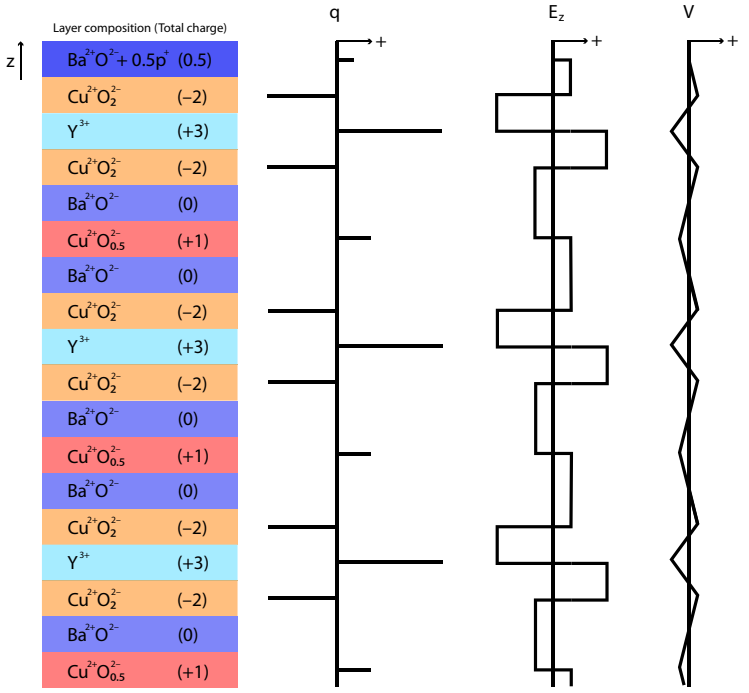

Figure 1.5: Charge accumulates on the cleaved surface to give a non-divergent potential. In the case of a cleave that removes the $CuO_{1-\delta}$ chain layer, the result of the charge reconstruction is hole doping. Alternatively, deposition of potassium, an electron donor, can solve the polar surface problem. Potassium deposition can reverse the self-doping. Potassium absorbs the holes, thereby forming K^+ ions. This does not change the surface charge, but holes are removed from the band structure. Potassium doping can thus be used to set the hole doping to that of the bulk, or to other values as desired.

1.6 Construction of an in-house ARPES system

In addition to studying Tl2201 and YBCO6.5, we have developed a new in-house ARPES system at UBC. While developments in electron analyzers have allowed measurements of higher and higher angular and energy resolution, these advances have made the requirements on the surrounding chamber more demanding.

Modern electron analyzers typically have ultimate resolutions of a few meV and 0.2° [9]. Typical ARPES experiments are done at significantly lower resolutions, though. When selecting operating parameters, there is a trade-off between angular and energy resolution. Furthermore, count rates drop precipitously as resolution is increased. As a result, typical ARPES experiments are done with energy resolutions at or above 10 meV.

The resolution of an ARPES system is distinct from that of the electron analyzer. The resolution of the system also depends on stray fields inside the system, the light source. Doppler broadening from a helium lamp typically gives a 1 meV width, while synchrotron light sources are limited by the resolution of their monochromators, which are normally more than 1 meV. Helium lamps typically have spot sizes 500 μm and up, while 100 μm is not atypical for a synchrotron.

The sample temperature does not affect the system resolution, but increasing the sample temperature broadens the spectral features, and as such sample temperature affects the ability to resolve spectral features of a sample in a similar manner to other resolution effects. Modern ARPES cryostats with more than one angular degree of freedom typically have minimum sample temperatures from 10 K to 25 K.

Like sample temperature, sample surface contamination does not affect the resolution, but the contamination can broaden features. ARPES is normally done with photon energies between 10 eV to 100 eV. The resulting photoelectrons have a very short mean free path (see Figure 1.6), corresponding to only a few atomic monolayers, and as a result even a sub-monolayer of contaminants can have a large effect by affecting the electronic and atomic structure of neighbouring layers. Contamination thus decreases the ability to distinguish spectral features. Surface contamination can also reduce signal strength and even affect the electronic structure of the sample. The rate at which a sample surface ac-

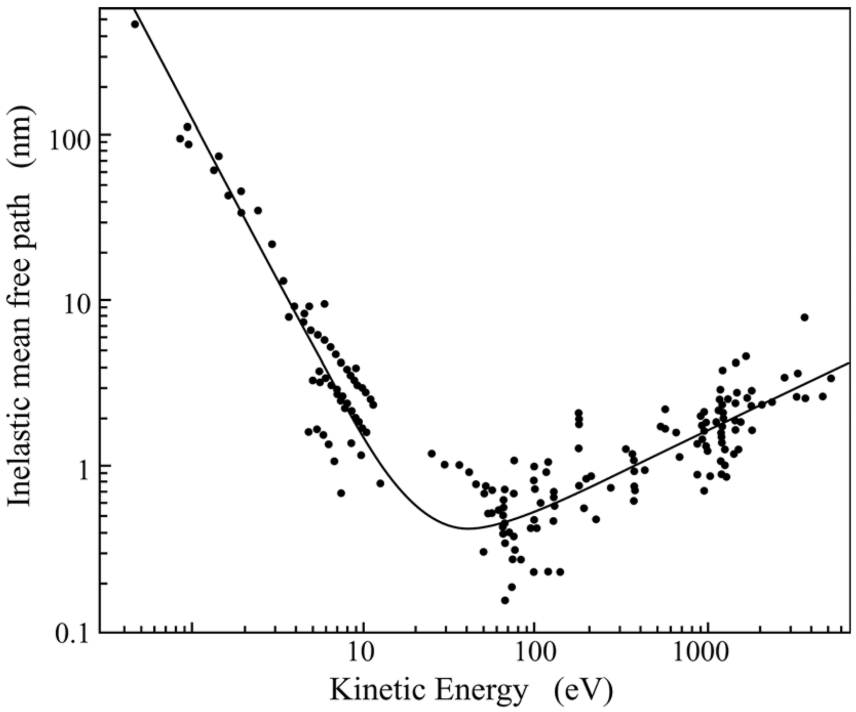

Figure 1.6: "Universal curve" of inelastic mean free path of electrons in solids as a function of kinetic energy (from [18]). For reference, Tl2201 has a $c-$axis lattice constant of 2.32 nm [19].

cumulates contamination is directly proportional to the pressure in the system. A vacuum of 5×10^{-11} mbar normally allows a sufficient sample lifetime to do ARPES experiments.

In order for the UBC ARPES system to capitalize on the increased resolution of modern electron analyzers, stray electric and magnetic fields in the chamber have to be correspondingly lower, the angular positioning of the sample has to be at least as accurate as the angular resolution of the analyzer, and cryostat temperatures and chamber pressures have to be lower. While each of these design goals by itself does not present a major challenge, accomplishing them all in the same system presents many unique difficulties. As well as achieving a new level of resolution and a new low for sample temperatures in a movable cryostat, the new system has the unique advantage of being coupled to a small

MBE, which is used to grow samples and pass them in vacuo to the ARPES system, broadening the scope of ARPES from the narrow set of samples that cleave readily to the very broad range of substances that can be grown by MBE. Furthermore, by growing on substrates of varying lattice constants, the interatomic distance of the material being studied can be adjusted, giving another degree of freedom on top of doping and temperature that can be used to tune the physical properties of the system under study. A further feature of the new system is that the linear polarization of the light source can be rotated, allowing us not only to see spectral features that may otherwise be missed as a result of matrix element effects but also to exploit these same matrix element effects to differentiate between overlapping spectral features. Novel design techniques implemented in the construction of the system, as well as results from preliminary testing, are presented.

1.7 Canadian Light Source ARPES Recommendations

The CLS is a fairly new synchrotron in Saskatoon, Saskatchewan. The Quantum Materials group at UBC is building the Quantum Materials Spectroscopy Centre (QMSC) at the CLS, which will consist of a beamline and endstations to study correlated systems. The QMSC will incorporate MBE systems for growth of oxide and organic films, a comprehensive set of diagnostic tools, and two ARPES systems—one with a conventional CCD detector and the other with a spin-sensitive detector.

The in-house ARPES system developed at UBC is not only an important research tool in and of itself, but it also serves as a prototype for the QMSC ARPES chambers. The smaller spot size of the synchrotron beam allows for the study of smaller and more challenging samples, but only if the mechanical accuracy of the cryostat motion is sufficiently improved to allow the beam to stay on the sample as the cryostat is moved. Alternatively, an arrangement where the analyzer moves instead of the cryostat significantly relaxes the tolerances needed, as the analyzer focus is an order of magnitude larger than the beam spot size. Design studies of both approaches are presented.

Chapter 2

ARPES on $Tl_2Ba_2CuO_{6+\delta}$

Despite a growing body of ARPES measurements of various families of cuprate superconductors and many intriguing results, profound disagreements as to the meaning of many of these results prevail [6]. Above and beyond the theoretical challenge of modelling correlated electrons, much of the difficulty comes from material issues of various types. Only a few of the known families of cuprates cleave sufficiently cleanly to allow ARPES measurements on crystals. Of the families that have been studied by ARPES, there are family-specific problems.

The bulk of ARPES studies to date have focused on $Bi_{2+x}Sr_{2-x}CuO_{6+\delta}$ (Bi2201), $Bi_{2+x}Sr_{2-x}CaCu_2O_{8+\delta}$ (Bi2212), and $La_{2-x}Sr_xCuO_4$ (LSCO). Each of these materials has provided valuable results, but in each family, complexities unrelated to superconductivity are present in the band structure, and the fact that these materials grow non-stoichiometrically has obscured a theoretical interpretation [6, 20].

Producing high-quality cleaved surfaces in LSCO is difficult, making ARPES studies challenging, and the presence of lattice distortions and spin/charge instabilities creates complications in the electronic structure of the material, which are difficult to divorce from the signatures of superconductivity [6]. Further, LSCO is difficult to grow without introducing chemical inhomogeneity. The substitutions have a strong effect on superconductivity, as the site of the substitution neighbours the CuO_2 plane.

In Bi2212, superstructure modulations with a periodicity of 27Å make the unit cell five times larger than the unit cell would be in the absence of the superstructure modulations, and hence its corresponding Brillouin zone (BZ) is one-fifth the size of the BZ of a modulation-free crystal. However, researchers focus on the latter, larger BZ, as the smaller zone's features are too faint to prove useful for analysis, and as a result they see not only the Fermi surface (FS) but also faint FS replicas. These are known as the umklapp bands [6]. Further, Bi2212 has shadow bands—FS replicas shifted by $(\pi/2,\pi/2)$, which are caused by an orthorhombic distortion [21]. Also, Bi2212 has bilayer band-splitting, which

is caused by the electronic structure of the neighbouring CuO_2 planes splitting into bonding and antibonding bands. The presence of bilayer splitting, umklapp bands, and shadow bands often obscures the analysis of ARPES spectra of Bi2212. In many instances, it is difficult to determine whether features observed are genuinely features related to superconductivity or merely consequences of the complications in the structure of Bi2212. Finally, Bi2212 grows best at optimal doping but is difficult to synthesize over a broad doping range, especially in the overdoped regime, making studies of the evolution of properties over the entire phase diagram difficult.

Bi2201 is a single-layer compound and thus does not exhibit the bilayer splitting present in Bi2212. That said, Bi2201 does not have a high T_C, a fact that likely makes the hallmarks of superconductivity less apparent. The umklapp and shadow bands are still present as in Bi2201, and like Bi2212, it can only be easily grown over a limited doping range. Overdoped Bi2201 is not readily synthesized.

In contrast, $Tl_2Ba_2CuO_{6+\delta}$ (Tl2201) has a number of properties that make it ideal for photoemission studies. Tl2201 is a single-layer compound, so there is no bilayer splitting. Tl2201 is doped through addition of interstitial oxygen and Cu substitution on the Tl sites. Tl2201 can be grown over a broad doping range and thus presents a unique opportunity to do ARPES measurements on a single compound, from optimally doped to highly overdoped, where there are indications that the normal state is a Fermi liquid [22]. Although understanding the transition from the superconducting state to a zero-temperature metallic state is likely critical for a theory of high-T_C superconductivity, very little ARPES research has been done on this part of the phase diagram, as LSCO suffers from cation disorder [20] at higher dopings. Cation substitution is used as a means of doping LSCO, complicating the photoemission spectra. However, cation disorder is not nearly as problematic in Tl2201, where the disorder is manifested as non-stoichiometric oxygen doping and Cu-Tl substitution, both occurring in the TlO planes, far from the CuO_2 planes. Moreover, Cu-Tl substitutions are not the sole means of doping; hence, changes in the spectra observed as a function of doping can be distinguished from cation disorder effects. Thus, Tl2201 is an ideal candidate for ARPES studies at higher dopings. The crystal structure is well ordered, with flat, distantly spaced CuO_2 planes. This reduced disorder may be the reason Tl2201 has a T_C of 93 K at optimal doping, which is among the highest of single-layer compounds [20].

Although little ARPES work has been done on Tl2201 until now, signifi-

cant results have been achieved via other experimental techniques. Neutron diffraction has revealed that the non-stoichiometric oxygen is located between the TlO layers [23]. The fact that the non-stoichiometric oxygen is isolated from the CuO_2 planes is likely important to the high T_C of optimally doped Tl2201 [20]. As well, neutron scattering experiments revealed a magnetic resonant mode in Tl2201. This magnetic resonant mode had been observed in Bi2212 and $YBa_2Cu_3O_{7-\delta}$ (YBCO) [24] but had not previously been observed in a single-layer compound; thus, the neutron scattering results clearly demonstrate that the mode is not a unique property of bilayer compounds. A pure *d*-wave order parameter was demonstrated for optimally and overdoped Tl2201 [25]. Heat transport measurements on overdoped Tl2201 ($T_C = 15\,\mathrm{K}$) suggest that the electrons at this doping level form a Fermi liquid. Moreover, these measurements put an upper bound on any subdominant order parameter of 0.5% [22], providing further evidence for a pure *d*-wave order parameter. Angle-dependent magnetoresistance oscillation (AMRO) measurements indicate a coherent FS, which is the first conclusive evidence for a well-defined FS for any cuprate at any doping level [11].

The first successful ARPES experiments on Tl2201 [26] arrived at an agreement with bulk probes on key features such as the normal-state Fermi surface [11] and the superconducting gap [19]. This success suggests that detailed ARPES studies of Tl2201 have the potential to reveal the nature and strength of many-body correlations when approaching high-T_C superconductivity from the more conventional overdoped regime.

This work presents the results from ARPES studies of Tl2201 performed by the Quantum Materials group at the University of British Columbia (UBC). The results show that while the FS is consistent with calculations and previous measurements, and the superconducting gap is consistent with a *d*-wave order parameter, unexpected results are observed for the lifetimes of the quasiparticle (QP) excitations. Previous ARPES measurements on the cuprates have focused on the underdoped and optimally doped regimes and have observed sharp, well-defined QP peaks at ($\pi/2$,$\pi/2$), broad peaks at (π,0), and a broadening with increasing binding energy over the entire electronic structure [6, 27, 28]. In contrast, we observe sharp peaks near (π,0) and broad features at ($\pi/2$,$\pi/2$). Further, while the QP linewidth increases with binding energy at ($\pi/2$,$\pi/2$) as expected, the opposite is seen at (π,0). In this work we also present a temperature-dependent determination of the superconducting gap.

The samples studied were grown using a copper-rich self-flux method and

were annealed in controlled oxygen partial pressures to produce overdoped samples with T_Cs ranging from 5 to 90 K. The high quality of the samples is demonstrated by the relatively narrow superconducting transition widths of 0.7 and 7 K for samples with T_Cs of 67.7 and 24 K, respectively (see Figure 2.1). The full-width half-maximum (FWHM) of the (0 0 10) x-ray rocking curve is 0.034°, indicating a good crystal structure (see Figure 2.2) [29]. The size of the crystals varied from sample to sample, but a 1 mm^2 plate 100 μm thick was typical.

The difficulties encountered during measurement stemmed from the inherent properties of the crystals, as opposed to crystal quality problems. The Tl2201 crystals are relatively hard compared to other cuprates. They are not as physically anisotropic either, and are prone to make glassy cleaves which are not flat or parallel to any crystal axis. Microscopy on the sample which produced the Fermi surface showed an array of fragments protruding from the cleaved surface. The presence of these fragments explained why when an angle was changed the signal would often disappear, and why minute 50 μm changes in sample position would restore the signal. The photon beam was likely blocked from reaching the sample surface by the protruding fragments.

The majority of the research presented was done at the Swiss Light Source, on the Surface and Interface Spectroscopy beamline, with circularly polarized 59 eV photons. The hemispherical electron analyzer used was the Scienta SES-2002 photoelectron spectrometer. The data were measured with an energy resolution of 24 meV and an angular resolution of 0.2°.

Measurements were taken at the SLS on two overdoped samples with T_Cs of 63 and 30 K, henceforth referred to as Tl2201-OD63 and Tl2201-OD30, respectively. The vast majority of the data taken were on Tl2201-OD30 and give sufficient information for a FS map and a study of QP lineshape anisotropy. The Tl2201-OD63 data did not allow a FS mapping but did provide QP lineshapes in the nodal and antinodal directions. The stoichiometry of the crystals is $Tl_{(1.88)2}Ba_2Cu_{(1.11)1}O_{6+\delta}$ with the departure from ideal stoichiometry corresponding to Cu substitution on the Tl site [23]. The samples were cleaved in situ at 10 K and were kept at 10 K and in a pressure of 6×10^{-11} mbar for the duration of the experiment.

In addition, temperature-dependent studies of overdoped Tl2201 samples with $T_C = 74$ K, henceforth referred to as Tl2201-OD74, were performed at the Stanford Synchrotron Radiation Lightsource (SSRL) on Beamline 5-4, using a Scienta SES-2002 photoelectron spectrometer. All data were acquired at 28 eV with linearly polarized light and with energy and angular resolutions of 15 meV

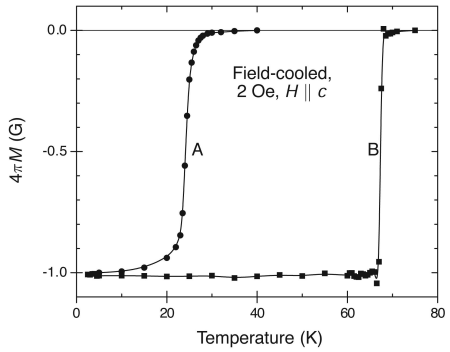

Figure 2.1: Field-cooled magnetization curves for crystals annealed in an O_2 partial pressure of 10^{-6} mbar at 290°C for 14 days (circles) and 10^{-7} mbar at 430°C for 6 days (squares), with T_Cs of 24 and 67.7 K, respectively. (Reproduced from Peets et al. [29])

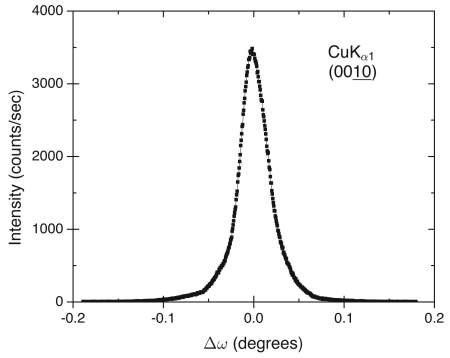

Figure 2.2: (0 0 10) X-ray rocking curve for a typical crystal ($T_C = 67.7$ K): the FWHM is 0.034°. (Reproduced from Peets et al. [29])

and 0.35°. The samples were cleaved at 3×10^{-11} torr and temperature cycled between 10 and 85 K. Spectra from different momenta were normalized by the k-independent spectral weight measured at binding energies between 6 and 11 eV.

2.1 Band structure calculations

Since it is generally believed that the normal metal on the very overdoped side of the HTSC phase diagram can be described as a rather conventional Fermi liquid system, in contrast to the strongly correlated Mott insulator found at half filling ($p = 0$ in Figure 1.1), exploring the electronic structure and FS of heavily overdoped Tl2201 can start with the results of non-interacting band structure calculations performed within the local density approximation (LDA). The most important structural element is the CuO_2 planes, which in Tl2201 are well separated from each other by the TlO and BaO layers [30]. As in all HTSC cuprates, the CuO_2-derived bands are expected to be the lowest-energy electronic states and thus directly determine the macroscopic electronic properties, such as, in particular, superconductivity.

The results of band structure calculations along the high-symmetry directions in the body-centred tetragonal Brillouin zone of Tl2201 are presented in Figure 2.3(a). The electronic structure of undoped (i.e. $\delta=0$) $Tl_2Ba_2CuO_6$ was calculated using the Stuttgart TBLMTO-47 computer code [31]. We used a basis set composed of $4s$, $4p$, and $3d$ orbitals for Cu, of $6s$, $6p$, $5d$, and $4f$ orbitals for Ba, of $6s$, $6p$, $5d$, and $5f$ orbitals for Tl, and of $3s$ and $2p$ orbitals for oxygen ($1s$ and $2p$ were used for empty spheres). Coordinates for the atoms are taken from Singh and Pickett [32]. The essential low-energy feature of the band structure is indeed the highly dispersive Cu($3d_{x^2-y^2}$)-O(1)($2p_{x,y}$) band (bold black line in Figure 2.3(a)); note, however, that this band is highly two-dimensional, with little dispersion along the k_z direction $(0,0,k_z=0)\rightarrow(0,0,k_z=\pi)$. Its top and bottom are located at (π,π) and $(0,0)$, respectively, within the two-dimensional projected Brillouin zone; at $(\pi,0)$ we find the so-called extended van Hove singularity, a saddle point in the electronic dispersion that experimentally exhibits a flat dispersion over a much larger momentum region than in the calculations [6]. The other two bands that sit at a comparable energy, i.e. 0 to –2 eV in Figure 2.3(a), are the anti-bonding Tl(6s)-O(2),O(3)(p_z) bands, which do show significant dispersion in the k_z direction. Based on the formal valences of stoichiometric and undoped $Tl_2Ba_2CuO_{6+\delta}$ (2:2:1:6 with Tl^{3+}, Ba^{2+}, Cu^{2+},

O^{2-}; $\delta = 0$), the Fermi energy would be located at the red line in Figure 2.3(a), and both the CuO_2 and TlO bands would cross E_F. This would result in a FS with hole pockets associated with the CuO_2 band and a small, spheroidal TlO electron pocket at the $\Gamma = (0, 0, 0)$ point, as in Figure 2.3(b). The presence of this small electron pocket, and the corresponding transfer of electrons from the CuO_2 to the TlO band, were originally proposed as a possible explanation for why undoped $Tl_2Ba_2CuO_6$ does not show the Mott insulating behaviour typically seen in undoped cuprates, such as La_2CuO_4, which results from the presence of a truly half-filled $3d_{x^2-y^2}$ CuO_2 band [32]. One should also realize that the non-stoichiometry of our samples ($Tl_{1.884(6)}Ba_2Cu_{1.11(1)}O_{6+\delta}$ [30]) provides additional hole doping even in the nominally undoped $\delta = 0$ case ($\sim$0.113 holes/formula unit, from the average between Tl and Cu non-stoichiometry). The latter would push the CuO_2 band further away from half-filling and eventually drive the TlO band above E_F. This shift of the chemical potential would generate a FS consisting solely of a CuO_2 hole pocket around (π, π), similar to the results shown in blue in Figure 2.3(a,c), which were calculated to match the 63% volume observed by ARPES on our $T_c = 30$ K overdoped Tl2201 crystal [26]. If the effect of hole doping through interstitial oxygen were explicitly included in the calculations, the TlO bands would likely be pushed to much higher energies, beyond the rigid band picture [33]. The analogous effects of Pb substitution or excess oxygen in the BiO layers of Bi-cuprates have recently been used to account for the lack of BiO electron pockets around (π,0) in those materials [34].

2.2 Electronic dispersion and Fermi surface by ARPES

The manipulator at the SIS beamline allows for two angular degrees of freedom. The entire cryostat can be rotated about its axis, which is oriented vertically, and the sample holder can be rotated about an axis normal to the face where the sample is mounted. The SIS geometry thus allows data to be taken along momentum directions radially outwards from the normal to the sample holder. For a sample mounted parallel to the sample holder, this would mean data would be taken along cuts radially outwards from Γ. Tl2201-OD30 was mounted off-normal, such that data were taken radially from a point near, although not exactly, (π,π) (see Figure 2.4), which allowed many of the sets of spectra taken

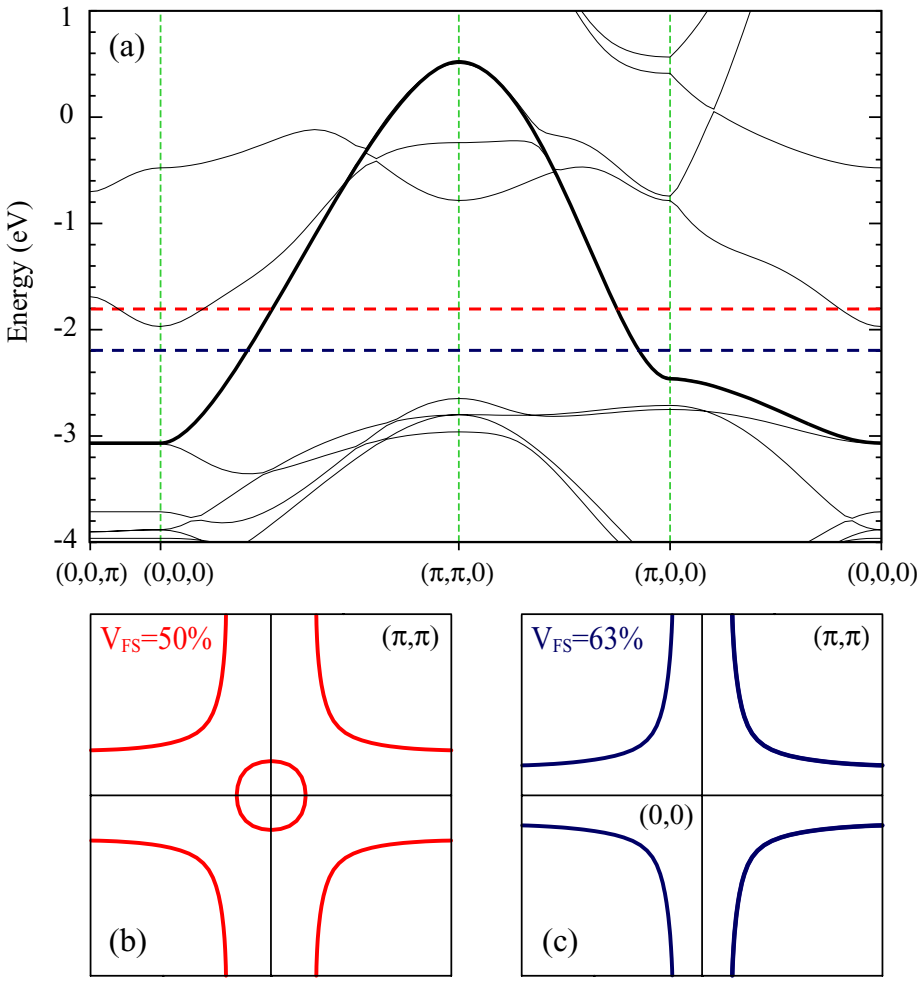

Figure 2.3: (a) Electronic dispersion obtained from band structure calculations within the local-density approximation (LDA). (b,c) FS calculated for two different doping levels enclosing a volume, counting holes, of 50% (red) and 63% (blue) of the two-dimensional projected Brillouin zone; the corresponding position of the chemical potential with respect to the dispersive electronic bands is indicated by the dotted lines in panel (a). Here, as in the rest of the thesis, k-space labels are expressed modulo the lattice constants.

to cross the FS at approximately normal.

Figure 2.5(b) shows ARPES data from a $T_C = 30\,\mathrm{K}$ very overdoped Tl2201 sample (Tl2201-OD30) taken close to the (0,0)–(π,π) direction in momentum space, the so-called nodal direction where the d-wave superconducting gap is zero.

Each line in Figure 2.5(b) is an energy distribution curve (EDC) from a given position in momentum space along the line marked as I in the FS plot of Figure 2.5(a). These EDCs show a strongly dispersing QP peak, related to the $3d_{x^2-y^2}$ CuO_2 band, which emerges from the background at high binding energies and progressively sharpens as it disperses all the way to the Fermi energy E_F. Note that, in the following, the term *quasiparticle* (QP) is used in a loose sense to identify a "reasonably sharp" dispersive peak, without precise reference to specific models accounting for correlation effects in a many-body system (more discussion will be given in Sections 2.3 and 2.4). From the results of band structure calculations (see Figure 2.3), we expect the bottom of this band to be located at the Γ point, or (0,0), at a binding energy of approximately 1 eV with respect to the chemical potential.

Although it is hard to track the band all the way down to high binding energies in the raw data, it is possible to highlight the band dispersion by taking a second derivative of the ARPES intensity with respect to energy. This is plotted in Figure 2.5(d) and indicates a filled bandwidth of only $\sim 250\,\mathrm{meV}$, suggesting a renormalization factor of about 4 between single-particle band structure calculations and measured ARPES spectra.

Near (π,0), the so-called antinodal direction where the d-wave superconducting gap exhibits its largest value, we also detected well-defined dispersive QP peaks, which define a shallow parabolic band. As mentioned in the discussion of the LDA calculations of Figure 2.3(a), the bottom of this band corresponds to the extended van Hove singularity observed near (π,0) in all HTSC cuprates [6, 35]. At this high doping level, this feature is located approximately 40 meV below the chemical potential, which corresponds to a renormalization factor of about 5 with respect to the band structure calculations.

The Fermi wavevector k_F can be determined using ARPES by by measuring the momentum at which a dispersing QP peak reaches E_F. This wavevector identifies one point along the normal-state FS, which is the contour in momentum space that separates filled from empty electronic states and whose existence and details are of fundamental importance for the understanding of the macroscopic physical properties of a material. By integrating the ARPES spectra over

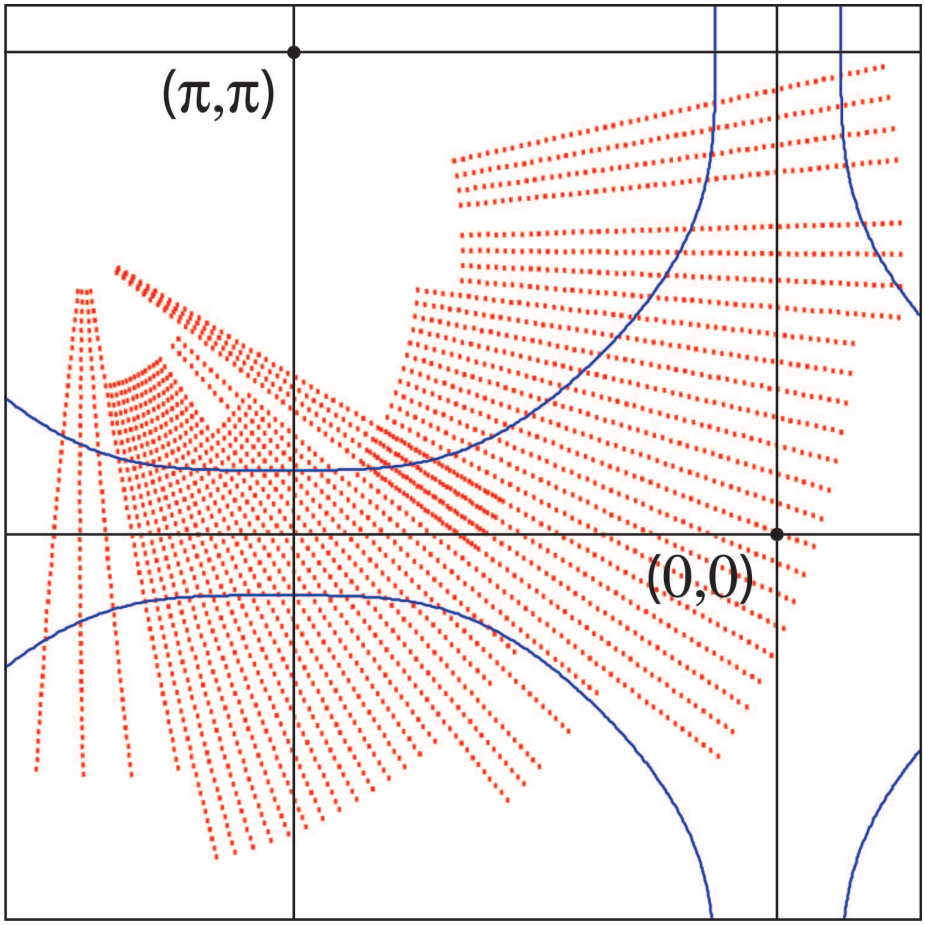

Figure 2.4: Direction of the cuts in momentum space on which ARPES data were obtained for Tl2201-OD30 (red). Momentum space is represented in the repeated zone scheme, with the tight-binding FS included for reference (blue). Data are seen to cover two irreducible symmetry units and multiple BZs.

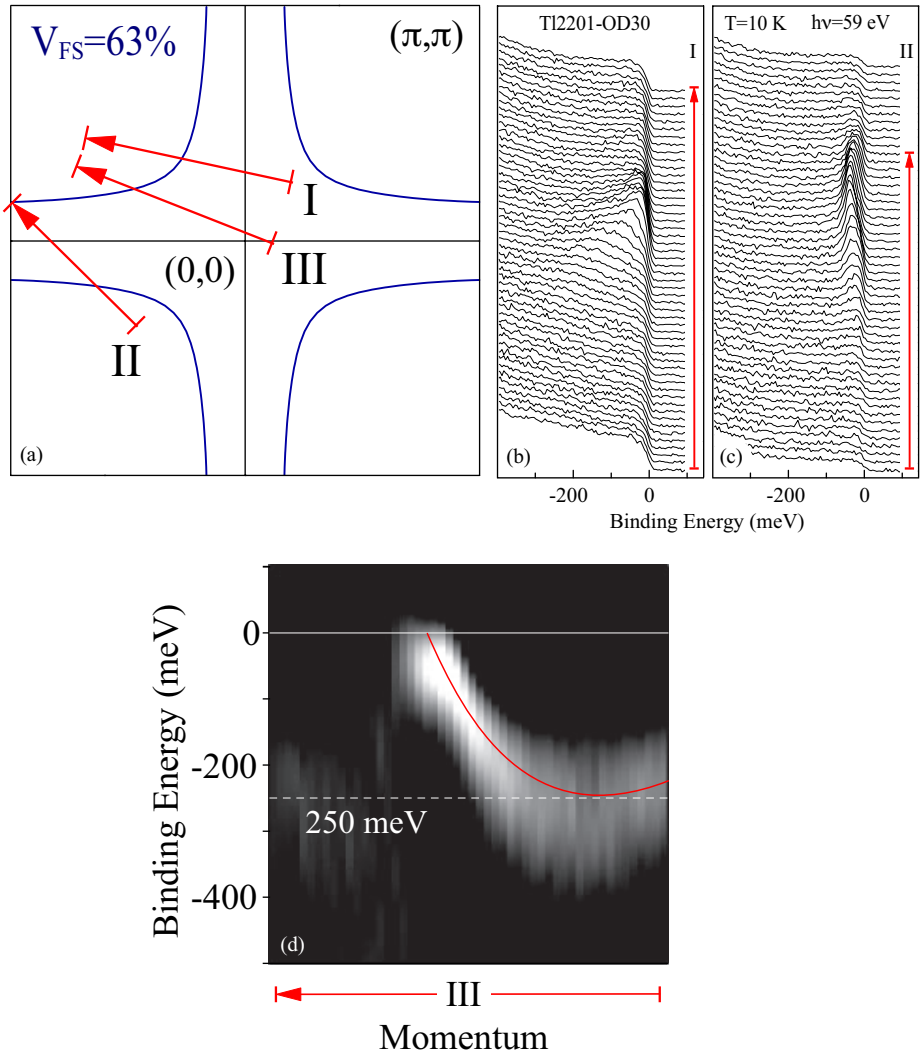

Figure 2.5: (a) FS calculated for a 63% Brillouin zone volume, counting holes, as in Figure 2.3(c). (b,c) ARPES spectra taken at $T = 10\,\mathrm{K}$ on Tl2201-OD30 along the directions marked by arrows I and II in (a). The portion of (c) that does not have a red arrow beside it extends into the second zone. (d) Second derivative vs. energy of the spectra from along arrow III in (a), also taken at $T = 10\,\mathrm{K}$; the red line is our tight-binding fit (see text).

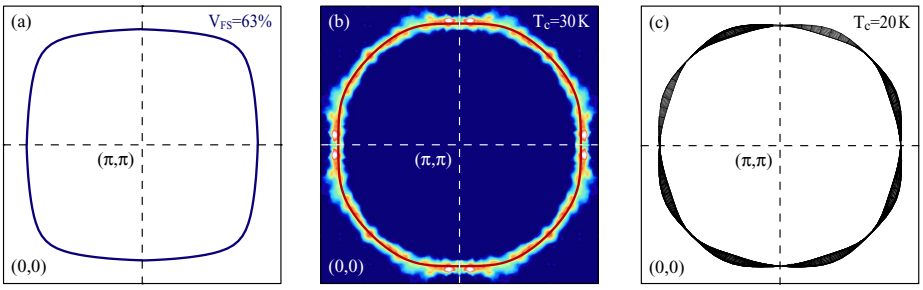

Figure 2.6: FSs, in the projected two-dimensional Brillouin zone, obtained from: (a) band structure calculations (imposing a volume of 63% counting holes, as observed by ARPES on Tl2201-OD30); (b) our ARPES experiments on the $T_c = 30$ K sample (Tl2201-OD30), measured at 10 K; and (c) the AMRO study on a $T_C = 20$ K Tl2201 crystal by Hussey et al. [11]. The red line in (b) is the result of our tight-binding fit of ARPES FS and dispersion; the width of the FS contour in (c) reflects the magnitude of the c-axis dispersion, here emphasized by a factor of 4 for clarity [11].

a ± 5 meV energy window about E_F for a large number of cuts in momentum space and then plotting the results versus momentum in the two-dimensional projected tetragonal Brillouin zone, one obtains an estimate of the normal-state FS. This has been done for Tl2201-OD30 and is shown in Figure 2.6(b). The location of the FS crossings has been determined over more than one quadrant across two different zones, and then backfolded to the first Brillouin zone and four-fold symmetrized to clearly show the detailed shape of the FS in the reduced zone scheme, with improved signal-to-noise. As expected, there is no indication of a TlO electron pocket around (0,0,0). In principle, given that the occupied TlO states should be confined to a small volume around the Γ point, the absence of the TlO pocket in the present ARPES data might simply be the result of having carried out the experiments at k_z values larger than the Fermi wavevector along the c-axis.

We checked this possibility by acquiring two-dimensional E_F intensity maps by ARPES as a function of photon energy, which allows one to study the evolution of the FS upon varying continuously the value of k_z; we have observed, however, no signature of the TlO spheroid over a wide range of photon energies. In conclusion, the FS determined from this procedure takes the form of a large hole pocket centred at (π,π) with an area that occupies $63\pm2\%$ of the Brillouin zone, corresponding to a carrier concentration of 1.26 ± 0.04 hole/Cu atom,

or p=0.26±0.04 greater hole density than the half-filled Mott insulator with 1 hole/Cu (p=0 in Figure 1.1). This result is in superb agreement with the recent study of the FS by angle-dependent magnetoresistance oscillation (AMRO) experiments [11], which found a hole-pocket volume of 62% of the Brillouin zone ($p = 0.24$) in a slightly more overdoped $T_c = 20\,\mathrm{K}$ sample (see Figure 2.6(a)). The ARPES determination is also in good agreement with the estimates from low-temperature measurements of the Hall coefficient, which gave a hole doping of p=0.30 holes/Cu for a $T_c \lesssim 15\,\mathrm{K}$ sample [36].

As a quantitative measure of the shape of the FS and of the many-body renormalized electronic dispersion, the Tl2201-OD30 ARPES data can be modelled by the tight-binding formula $\epsilon_{\mathbf{k}} = \mu + \frac{t_1}{2}(\cos k_x + \cos k_y) + t_2 \cos k_x \cos k_y + \frac{t_3}{2}(\cos 2k_x + \cos 2k_y) + \frac{t_4}{2}(\cos 2k_x \cos k_y + \cos k_x \cos 2k_y) + t_5 \cos 2k_x \cos 2k_y$ [24], setting a=1 for the lattice constant. With parameters μ=0.2438, t_1=−0.725, $t_2 = 0.302$, $t_3 = 0.0159$, $t_4 = -0.0805$, $t_5 = 0.0034$, all expressed in eV, this dispersion reproduces both the FS shape (the solid red line in Figure 2.6(b)), and the QP energy at (0,0) and (π,0) as seen in Figure 2.5(c,d). Note that experimentally the band bottom at (π,0) is extremely flat, a behaviour that could not be reproduced by including only t_1 and t_2 hopping parameters in the model. Alternatively, a simple analytical formula for the three-dimensional electronic dispersion of Tl2201 has been derived within the framework of the linear combination of atomic orbitals (LCAO) approximation [37] and was used to fit both ARPES [26] and AMRO [11] results. A basis set spanning the Cu $4s$, Cu $3d_{x^2-y^2}$, O $2p_x$ and O $2p_y$ states was used in order to take into account the effective Cu-Cu hopping amplitude between Cu $4s$ orbitals in neighbouring CuO_2 layers. This approach emphasizes the significance of the Cu $4s$ hopping amplitude in obtaining the correct three-dimensional FS shape, an issue that was originally raised by Andersen et al. [38]. With regards to the detailed shape of the FS, LDA band structure calculations predict a more square contour than observed by ARPES and AMRO (see Figure 2.6(a)). The inclusion of correlation effects, as well as Cu-Tl substitution or interstitial O-doping beyond a rigid-band picture, might lead to a better agreement; preliminary attempts have not yet led to appreciable improvements [33].

2.2.1 ARPES study of the superconducting gap

In order for Tl2201 to be a model system to study the overdoped HTSCs by surface and bulk sensitive probes, it is important to show that ARPES measures

quantities that are characteristic of the bulk, for both normal and superconducting states. In addition to the quantitative agreement on the normal-state FS, the observation of a superconducting gap in agreement with bulk measurements is also a necessary requirement. In the following, we will discuss three different methods for determining a gap by ARPES.

The first two show a gap consistent with a $d_{x^2-y^2}$ form. The third method allows one to follow the temperature dependence of the gap, highlighting the minimal surface degradation that occurs as the temperature is cycled from 10 to 85 K.

The detection of a $d_{x^2-y^2}$ gap using ARPES can be most easily visualized by the comparison of nodal and antinodal symmetrized spectra [39]. The spectra are symmetrized in energy about E_F, by taking $I(\omega)+I(-\omega)$, which minimizes the effects of the Fermi function.[1] While this procedure does not return a quantitative value for the size of the superconducting gap, it provides a qualitative criterion for determining whether or not there is a Fermi crossing and hence whether or not a superconducting gap has opened along the normal-state FS.

In the symmetrized ARPES data, the presence of a peak in the spectra at E_F indicates a FS crossing. This procedure has been used extensively for the Bi-based cuprates, both single and bilayer compounds, in detailed investigations of the normal-state FS, as shown for instance in Figure 2.7(c–f) [40], and of the superconducting as well as normal-state pseudogap [39, 41]. In the case of our Tl2201-OD30 sample, this crossing is clearly seen in the nodal direction (bold line in Figure 2.7(a)) but not in the antinodal direction (see Figure 2.7(b)), which is consistent with a d-wave functional form for the gap.

A more quantitative analysis of the gap can be performed by fitting ARPES spectra along cuts that cross the underlying normal-state FS, as shown in Figure 2.8. The model used to reproduce the spectra is a Lorentzian peak plus a step-like background. The latter is determined from the ARPES spectra with $k \gg k_F$ and is used to help phenomenologically isolate the coherent part of the spectral function. This lineshape is then multiplied by the Fermi distribution and convolved with the instrumental energy resolution function to obtain the

[1] This procedure assumes that the ARPES spectra are described by $I(\omega) = I_0 f(\omega) A(\mathbf{k}, \omega)$ and that there is particle-hole symmetry for a small range of ω and k about E_F and k_F, such that $A(-\epsilon_{\mathbf{k}}, -\omega) = A(\epsilon_{\mathbf{k}}, \omega)$. With the identity $f(-\omega) = 1 - f(\omega)$, it then follows that $I(\omega)+I(-\omega) = A(\mathbf{k}, \omega)$. As the assumptions in the symmetrization are the same assumptions that need to be made in order to do a fit of the gap, the results of the symmetrization do not provide a better starting point to fit the gap than the raw spectra. This procedure is also valid in the case that energy and momentum resolutions are included in the description of $I(\omega)$, via convolution with the resolution function $R(\Delta k, \Delta\omega)$ [39, 40].

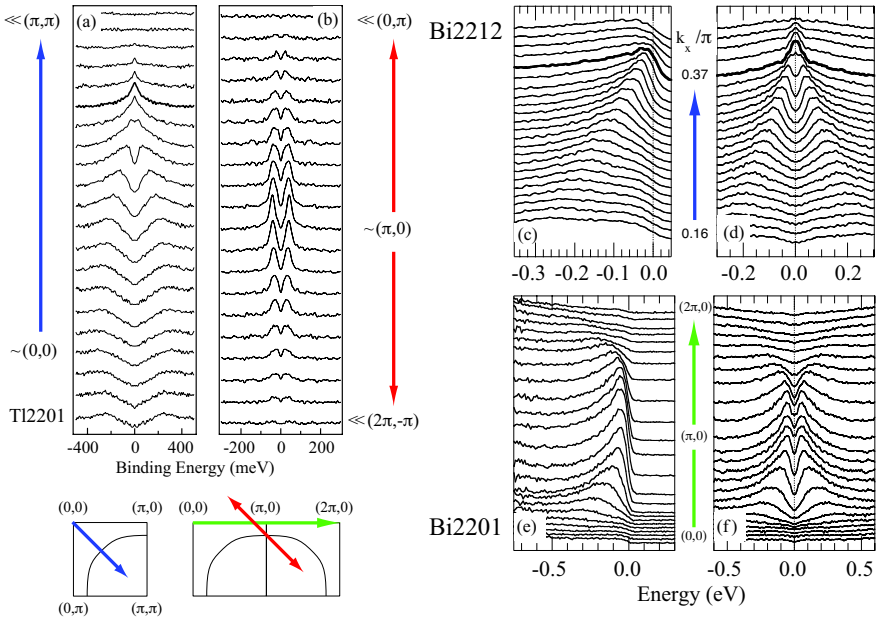

Figure 2.7: (a,b) Symmetrization of Tl2201-OD30 ARPES spectra, taken at $T = 10\,\mathrm{K}$, from along cuts I and II in Figure 2.5(b,c). ARPES spectra and their symmetrization along (c,d) the nodal direction for overdoped $Bi_2Sr_2CaCu_2O_{8+\delta}$ ($T_c = 88\,\mathrm{K}$, $T = 180\,\mathrm{K}$) and (e,f) perpendicular to the antinodal direction for overdoped $Bi_2Sr_2CuO_{6+\delta}$ ($T_c = 23\,\mathrm{K}$, $T = 25\,\mathrm{K}$); after Mesot et al. [40]. For all samples, the approximate locations of the k-space cuts are indicated in the Brillouin zone sketches. Bold lines in (a,c,d) mark the spectra that cross the Fermi energy, identifying a Fermi wavevector k_F; no crossing is observed for the spectra in (b,e,f).

functional form to be fit to the data [6]. This procedure for determining the gap has been used previously for $Bi_2Sr_2CaCu_2O_{8+\delta}$ [42]. The inset of Figure 2.8(b) shows good agreement between the raw data and the fit. Since heavily overdoped cuprates have weaker, possibly Fermi liquid–like electron correlations, good agreement between the measured QP peak and the Lorentzian is in principle expected.

Figure 2.8(d,e) shows the peak positions from the fits compared with our tight-binding description of the normal-state electronic structure near the antinodal region. At higher binding energies, there is good agreement between the fit peak positions and the normal-state dispersion.

At lower binding energies, however, the peak does not reach E_F but instead reaches a minimum at $\Delta_P \simeq 17\,\mathrm{meV}$ and then disperses back to higher binding energy. This behaviour is a hallmark of Bogoliubov QPs in a superconductor, as shown in the sketch of Figure 2.8(f,g), for which a beautiful experimental demonstration was obtained by ARPES on the trilayer Bi-cuprate $Bi_2Sr_2Ca_2Cu_3O_{10+\delta}$ [43]. Simultaneously, we observe a reduction of spectral weight, by about a factor of 2, when the QP peak has dispersed from the van Hove singularity all the way to k_F. This is consistent with the spectral intensity of Bogoliubov QPs being determined by the coherence factor $v_{\mathbf{k}}^2 = 1 - u_{\mathbf{k}}^2 = \frac{1}{2}(1 - \epsilon_{\mathbf{k}}/E_{\mathbf{k}})$, with $E_{\mathbf{k}} = \sqrt{\epsilon_k^2 + \Delta_{\mathbf{k}}^2}$, which corresponds to 1/2 when $\epsilon_{\mathbf{k}} = \epsilon_{\mathbf{k}_f} = 0$ and 1 for $|\epsilon_{\mathbf{k}}| \gg \Delta_{\mathbf{k}}$. Extending this analysis to other momenta along the FS, one can study the k-dependence of the gap: at $\sim(\pi/2, \pi/2)$ the peak does cross E_F (not shown), while at intermediate momenta a gap smaller than at $(\pi, 0)$ is observed, as on the right-hand side of Figure 2.8(d), consistent with d-wave symmetry.

The temperature dependence of the gap at the antinode has been measured for Tl2201-OD74. Figure 2.9(a,b) present symmetrized ARPES data along the $(\pi, 0) - (\pi, \pi)$ direction, at temperatures above and below T_C. In exactly the same manner as the k-dependent symmetrized data of Figure 2.7(a,b), the temperature-dependent data of Figure 2.9(a,b) show a clear gap at $k = k_F$ at 10 K, which is smaller at 85 K (with this type of analysis, the broadness of the QP peak and noise level make it hard to conclude whether the gap has completely closed at 85 K).

Figure 2.9(c) shows EDCs averaged over a narrow k-range around k_F at 10, 45, 85, and again at 10 K. The opening of the superconducting gap is indicated by the shift of the EDC leading-edge midpoint (LEM) to binding energies higher than the chemical potential for $T < T_C$, which defines the so-called LEM gap. The inset of Figure 2.9(c) shows a closer view of these k-integrated EDCs

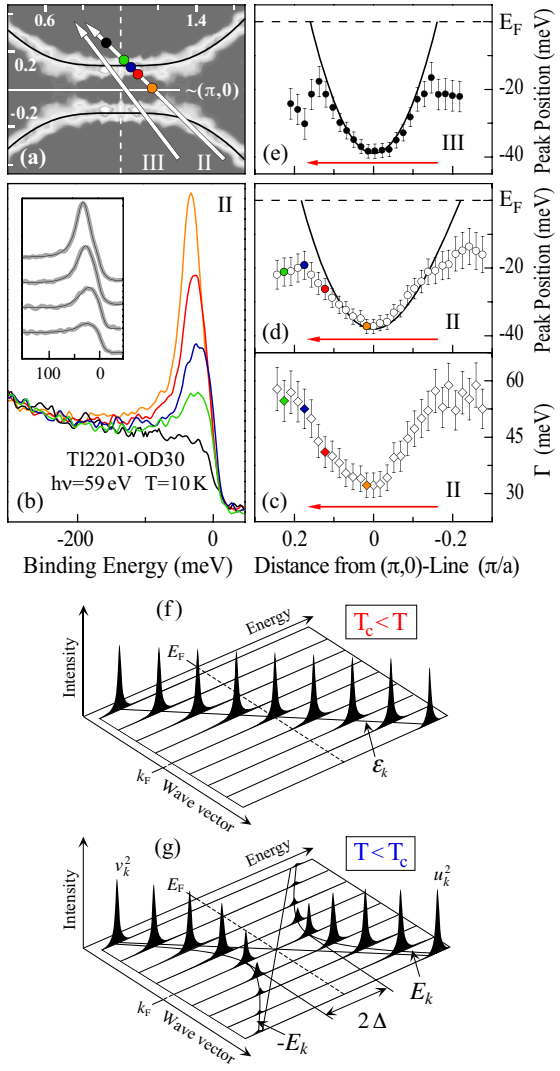

Figure 2.8: (a) Enlarged view of the FS of Tl2201-OD30 near (π,0). (b) Selected spectra from along cut II in (a); their k-space positions are indicated by circles of corresponding colour. (c,d) QP linewidth Γ and peak position from a Lorentzian fit of the energy distribution curves along cut II in (a). (e) Similarly, QP peak position along cut III in (a). Black lines in (a,d,e) are our tight-binding results (see text). (f) Normal- and (g) superconducting-state single-particle spectral function, highlighting particle-hole mixing and backward dispersion of Bogoliubov QPs below T_C (after Matsui et al. [43]).

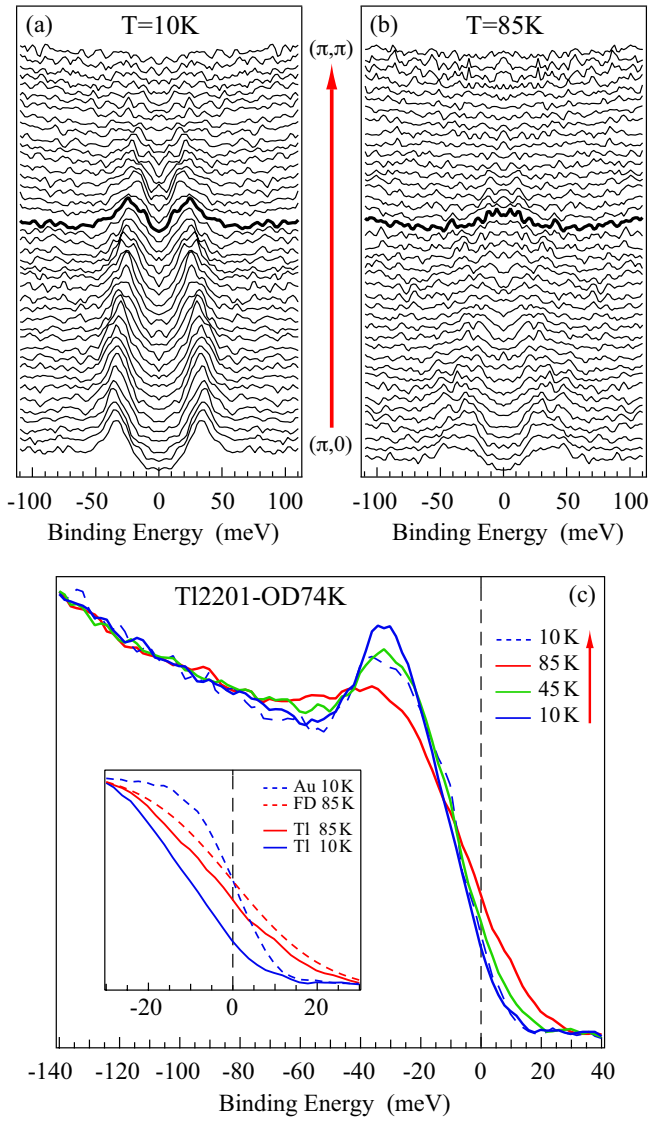

Figure 2.9: Symmetrized ARPES spectra measured at (a) 10 K and (b) 85 K on overdoped Tl2201-OD74, along the $(\pi, 0)-(\pi, \pi)$ direction. Bold lines indicate the EDCs closest to k_F. (c) The k-integrated spectral weight at the antinode, for several temperatures. The dashed 10K line is the same sample, returned to 10K after reaching 85K. An enlarged view of the leading-edge positions is given in the inset, together with a 10 K Au Fermi edge and an 85 K resolution-broadened Fermi function.

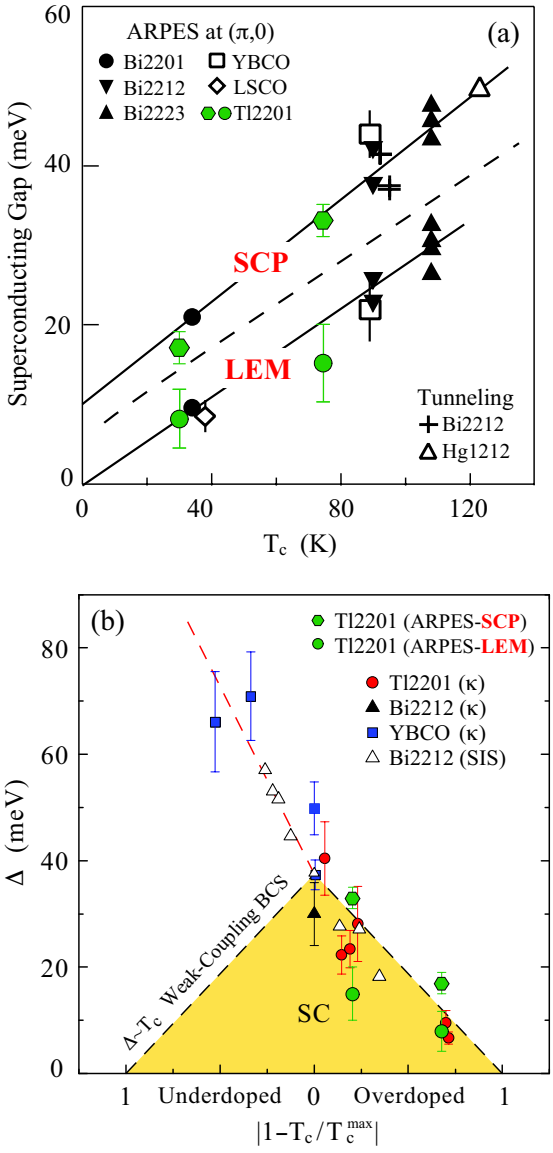

Figure 2.10: (a) Superconducting gap magnitude estimated by tunnelling and ARPES from the superconducting peak position (SCP) and the leading-edge midpoint (LEM) shift, plotted versus T_C for various optimally or overdoped cuprates (after Feng et al. [44]). (b) Gap values from thermal conductivity, tunnelling, and ARPES plotted vs. $|1-T_C/T_C^{\max}|$ for many HTSCs across the phase diagram (after Hawthorn et al. [19]); dashed lines are guides to the eye. Both plots include our own Tl2201-OD74 and Tl2201-OD30 ARPES results.

around E_F, together with 10 K polycrystalline Au data and the simulation of an energy-resolution broadened Fermi function at 85 K, which provide a reference for a normal-metal angle-integrated spectrum. It is clear from this figure that, as temperature increases, the size of the gap decreases, although it does not seem to completely close at 85 K. This is suggested by comparing the position of the LEM of the 85 K ARPES data with the simulated Fermi function; they are close in energy but not quite coincident. It is possible that there is still a pseudogap at temperatures slightly above $T_c = 74$ K at this doping level. It is worth emphasizing that as the temperature is lowered back to 10 K, the gap reopens to approximately the same size. Although a partial degradation of the ARPES features can be seen, the QP peaks and the gap are still clearly observable. This is strong evidence that the surface is stable under these experimental conditions and is thus suitable for detailed surface-sensitive experiments. From these data, a superconducting peak (SCP) position of ~ 33 meV and an LEM gap of ~ 15 meV can be extracted (for the more overdoped Tl2201-OD30 sample, we obtained ~ 17 meV and 8 meV, respectively [26]).

As a direct comparison with other cuprates and different means of determining the gap, Figure 2.10(a,b) presents a compilation of the doping dependence of the gap magnitude. Figure 2.10(a) refers only to spectroscopic studies of optimally and overdoped HTSCs, for which the gap is proportional to T_C. Our results from Tl2201-OD74 and Tl2201-OD30 are fully consistent with the behaviour observed on the other cuprates, as far as both SCP and LEM positions are concerned. Even more significant is Figure 2.10(b), which demonstrates that ARPES measures gap values that follow the same trend as those derived from thermal conductivity, a bulk transport property. A more accurate comparison would require an analysis of the ARPES data beyond the mere determination of SCP and LEM positions—for instance, on the basis of a model spectral function; this is, however, complicated by the non-trivial doping dependence of the ARPES data and in the present case was done for Tl2201-OD30 but not Tl2201-OD74.

2.3 ARPES lineshape analysis

The electrical and thermal transport properties suggest that overdoped Tl2201 may be regarded as a Fermi liquid [11, 22, 36]. Since the ARPES data for both the normal and superconducting states indicate that single-particle surface-

sensitive probes do provide information representative of the bulk, overdoped Tl2201 might be an ideal material for a quantitative study of the strength and nature of the many-body effects, which are revealed by the energy and momentum evolution of a QP's intrinsic ARPES lineshape [9]. In general, however, the shape of an ARPES peak does not correspond directly to an excitation's intrinsic lineshape. This discrepancy is primarily due to an extrinsic contribution from momentum and energy resolution of the analyzer. Recent work on the model two-dimensional Fermi liquid system Sr_2RuO_4 highlights the significant issues involved in removing the effects of the analyzer resolution [45]; in particular, it clearly shows that both the lineshape width and the peak position can be affected by resolution effects. There are significant challenges to completely removing the analyzer resolution from the data and stringent requirements on the data quality needed to attempt such analysis; therefore, we will analyze the current Tl2201 spectra in a more qualitative and phenomenological manner, concentrating primarily on the momentum dependence of the QP peaks measured in the superconducting state for different doping levels.

Beyond the issue of the experimental resolution, matrix element effects and the handling of the ARPES background are the two main complications in attempting even a qualitative description of the momentum dependence of the QP lineshapes. Experimentally, problems due to matrix element effects may be reduced by appropriate choice of measurement conditions such as geometry, photon energy, and polarization. For the experiments performed at the SLS and the data discussed in the following, circularly polarized 59 eV photons were used. Circular polarization was chosen specifically to minimize matrix element effects, which, using symmetry arguments, can be shown to be most extreme for linear polarization [6]. The photon energy was selected based on our experience on other cuprates—specifically $La_{2-x}Sr_xCuO_4$ (LSCO), where similar photon energies were used to reveal structure that had previously been missed in lower-energy ARPES data [46, 47]. Finally, in order to gain more reliable information, the ARPES data were taken over multiple Brillouin zones, making it possible to verify that, for the same point in the reduced-zone scheme, the lineshapes from different zones in the extended-zone scheme were qualitatively the same.

A commonly used method to isolate a QP peak from the experimental background [6, 48], is to subtract a phenomenological ARPES background determined from the data at k-values far removed from those at which the QP-like peaks are detected. In our analysis we will use this approach, taking as background the weakly k-dependent photoemission intensity observed in each mo-

mentum space cut for $k \gg k_F$. The fundamental problem with this approach is that if some of the background is related to the incoherent part of the spectral function, as one would expect for correlated-electron systems, then by subtracting the background we are actually disregarding some of the most crucial information contained in the ARPES spectra. In fact, the k- and ω-dependence of the incoherent part of the spectral function is, in many respects, as important as the behaviour of the QP peak itself; unfortunately we do not yet have the means to reliably extract information from it.

In Figure 2.5(b), similar to all previous photoemission studies of the cuprates [6, 35], we see that in the nodal region the width of the QP peaks increases as a function of binding energy, as expected from simple phase-space arguments [4]. This is, however, in sharp contrast to what is observed in the antinodal region, where the sharpest peak is found at the bottom of the band: in Figure 2.8(c), the linewidth Γ of the QP peak is observed to grow from ∼30 to ∼55 meV as the QP peak disperses from ∼39 to ∼20 meV binding energy. An analogous effect has since been reported for very overdoped and nearly non-superconducting $Bi_{1.74}Pb_{0.38}Sr_{1.88}CuO_{6+\delta}$ [49]. Possible origins for this anomalous behaviour will be discussed later. Another striking feature of the lineshape evolution is that the QP peaks are much broader in the *nodal* region than in the *antinodal* region, as evidenced by the direct comparison of Figure 2.5(b) and 2.5(c). To elaborate on this, in Figure 2.11(a) we present a compilation of spectra from along the FS contour, with k slightly smaller than k_F and corresponding to a binding energy of ∼35 meV. The choice in favour of spectral peaks at a binding energy lower than E_F is dictated by the need to compare spectra not affected by either the opening of the d-wave gap or the anomalous low-binding-energy broadening seen at the antinode.

The sharp peak near $(\pi, 0)$ becomes progressively broader as $(\pi/2, \pi/2)$ is approached. In order to determine whether this apparent broadening represents an increase in the QP linewidth Γ or is merely a loss of spectral weight, the momentum-independent background from $k \gg k_F$ is subtracted from the ARPES spectra,, as shown in Figure 2.11(b); then the data are integrated over varying energy ranges and plotted in Figure 2.11(c), normalized at the FS angle $\alpha = 0°$. For narrow integration windows, there is a drop as a function of α: the QPs show a loss of low-energy weight (and possibly coherence) in the nodal region. However, once the integration window is expanded to about 550 meV, the spectral weight of the QP peaks becomes angle independent (EDCs from different momenta were normalized by the k-independent spectral weight measured

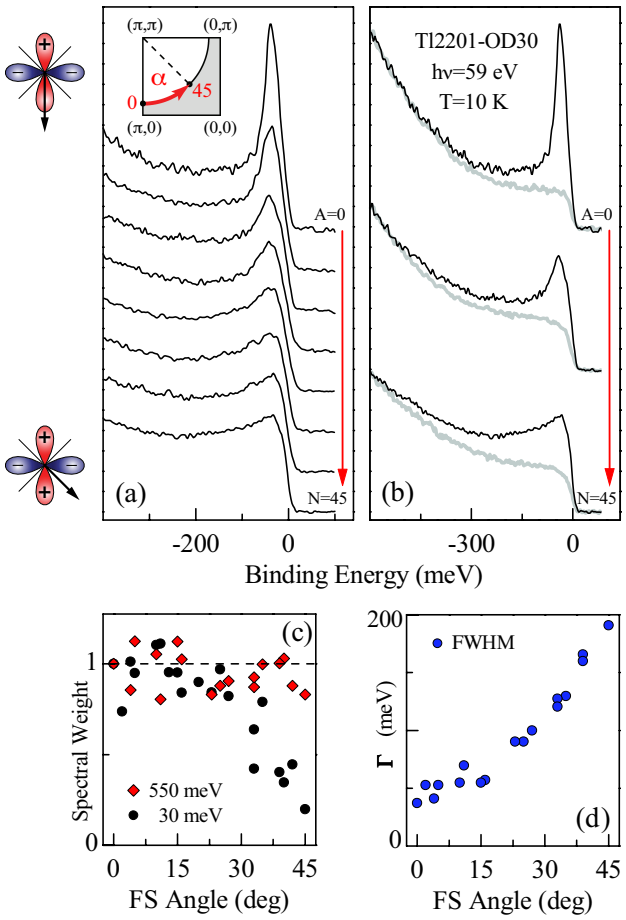

Figure 2.11: (a) Tl2201-OD30 ARPES spectra at k slightly smaller than k_F along the FS contour (corresponding to a QP binding energy of ∼35 meV). (b) Selected spectra from (a) along with their corresponding $k \gg k_F$ background. (c) Spectral weight of the background subtracted spectra, integrated over different energy ranges and normalized with respect to the $\alpha = 0$ antinodal value, plotted vs. the Fermi-surface angle α. (d) Quasiparticle linewidth Γ plotted vs. the Fermi-surface angle α. Nodal and antinodal momenta are here indicated, as in Figure 2.13, by the red-blue "butterfly" of the $d_{x^2-y^2}$ order parameter; note, however, that while ARPES can measure the k-dependence of the superconducting gap magnitude, it does not provide any information on the phase, whose determination requires phase-sensitive experiments [50].

at binding energies between 6 and 11 eV). This indicates that the k-dependent broadening of the ARPES spectra indeed reflects a loss of coherence of the QP spectrum, rather than being due to matrix element effects.

The observed QP anisotropy of Tl2201-OD30, with peaks much broader in the nodal than the antinodal region, is in sharp contrast to the behaviour observed in underdoped cuprates, where the QP peaks are sharp near $(\pi/2, \pi/2)$ and very broad around $(\pi, 0)$, as summarized in Figure 2.13. As doping is increased, the antinodal QP peaks sharpen but remain significantly broader than the nodal QPs up to optimal doping, at least in the normal state. Even in the superconducting state, where antinodal QPs sharpen considerably, the ARPES lineshapes for underdoped and optimally doped materials are still highly anisotropic, with a minimum in linewidth at $(\pi/2, \pi/2)$ [6, 35].

Overall this behaviour leads to the expectation that increasing doping beyond the optimal value will simply render the QP linewidths progressively more isotropic. Indeed, isotropic lineshapes were observed on early data from very overdoped, non-superconducting $Bi_{1.80}Pb_{0.38}Sr_{2.01}CuO_{6+\delta}$ [51], although more recent work on the same material [49] exhibits a behaviour more consistent with what is reported here for Tl2201. Going back to the QP anisotropy reversal observed for Tl2201-OD30 in Figure 2.11, and presented again in Figure 2.12(b) for nodal and antinodal points only, we note that the same, albeit less pronounced, effect was observed in our Tl2201-OD63 sample, as shown in Figure 2.12(a). For comparison, in the inset of Figure 2.12(a) we have plotted ARPES data from overdoped ($x = p = 0.22$) $La_{2-x}Sr_xCuO_4$ [28]. This sample has $T_C \simeq \frac{2}{3}T_C^{\max}$, comparable to the degree of overdoping of our sample Tl2201-OD63, which also has $T_C \simeq \frac{2}{3}T_C^{\max}$ for the much larger $T_C^{\max}$ of the Tl2201 family. The data from LSCO exhibit a QP anisotropy similar to that in Tl2201-OD63, suggesting that the observed QP anisotropy reversal might indeed be generic to the overdoped cuprates.

2.4 Discussion and conclusions

The results on the FS of Tl2201 mark an important new starting point for understanding the cuprates, namely that there is a material where both a surface-sensitive single-particle spectroscopic technique (ARPES) and comparable bulk transport measurements (AMRO) have arrived at quantitative agreement on a major feature of the normal state [11, 26].

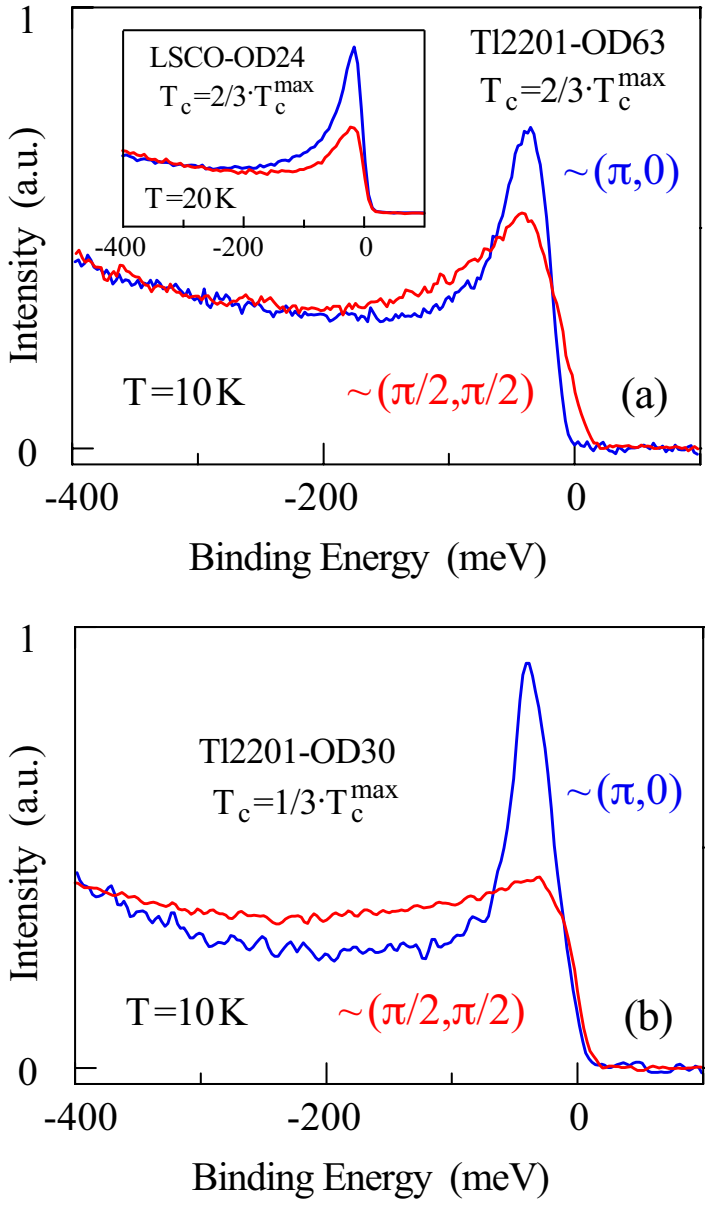

Figure 2.12: Nodal and antinodal spectra from (a) Tl2201-OD63 and (b) Tl2201-OD30, at $k \lesssim k_F$ and $T = 10\,\mathrm{K}$ Inset: similar data from overdoped LSCO-OD24 ($p = 0.22$, $T = 20\,\mathrm{K}$), from Zhou et al. (2004) [28]. For both samples in (a), $T_C \simeq \frac{2}{3} T_C^{\max}$ with respect to the $T_C^{\max}$ of each family [20].

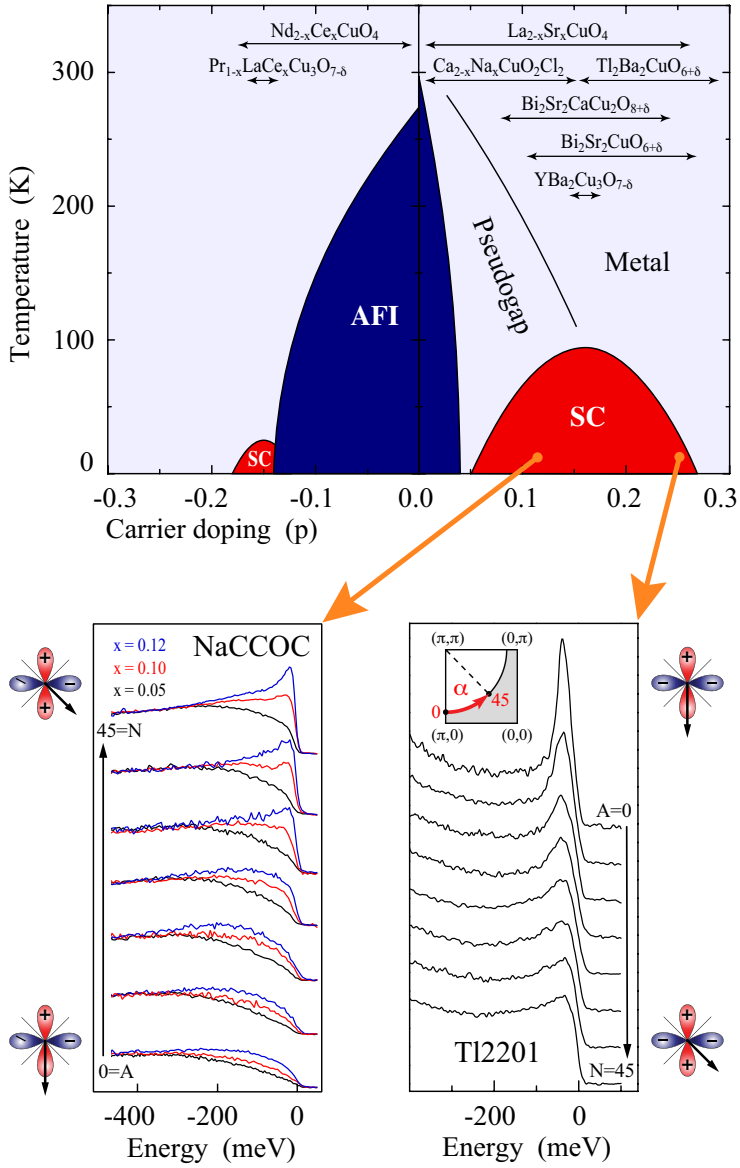

Figure 2.13: Nodal-antinodal QP anisotropy reversal observed in the cuprates. As a function of the FS angle α, sharp QP peaks are observed at the nodes (N) and ill-defined QPs at the antinodes (A) in underdoped cuprates (e.g. data from $Ca_{2-x}Na_xCuO_2Cl_2$, taken at $T = 15\,\mathrm{K}$, after Shen et al. (2005) [52]); in overdoped Tl2201, measured at $T = 10\,\mathrm{K}$, this behaviour is reversed.

This is a first for the copper-oxide high-T_C superconductors and, within the more general class of $3d$ and $4d$ transition-metal oxides, it is second only to the case of Sr_2RuO_4 for which a similar quantitative agreement was reached between de Haas–van Alphen [53, 54] and ARPES [45, 55, 56, 57, 58]. The detailed agreement on the FS (see Figure 2.6), together with the good quantitative agreement achieved for the superconducting gap by thermal conductivity and ARPES (see Figure 2.10), establishes Tl2201 as an ideal system to study the overdoped regime of the cuprate phase diagram with a wide spectrum of techniques. Next it will be important to study the single-particle excitation spectrum with both ARPES and scanning tunnelling spectroscopy (STS) in enough detail to compare to other normal-state properties, thus critically testing whether or not a conventional Fermi-liquid description of the electronic properties captures the physics of the normal metal in the heavily overdoped regime. In this regard, it is important to elaborate on the most surprising result that emerged from this study of overdoped Tl2201 by ARPES, one that is counterintuitive within the realm of Fermi-liquid theory: the QP anisotropy reversal observed across optimal doping (see Figures 2.11 and 2.12).

2.4.1 Quasiparticle anisotropy reversal

A summary of the momentum anisotropy as seen by ARPES in under- and overdoped cuprates is given in Figure 2.13, where data from $Ca_{2-x}Na_xCuO_2Cl_2$ for several doping levels [52] and Tl2201 are directly compared. Early magnetotransport experiments on very overdoped Tl2201, for which a small magnetoresistance and a weak T-dependence of the resistivity and cotangent of the Hall angle have been observed, do not support the presence of strongly k-dependent low-temperature scattering rates in the normal state [36]. More recently, a temperature- and doping-dependent AMRO study of Tl2201 suggested a two-component scattering rate consisting of an isotropic T^2 term as well as an anisotropic T-linear term [59], which vanishes at the nodes and has a maximum near the antinodes. The anisotropic term becomes weaker as the doping increases, which is consistent with the view that as hole doping increases, the antinodal QPs should gain coherence faster than the nodal ones, eventually leading to a relatively small and fully isotropic scattering rate. Therefore, what is at variance between the ARPES and AMRO results from Tl2201 is not the behaviour of the antinodal QPs, which in both cases are indeed gaining coherence upon overdoping, but rather a progressive loss of coherence of the nodal

QPs seen in ARPES as doping increases. In addition, on a more quantitative level, one should realize that the overall magnitude of the scattering rate seen by ARPES is approximately a factor of 10 larger than estimated by AMRO.

What could be the origin for this discrepancy between ARPES- and AMRO-determined scattering rates? In this regard, it is worth emphasizing that while AMRO experiments are possible on Tl2201 but not on LSCO, owing to the higher impurity content of the latter, the ARPES features from the two compounds in the overdoped regime are actually quite comparable (see Figure 2.12). This seems to point to the fundamental differences between what the two techniques actually probe. A key difference between the measurements is that while our ARPES experiments were performed in the superconducting state, the AMRO measurements were carried out in the normal state, and the latter is achieved by the application of external magnetic fields as high as 45T, which might potentially affect the low-energy QP dynamics. As for the reliability of the ARPES data on the specific point of the loss of coherence of nodal QPs at large dopings, it is important to mention that these findings are also supported by a preliminary study of overdoped $Bi_2Sr_2CaCu_2O_{8+\delta}$ by scanning tunnelling microscopy (STM) and STS [60]. From the Fourier analysis of the energy-dependent spatial modulations observed in the tunnelling conductance [61], it was concluded that for strongly overdoped samples, the nodal (i.e. low-energy) QP interference signal is no longer visible, consistent with a decoherence of the nodal states [60]. Interestingly, although a precise connection is not yet established, terahertz [62] and optical [63, 64] spectroscopy results also suggest an abrupt transition in the low-energy QP dynamics across optimal doping, as evidenced by (i) the decay time of the transient reflectivity in pump-probe experiments on Bi-cuprates [62]; (ii) the doping dependence of the low-frequency optical spectral-weight redistribution across T_C in Bi-cuprates [63]; (iii) the decrease of the optical scattering rate upon overdoping in Tl2201 [64].

A reconciliation of the results might require consideration of the specific sensitivity of transport probes and single-particle spectroscopies to electronic scattering phenomena. In particular, photoemission and scanning tunnelling spectroscopy are very sensitive to electronic scattering involving small momentum transfers, while transport is rather insensitive to it. A possible source of such scattering could be minor distortions of the CuO_2 planes caused by impurities far from the CuO_2 planes themselves [20, 65], such as cation substitution or interstitial oxygen, which increase with doping in most cuprates. Calculations show that the inclusion of elastic forward scattering in a *d*-wave superconductor

can lead not only to an overall increase of the scattering rate in the normal state but also to a strong enhancement of antinodal QP coherence in the superconducting state [66]. A very different model, based on the description of unitary-limit scattering beyond the Born approximation so as to account for multiple scattering from a single point-like impurity, would also lead to loss of nodal coherence and enhancement of antinodal coherence below T_C [67]. However, both models predict an approximately isotropic QP scattering above T_C, as well as temperature-dependent effects limited to the energy scale of the gap itself. To test the applicability of these scenarios to the present case, a thorough temperature-dependent study is required. Sources of scattering relevant to this discussion are not just limited to impurities; inelastic (i.e. electronic) scattering involving small momentum transfer might also result in anomalous decoherence of the nodal QPs. For instance, low-energy (i.e. small q) quantum-critical fluctuations associated with proximity to a competing superconducting $d_{x^2-y^2}+id_{xy}$ phase [68], or a ferromagnetic phase, could also lead to a similar QP anisotropy reversal [69]. Recent measurements of overdoped LSCO show a similar QP anisotropy reversal, and upon light doping with Fe, a magnetic transition is observed [70].

2.4.2 Investigating quantum criticality and phase changes

The QP anisotropy reversal observed could be coincident with the proposed quantum critical point in the cuprate phase diagram [71]. It has been suggested that quantum phase transition from a $d_{x^2-y^2}$ to a $d_{x^2-y^2}+id_{xy}$ order parameter, as a function of some tuning parameter, possibly doping, may give rise to increased scattering rates of the nodal QPs. At the phase transition, low-energy bosonic modes would couple to the gapless nodal QPs [68]. While this proposal provides a convenient mechanism for explaining the broad QP lineshape in the nodal direction, a complex d_{xy} pairing component (i.e. $\sin k_x \sin k_y$) would generate an order parameter with no nodes. This is inconsistent with the results from Tl2201-OD30, which show a clear FS crossing in the nodal region. Heat transport measurements on Tl2201 indicate that the superconducting order parameter has nodes and, further, is consistent with the simplest $d_{x^2-y^2}$ pairing scenario [22]. The Tl2201-OD30 data, coupled with the heat transport data, provide strong evidence that quantum criticality, if it exists, is either not associated with the development of an id_{xy} order parameter or that doping is not,

in fact, the actual tuning parameter.

2.4.3 ARPES-specific broadening mechanisms

Magnetotransport experiments—where a small magnetoresistance and a weak T-dependence of the resistivity and cotangent of the Hall angle have been observed—do not indicate the presence of strongly k-dependent scattering rates. While these experiments are performed in the normal state, in contrast to the ARPES results presented, the comparison of the results from the two techniques may indicate that ARPES-specific scattering mechanisms for the nodal QPs, such as elastic forward scattering and the effects of a non-zero k_z dispersion, have to be examined.

We comment here on two extrinsic effects that could potentially contribute to an anomalous k-dependent broadening of the QP lineshapes: residual k_z electronic dispersion and resolution broadening effects. First, the dispersion of the electronic structure along the c-axis may indeed give rise to $k_{||}$-dependent broadening of the ARPES features [72, 73] (where $k_{||}$ is the ab-plane momentum). This effect could be doping dependent, because there is a 0.4% c-axis lattice constant reduction as doping is increased [23]. However, the k_z-dispersion vanishes in Tl2201 along the $(0,0)-(\pi,\pi)$ and $(\pi,0)-(\pi,\pi)$ directions, and thus at all nodal and antinodal points. This is a direct consequence of the symmetry of the body-centred tetragonal unit cell, and it holds also for LSCO. Figure 2.14(a,b) illustrates this point by showing ARPES data for both materials together with band structure calculations for LSCO [72] and AMRO data for Tl2201 [11].

Along these high-symmetry directions, no k_z-dispersion is present in either the LSCO calculations or the Tl2201 AMRO data (in both cases the k_z-dispersion is proportional to the width of the three-to-two-dimension projection). This is consistent with the ARPES maps for the two systems, although the broader E_F intensity patches for LSCO indicate that the three-dimensionality is much stronger in LSCO than in Tl2201. A residual k_z dispersion might contribute to the overall width of the ARPES features [72, 73], but it cannot be responsible for the reversal of the anisotropy observed on overdoped cuprates, since the anisotropy exhibits a monotonic $k_{||}$-dependence between $(\pi/2,\pi/2)$ and $\sim(\pi,0)$.

The second extrinsic effect that influences the width in energy of an ARPES spectrum, or EDC, is instrumental resolution. In a two-dimensional system, the

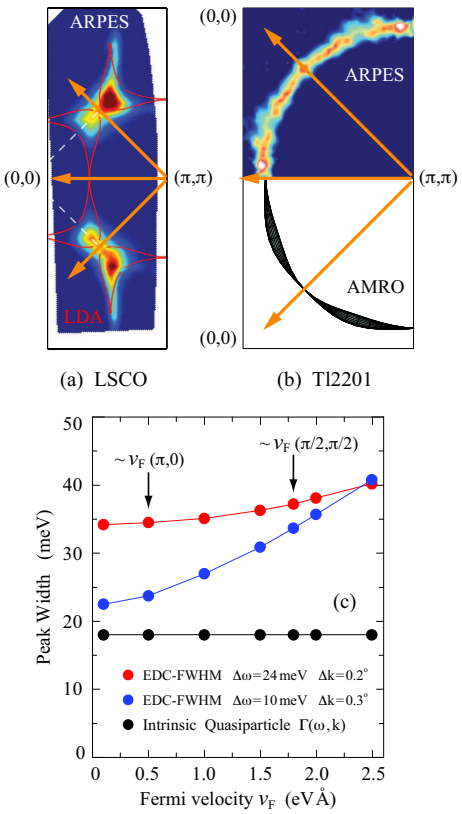

Figure 2.14: (a) ARPES intensity map for emission from E_F for overdoped LSCO-OD24 ($p = 0.22$). Red lines are the calculated three-dimensional FS for $k_z = 0$ and π/c; the enclosed area is the projection of the FS onto the two-dimensional k_x–k_y plane and denotes the region allowed for emission [72]. (b) ARPES and AMRO [11] data from Tl2201 (for $p = 0.26$ and 0.24, respectively). In (a,b) the yellow arrows identify directions characterized by zero k_z dispersion as indicated by the LDA calculations and consistent with AMRO experiments, which also suggest much weaker residual three-dimensionality effects in Tl2201 than in LSCO. (c) Resolution contributions to the width of an ARPES energy-dispersion curve calculated, as a function of Fermi velocity v_F, from the two-dimensional convolution of a Lorentzian QP peak (binding energy $\omega = 30$ meV and intrinsic width $\Gamma = 18$ meV) with Gaussian energy and momentum resolution functions (results corresponding to our experimental parameters are in red).

width in energy is determined by the intrinsic inverse lifetime of the QP excitation and by the experimental resolution broadening, which reflects both the energy ($\Delta\omega$) and angular (Δk) resolution of the apparatus [9]. For a dispersionless feature, the instrumental contribution to the total EDC width is determined solely by the energy resolution $\Delta\omega$. However, for a dispersive feature, the angular resolution Δk contributes to the energy broadening in a manner directly proportional to the band velocity ($v_F \neq 0$ in Figure 2.14(c)). Since the Fermi velocity around the FS of the cuprates is highly anisotropic, varying from approximately 0.5 to 1.8 eVÅ in going from the antinodal to nodal region, this should give rise to a momentum-dependent resolution broadening of the EDCs. This broadening would be more severe at the nodes, where v_F is at its largest, which raises the concern that the larger nodal widths shown in Figures 2.11 and 2.12 might be an artifact of the instrumental resolution. We have carefully evaluated the contribution of resolution-broadening effects for our experimental conditions with a variety of different procedures, and the results are summarized in Figure 2.14(c). For our experimental parameters (red data, $\Delta\omega = 24$ meV and $\Delta k = 0.3°$) the k-dependent resolution broadening is on the order of a few meV, nowhere near the factor of 4 observed in Figure 2.11(d).

2.4.4 Broadening of the antinodal quasiparticles towards lower binding energies

A candidate for explaining the anomalous behaviour of this system is microscopic inhomogeneity. STM measurements have shown that on Bi2212, there is a strong inhomogeneity in the local density of states (LDOS) [74]. Pan et al. [74] suggest that the inhomogeneity in the bulk may give rise to a microscopic modulation in the gap size and, further, that averaging over a macroscopic spot on the sample, as is effectively done by ARPES, will produce a broadening in the antinodal region and will have little effect in the nodal region. Pan et al. [74] use this observation to explain the lineshape anisotropy around the FS in underdoped and optimally doped cuprates. By analogous reasoning, microscopic inhomogeneity may be responsible for the observed broadening of the antinodal QPs towards lower binding energies. This mechanism may also be responsible for the analogous effect reported in $Bi_{1.74}Pb_{0.38}Sr_{1.88}CuO_{6+\delta}$ and may be generic to overdoped cuprates in general.

Chapter 3

ARPES on $YBa_2Cu_3O_{7-\delta}$

Not only did Tl2201 offer us the opportunity to perform ARPES studies on the overdoped side of the phase diagram, it also yielded the first results on HTSCs from a surface-sensitive technique that agreed with those acquired through bulk probes. On the underdoped side of the phase diagram, despite an impressive body of ARPES research, there is still no consensus as to the topology of the Fermi surface. The materials that have generated the bulk of underdoped ARPES results all have insufficient mean free paths to allow fermiology by bulk-sensitive probes.

$YBa_2Cu_3O_{7-\delta}$ (YBCO) allows us to study the underdoped side of the phase diagram and, owing to the fact that it is free of cation disorders and has excellent crystallinity, with a rocking curve FWHM of $<0.01^\circ$ achievable [12], provides us with a clean system with sufficient mean free path to allow quantum oscillation measurements to study the Fermi surface. However, reconciling surface-sensitive studies of YBCO with the results of bulk probes has been hampered [75, 76, 77] by the polarity and resulting self-doping of the YBCO surface. By in-situ deposition of potassium atoms on cleaved YBCO, we can not only restore the doping of the surface to that of the bulk, allowing us to perform ARPES studies on YBCO whose results are directly comparable with those of bulk-sensitive techniques, but we can also continuously control the surface doping and follow the evolution of the Fermi surface (FS) from the overdoped to the underdoped regime.

ARPES on the surfaces of easily cleaved materials such as $Bi_2Sr_2CaCu_2O_{8+\delta}$ shows that in zero magnetic field the Fermi surface breaks up into disconnected arcs upon underdoping. [39, 41, 52]. However, in high magnetic field, quantum oscillations at low temperatures in $YBa_2Cu_3O_{6.5}$ (YBCO6.5) [13] indicate the existence of small Fermi surface pockets [14, 15, 78, 79, 80, 81, 82, 83, 84, 85, 86]. Unfortunately Bi2212 and YBCO6.5 are not directly comparable, since they are different materials with different electronic structures. An ARPES study of YBCO6.5 would help elucidate the origin of the Fermi surface pockets.

3.1 Fermi surface topology of underdoped cuprates

In the heavily overdoped regime, angle-dependent magnetoresistance oscillation [11] and ARPES experiments [26, 30] on $Tl_2Ba_2CuO_{6+\delta}$ have arrived at a quantitative consensus in observing a large holelike Fermi surface (FS). Upon reducing the number of holes in the CuO_2 planes, the FS volume decreases in the manner expected by Luttinger's theorem, but below optimal doping the single-particle FS appears to reduce to four disconnected nodal Fermi arcs. This scenario was suggested from ARPES studies of Bi-cuprates [39, 41] and $Ca_{2-x}Na_xCuO_2Cl_2$ [52] and is thought to be connected to the existence of the pseudogap. The detection of quantum oscillations in oxygen-ordered ortho-II YBCO6.5 suggests a different scenario involving FS reconstruction into hole and/or electron pockets [13, 14, 15]. These two pictures are derived from quite different measurement techniques, performed on different materials, and under conditions of high magnetic field in one case but zero field in the other.

Owing to the complex multiband and correlated character of the electronic structure of YBCO6.5 [79], the determination of the nature of these pockets and their generality to the underdoped cuprates requires connecting transport and single-particle spectroscopy information on the same underdoped system. The study of YBCO6.5 by ARPES is thus crucial.

3.2 YBCO structure and polar surfaces

YBCO is complicated by the lack of a natural [001] cleavage plane and also by the presence of CuO-chain layers. The unit cell of YBCO consists of the following layers: a Y layer is at centre, and on either side of it is a CuO_2 plane, followed by a BaO layer, followed finally by a layer of $CuO_{1-\delta}$ chains (see Figure 3.1(a)). The calculated electronic structure of the CuO_2 bilayer splits into bonding and antibonding bands (see Figure 3.1(b)). The ortho-II state of YBCO—YBCO6.5—has chain layers in which the chains alternate between having full and vacant oxygen sites. As grown, samples are twinned, meaning there are domains of parallel chains, but that the chain orientation changes by 90° across domain boundaries. Since chains are one-dimensional structures, they produce a one-dimensional parabolic band. ARPES on a twinned sample results in one-dimensional features seen in both x and y directions. However, by

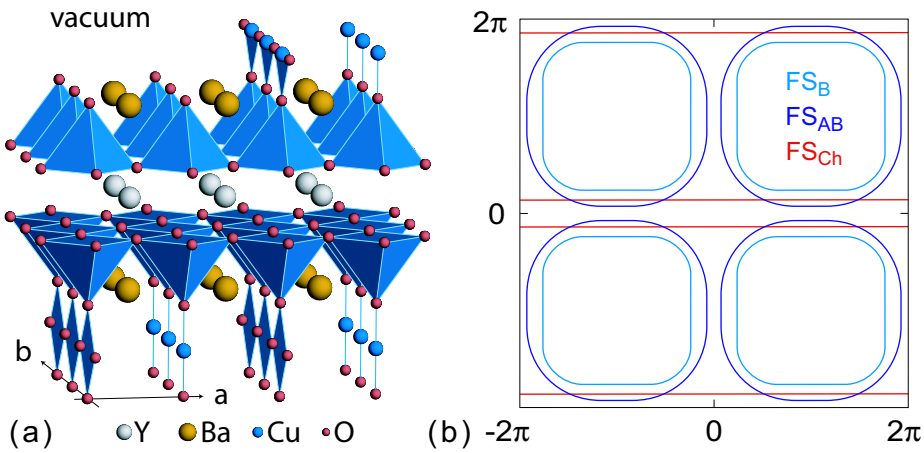

Figure 3.1: The surface of cleaved YBCO. (a) Structure of oxygen-ordered YBCO6.5 (with alternating oxygen-full and -empty chains), showing the BaO- and CuO-chain terminations of the cleaved surface. Electronic reconstruction takes place at these polar surfaces, similar to the prototypical case of a polar catastrophe in ionic insulators with a $|1+|1-|1+|1-|...$ layer-by-layer charge [87]. This leads to "overdopedlike" FS features for the topmost layers, as shown pictorially in (b) for CuO_2-plane bonding and antibonding bands (FS_B and FS_{AB}), and the one-dimensional CuO-chain band (FS_{Ch}).

annealing the YBCO6.5 crystal at a controlled temperature and oxygen pressure while stressing it in one dimension only, a detwinned sample—in which all chains are parallel from one layer to the next—may be produced [12].

More specifically, YBCO cleaves between the CuO chain layer and the BaO layer, leaving on the cleaved surface relatively large regions (>100 Å) of either CuO or BaO terminations, the latter positively charged and the former neutral. Electronic reconstruction takes place at these polar surfaces, similar to the prototypical case of a polar catastrophe in ionic insulators with a $|1+|1-|1+|1-|...$ layer-by-layer charge [87], leading to self-doping of the surface. Scanning-tunnelling microscopy shows that the CuO-chain terraces are characterized by prominent surface density waves [88] and differ substantially from the bulk: as also seen in ARPES [75], they exhibit surface states and unavoidable doping disorder. Recent ARPES studies of nearly optimally doped YBCO indicated that surfaces terminating in either a CuO or BaO layer give different contributions to the total photoemission intensity [77] and that the doping of the topmost CuO_2 planes visible by ARPES is $p = 0.3$, almost irre-

spective of the nominal bulk doping. This corresponds to heavy overdoping, all the way into the non-superconducting regime (see Figure 3.5), and is actually not achievable in bulk, fully oxygenated YBCO7.0 for which $p = 0.194$ [89]. Similar problems have been encountered in the ARPES study of $YBa_2Cu_4O_8$ [90].

3.3 ARPES on YBCO achieved through potassium deposition

3.3.1 Sample preparation

$YBa_2Cu_3O_{7-\delta}$ single crystals were grown in non-reactive $BaZrO_3$ crucibles using a self-flux technique. The CuO_x-chain oxygen content was set to $\delta = 0.49$ by annealing in a flowing O_2:N_2 mixture and homogenized by further annealing in a sealed quartz ampoule, together with ceramic at the same oxygen content. After mounting for the cleave required in an ARPES measurement, the samples were cooled from 100 °C to room temperature over several days to establish the ortho-II superstructure ordering of the CuO_x chain layer [12]. The particular sample used in the present study was twinned, as confirmed by x-ray diffraction after the ARPES measurements.

3.3.2 ARPES experiments

ARPES measurements were carried out on the Electronic Structure Factory endstation at Beamline 7.01 of the Advanced Light Source (ALS). The data were measured with linearly polarized 110 eV photons and a Scienta R4000 electron analyzer in angle-resolved mode. YBCO6.5 single crystals were cleaved in situ at a base pressure lower than 2.5×10^{-11} torr and then oriented by taking fast Fermi surface scans. A wide momentum-distribution map of the FS from "as-cleaved" YBCO6.5 is presented in Figure 3.2(a). The ARPES data are a superposition of features from the BaO- and CuO-terminated regions: because of the few-Å electron escape depth at these photon energies, the ARPES intensity from the BaO-terminated regions (The oxygen of the BaO unit is the apical oxygen of the CuO_2 plaquettes) is dominated by the CuO_2-bilayer bands and that from the CuO-terminated regions by the chain band. The comparison with Figure 3.1(b) allows one to identify the FS features originating from the CuO_2-plane bonding and antibonding bands (FS_B and FS_{AB}), and the one-dimensional (1D) CuO-chain band (FS_{Ch}). Note that the strong momentum-dependent intensity

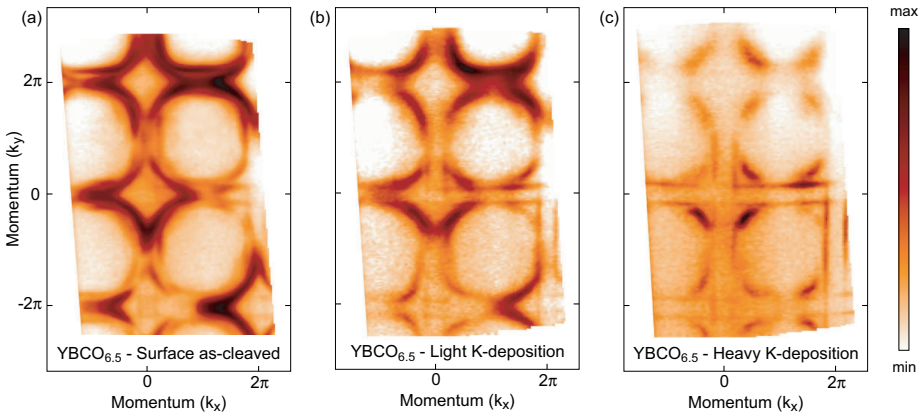

Figure 3.2: YBCO FS evolution upon e^- doping. Energy and angular resolutions were set to ~ 30 meV and 0.2° (±15° angular window), and the sample was at $T = 20$ K. The FS maps were obtained by integrating the ARPES intensity over a 30 meV energy window about E_F and then normalizing the intensity maps relative to one another for display purposes. (a) ARPES FS of as-cleaved YBCO6.5, exhibiting an effective hole doping of $p = 0.28$ per planar Cu atom, as determined from the average area of bonding and antibonding CuO_2-bilayer FSs. (b,c) By evaporating potassium on the same sample (< 1 monolayer), electrons are transferred to the topmost CuO_2 bilayer and the corresponding FSs become progressively more hole-underdoped. (c) For heavy K-deposition ($p = 0.11$ as estimated from the area of the chain FS), the E_F ARPES intensity reduces to the 1D CuO-chain FS and four disconnected nodal CuO_2 FS arcs.

modulation of the ARPES features, which seems inconsistent with the sample symmetry, is simply a manifestation of the matrix elements effects associated with the photon/crystal/electron geometry changing across the field of view (no symmetrization was performed). Also, this particular ortho-II sample happened to be twinned, in the bulk and not just on the surface, as confirmed by x-ray diffraction (this has an effect on FS_{Ch} but not on the discussion of the four-fold symmetric Fermi arcs). Most important, the fit of the two-dimensional ARPES FSs over multiple zones returns the following areas, counting electrons, relative to the Brillouin zone area $A_{BZ} = 4\pi^2/ab$: the bonding Fermi surface area $FS_B = 46.2\%$, the antibonding $FS_{AB} = 26.0\%$, and the chain surface $FS_{Ch} = 13.8\%$. From the average of bonding and antibonding FS areas, one can calculate the hole-doping $p = 0.28 \pm 0.01$ per planar copper ($p = 0$ for the 1/2-filled Mott insulator with 1 hole per Cu atom).

As summarized in the phase diagram of Figure 3.5, this indicates that the

self-doping of the YBCO6.5 polar surface is that of a heavily overdoped, non-superconducting cuprate.

The next step is to actively control the self-doping of the surface, so as to reduce its hole content to that of underdoped, bulk YBCO6.5. Several procedures were tried out on these samples in an attempt to suppress the surface contribution to the total photoemission intensity and gain direct insight into the bulk electronic structure. For instance, samples were temperature-cycled between 20 and 100 K or were cleaved at higher temperature ($\sim$80 K) and then cooled down to 20 K [55], in order to age and/or vary the characteristics of the cleaved surfaces. While both procedures have proved successful in measuring the bulk dispersion and FS of layered Sr_2RuO_4 [55], no effect was observed in the case of YBCO6.5. Successful control of the self-doping of the cleaved surfaces was achieved by in-situ deposition of submonolayers of potassium, with a commercial SAES getter source [91], on freshly cleaved YBCO6.5. In this latter case, the samples were kept at 20 K at all times during the cleaving, K deposition, and ARPES measurements (temperature-dependent measurements could not be performed because of the need of maintaining the most stable experimental conditions over extended time, during and between subsequent K evaporations). All ARPES data shown in Figures 3.2, 3.3, and 3.5 were obtained on the same sample, i.e. as-cleaved and after two subsequent K evaporations. Owing to the low ionization potential, K^{1+} ions are adsorbed on the surface and electrons are doped into the topmost layers. As a consequence, we would anticipate the evolution of all detected features towards the underdoped regime of hole-doped cuprates, which is precisely what one can observe in Figure 3.2(a–c) upon increasing the K^{1+} concentration (i.e. decreasing the hole doping). The doping is indeed changing according to an increase in electron filling (all data were acquired on the same sample after subsequent K evaporations). This is evidenced by the continuous FS_{Ch} area increase (counting electrons), which evolves from $FS_{Ch} = 13.8\%$ for the as-cleaved surface to $FS_{Ch}^{K1} = 14.7\%$ and $FS_{Ch}^{K2} = 16.6\%$ for the increasingly K-deposited YBCOK1 (see Figure 3.2(b)) and YBCOK2 (see Figure 3.2(c)). By comparing the carrier concentration per chain-Cu measured by the FS_{Ch} area with the results of ab-initio LDA band structure calculations [79], we can estimate the corresponding hole-doping per planar-Cu. This way we find good agreement with the value $p = 0.28$ already estimated for as-cleaved YBCO6.5 from the average of FS_B and FS_{AB}. Most importantly, however, we obtain a hole-doping $p^{K1} = 0.20$ and $p^{K2} = 0.11$ for YBCOK1 and YBCOK2, which means that the surface of YBCOK2 is very

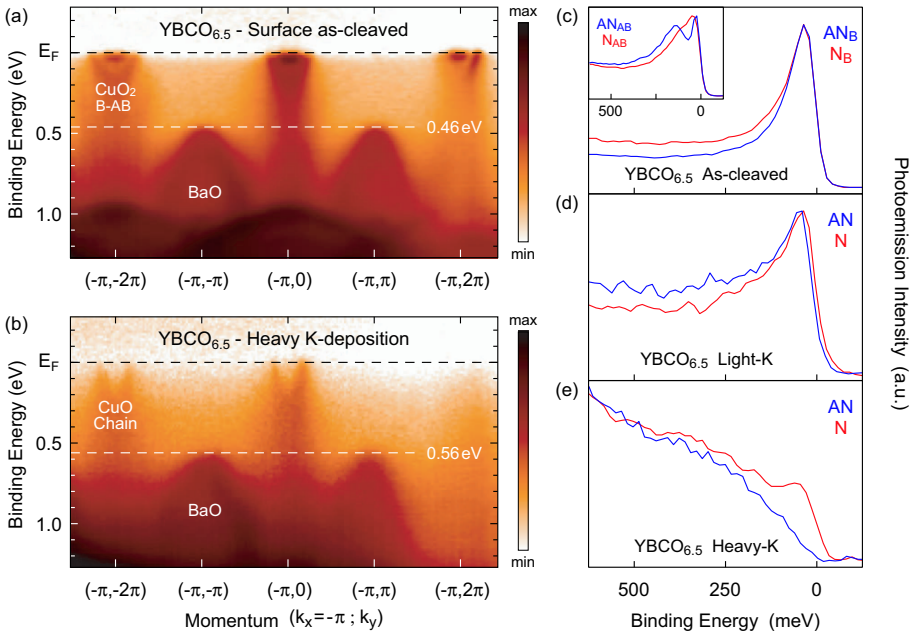

Figure 3.3: YBCO dispersion and EDC evolution upon e^- doping. Energy and angular resolutions were set to ~ 30 meV and 0.2° (±15° angular window), and the sample was at $T = 20$ K. (a,b) The BaO band high-energy shift in YBCOK2 as compared with YBCO6.5 reveals that electrons are added upon K deposition; also, bonding (B) and antibonding (AB) CuO_2 features vanish at the antinodes, and only the CuO-chain band is detected. (c–e) Nodal (N) and antinodal (AN) k_F EDCs showing the progressive opening of an AN gap and loss of CuO_2-plane QP coherence upon underdoping ($\Delta \sim 10$ and 80 meV for YBCOK1 and YBCOK2); the B and AB splitting is resolved only for as-cleaved YBCO6.5.

close to the doping level $p = 0.097$ of bulk YBCO6.5.

3.4 Discussion and conclusions

The most interesting aspect of the data in Figure 3.2 is the evolution of the CuO_2-plane features. For heavy K deposition (see Figure 3.2(c)), the LDA-like CuO_2-bilayer bonding and antibonding FSs of overdoped YBCO have collapsed into four nodal Fermi arcs, consistent with other underdoped cuprates [39, 41, 52]. This is accompanied by the complete suppression of CuO_2 antinodal spectral intensity as well as nodal bilayer splitting, which in contrast were clearly resolved for as-cleaved YBCO6.5 (see Figure 3.2(a)). Their dis-

appearance with K deposition hints at a severe loss of coherence upon underdoping. Correspondingly the CuO_2 nodal Fermi wavevectors, relative to the Brillouin zone diagonal $(0,0)$–(π,π), have evolved from $k_F^{AB} = 0.29$ and $k_F^B = 0.36$ for "overdoped" as-cleaved YBCO6.5, to a single $k_F^{K2} = 0.40$ for "underdoped" YBCOK2. These numbers compare well with what has been observed on other cuprates at similar dopings (note that the following are both single-CuO_2-layer systems): $k_F = 0.36$ and 0.41, respectively, for overdoped ($p = 0.26$) $Tl_2Ba_2CuO_{6+\delta}$ [26] and underdoped ($p = 0.12$) $Ca_{2-x}Na_xCuO_2Cl_2$ [52].

The transfer of electrons to the surface of YBCO upon K deposition is also confirmed by an inspection of the electronic dispersions along the $(-\pi,-2\pi)$–$(-\pi,2\pi)$ direction. On $p = 0.28$ as-cleaved YBCO6.5 (see Figure 3.3(a)) we detect well-defined bonding and antibonding CuO_2 bands crossing E_F at the antinodes, as well as the BaO band with a maximum binding energy at the zone corners $(-\pi,\pm\pi)$. On underdoped $p = 0.11$ YBCOK2 (see Figure 3.3(b)) the BaO band is located ~ 100 meV deeper in energy. This indicates a shift of the chemical potential consistent with the transfer of electrons from adsorbed K atoms to the topmost BaO, CuO-chain, and CuO_2-plane layers. On YBCOK2 the only coherent feature detected at the antinodes is the 1D CuO-chain band; the antinodal CuO_2-plane spectral weight has now become fully incoherent. The nodal and antinodal energy-distribution curves (EDCs) in Figure 3.3(c–e) clearly show that the progressive loss of QP coherence with K deposition is very similar to what is observed on other cuprates upon hole underdoping [26, 39, 41, 52]. Most importantly, while metallic behaviour is observed on as-cleaved YBCO6.5, a leading-edge antinodal gap $\Delta \sim 10$ and 80 meV is detected for YBCOK1 and YBCOK2, respectively. This is consistent with YBCO being superconducting for $p = 0.11$ and 0.20 but not 0.28 (see Figure 3.5—the experiments were all performed at $T = 20$ K) and allows us to conclude that the properties of K-deposited YBCO surfaces are representative of the bulk. The superconducting gaps measured are consistent with ARPES measurements on Bi2212, where the gap is 40 meV for a sample with a T_C of 87K [42].

The analysis of the E-vs.-k ARPES intensity map and EDCs in Figure 3.3 can be extended to the corresponding momentum-distribution curves (MDCs), which confirm the findings from EDC analysis. The MDCs for as-cleaved YBCO6.5, YBCOK1, and YBCOK2 are shown in Figure 3.4. For overdoped ($p = 0.28$) as-cleaved YBCO6.5, the MDCs are characteristic of an anti-nodal signal dominated by bonding and antibonding CuO_2 bands (see Figure 3.4(a)). The single peak at 180 meV corresponds to approximately the bottom of the

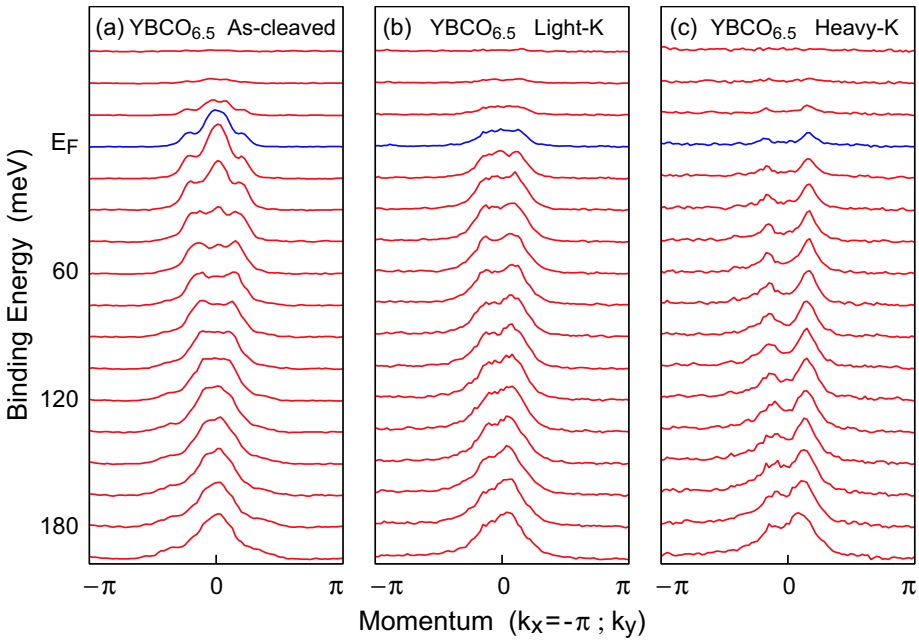

Figure 3.4: YBCO MDC evolution upon e^- doping. MDCs measured on (a) as-cleaved and (b,c) K-deposited YBCO6.5, along the same momentum-space direction of the EDCs shown in Figure 3.3(a,b), yet limited to the $k_x = -\pi$ and $k_y = [-\pi, \pi]$ range. The energy step between adjacent MDCs is 15 meV. Also note that, owing to the relative peak/background intensity decrease upon K deposition, the MDCs for YBCOK1 and YBCOK2 have been rescaled by a factor of 4.4 and 7.2, respectively, with respect to those of as-cleaved YBCO6.5. All spectra were taken at $T = 20$ K.

bonding band and evolves into two symmetric peaks with respect to $k_y = 0$ upon approaching E_F, as expected for a parabolic dispersion. Closer to the Fermi energy ($E_B \lesssim 60\,\text{meV}$), a second, more intense peak is detected, which corresponds to the antibonding band bottom and also splits in two upon crossing E_F. As potassium is deposited on the cleaved YBCO6.5 surface, the peak-to-background intensity ratio progressively decreases (the MDCs were multiplied by 4.4 and 7.2 for YBCOK1 and YBCOK2, respectively). Although the overall background is increasing, the widths of the MDCs are still well defined without evidence of further broadening, suggesting that the doping evolution of the ARPES response is not dominated by disorder arising from the adsorption of potassium. In addition, the intensity associated with the CuO_2 bands decreases, and the CuO chains start instead to dominate the antinodal response (see Figure 3.4(b)). On YBCOK2 the only detectable features come from the parabolic CuO-chain dispersion (see Figure 3.4(c)), which is substantially deeper than that of the CuO_2-plane bands (two distinct MDC peaks are still observable at 180 meV in Figure 3.4(c), as opposed to the single one in Figure 3.4(a)). Finally, the E_F (π,0) weight is progressively decreasing, consistent with the reduction of QP coherence and the opening of the antinodal gap, as discussed in the context of Figure 3.3.

We now summarize our findings, illustrated by the phase diagram and symmetrized FS data for YBCOK2 and as-cleaved YBCO6.5 in Figure 3.5. Our study demonstrates that the self-hole-doping of the cleaved polar surfaces of YBCO can be controlled by the in-situ evaporation of alkali metals, in the present case, K. This novel approach paves the way for the study of this important material family—across the whole phase diagram—by single particle spectroscopies. As this material has been the gold standard in a number of seminal bulk-sensitive studies of the normal and superconducting properties, the direct connection with single-particle spectroscopy can lead to an understandable underdoped anchor point, analogous to $Tl_2Ba_2CuO_{6+\delta}$ in the overdoped regime [30]. The results obtained for $p = 0.11$ YBCOK2 establish that the ARPES FS of underdoped YBCO consists of the superposition of the 1D CuO-chain FS and CuO_2-plane-derived nodal Fermi arcs. It is thus consistent, with the additional complication of the chains, with what has already been observed in oxychloride [52] and Bi-cuprates [39, 41]. In this sense, the disruption of the large holelike coherent FS in underdoped cuprates is a truly universal phenomenon.

Since the first momentum-resolved FS data for underdoped YBCO have been obtained, it has become crucial to understand the connection between

ARPES and quantum oscillation results [13, 15]. First, the detection of the BaO band maximum at $\sim$0.5 eV below E_F rules out the scenario coming from LDA band structure calculations, which suggested that the small Fermi surface found in the quantum oscillation measurements might originate from small pockets produced by BaO-Cu_{chain} bands at $(\pm\pi, \pm\pi)$ [79, 80]. We also did not observe any signature of CuO_2-derived band folding arising from the ortho-II oxygen ordering of the chains [79, 80], which is possibly consistent with the loss of three-dimensional coherence evidenced by the suppression of bilayer band splitting upon underdoping.

Recent measurements of the Hall resistance in high magnetic field have noted a sign change with decreasing temperature [14], suggesting that the quantum oscillations seen on top of a negative Hall coefficient might come from small electron pockets, rather than the hole pockets originally proposed [13]. However, there is no sign of such electron pockets in our ARPES data from underdoped YBCOK2, nor are there signs of additional zone-folding due to the kinds of density wave instabilities that might give rise to such a Fermi surface reconstruction [14, 78, 83].

If any pocket had to be postulated on the basis of the present ARPES data, the most obvious possibility would be that the Fermi arcs are in fact hole-like nodal Fermi pockets, as obtained for light doping of the antiferromagnetic parent compound in self-consistent Born calculations [92] and already speculated from the study of other underdoped cuprates [39, 41, 52]. The lack of a finite ARPES intensity on the outer side of the pockets would be consistent with the strong drop in the QP coherence $Z_{\mathbf{k}}$ expected beyond the antiferromagnetic zone boundary [81, 93]. To estimate an area for these ostensible nodal pockets, we can fold the detected arc profile, either with respect to the antiferromagnetic zone boundary or the end points of the arc itself, obtaining values of either 2.6% or 1.3%, relative to the full Brillouin zone area $A_{BZ} = 4\pi^2/ab$. These numbers compare relatively well with the pocket area of 1.9% suggested on the basis of quantum oscillation experiments on bulk YBCO6.5 [13, 15]. However, these are hole, not electron, pockets. Thus, the interpretation of high field measurements in terms of electron and hole pockets differs markedly from single-particle spectroscopy on the same material, suggesting that the high magnetic field might be inducing a state different from that being studied in zero field.

The YBCO data are the first ARPES results from an underdoped cuprate that has sufficient mean free path to allow for fermiology by bulk-sensitive techniques. Further, the deposition of alkali metals now offers us a tool to progres-

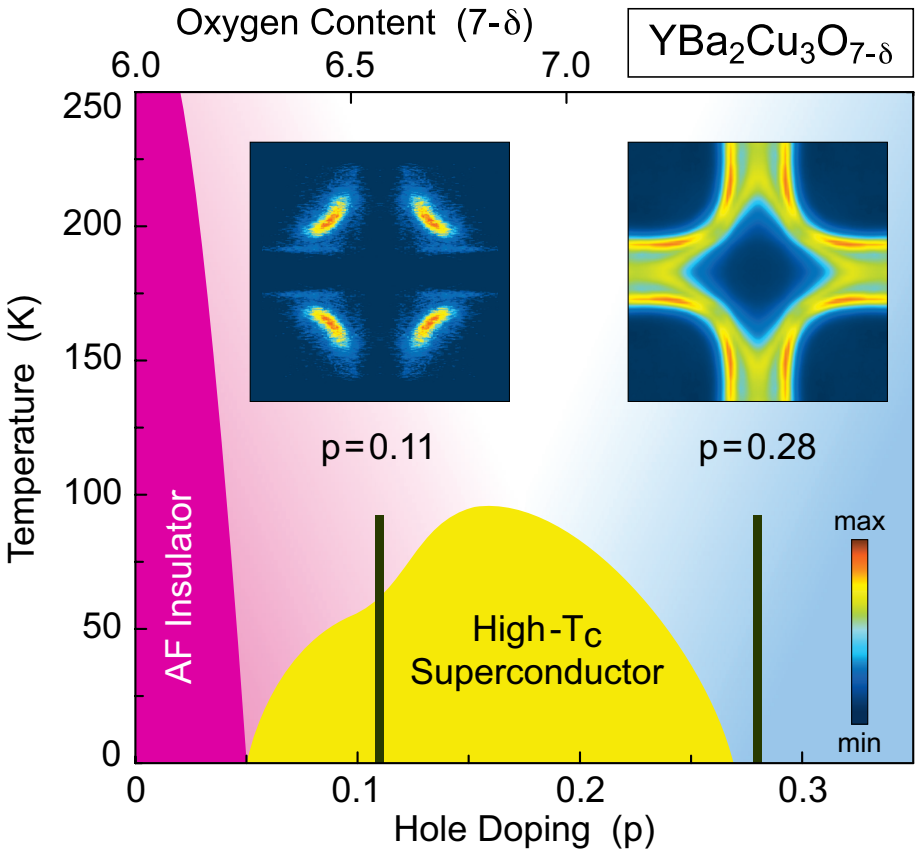

Figure 3.5: Phase diagram of YBCO as measured by ARPES. Schematic temperature-doping phase diagram of YBCO adapted from Doiron-Leyraud et al. [13]. The hole doping p per planar copper ($p=0$ for the 1/2-filled Mott insulator with 1 hole per Cu atom), and the corresponding oxygen content ($7-\delta$), are indicated on bottom and top axes [89]. The ARPES FS for under- and overdoped YBCO is also shown; the momentum-distribution maps have been 2-fold and 4-fold symmetrized for $p=0.11$ and 0.28, respectively. Similar to the data in Figure 3.2, the doping levels were determined for $p=0.11$ from the area of $\mathrm{FS_{Ch}}$, and for $p=0.28$ from the area of $\mathrm{FS_B}$ and $\mathrm{FS_{AB}}$. Energy and angular resolutions were set to ~ 30 meV and 0.1° (±7° angular window) for the FS mappings, which were obtained by integrating the ARPES intensity over a 30 meV energy window about E_F and then normalizing the intensity maps relative to one another for display purposes.

sively underdope any cuprate: whereas previously different levels of doping had to be studied by using different materials—leading to uncertainty in whether changes in ARPES spectral features were a consequence of the doping or of the material itself—we can now follow the evolution of the electronic structure as a function of doping continuously on a single sample. For instance, one could try to underdope the surface of Tl2201, which grows naturally overdoped [30], or even to obtain an electron-doped superconductor starting from the insulating parent compounds.

Chapter 4

Construction of an In-house ARPES System

An in-house ARPES system has been constructed at UBC with the goal of improving both energy resolution (to < 1.5 meV) and angular resolution (to $< 0.2°$), with the highest possible sample positioning accuracy. The progress made is the latest in a series of advances in ARPES instrumentation that have seen dramatic improvements in resolution over the past thirty years. The improvements in resolution over time are shown by Reinert et al. [94] in Figure 4.1.

In addition to working towards improved resolution in all the fundamental aspects of an ARPES system, the UBC ARPES system extends the measurement capabilities of the system by being coupled directly to a molecular beam epitaxy (MBE) system such that samples can be grown and passed directly into the ARPES cryostat without ever being exposed to pressures higher than 5×10^{-10}mbar. Connection to the MBE allows ARPES to be done on the vast array of crystal structures that can be grown by MBE, rather than on the small range of crystals that can be cleaved in vacuo. For instance, CaO and NiO films, with the introduction of appropriate specific point defects, can be used to generate half-metallic ferromagnets and antiferromagnets, which represent a new class of magnetic systems that can now be synthesized and studied using ARPES. Since the samples grown by MBE are inherently thin films, we will be able to study systems with much higher resistivities without the charging problems found in bulk crystals, so long as a conductive substrate is used.

Beyond the advantages offered by a broader range of samples available for study, the MBE-grown samples offer a tuning parameter not available in single crystals—namely, the lattice constants. By choosing substrates with varying lattice constants, the strain, bond lengths, and bond angles of the grown samples are varied accordingly, which allows the lattice constants on the thin films grown

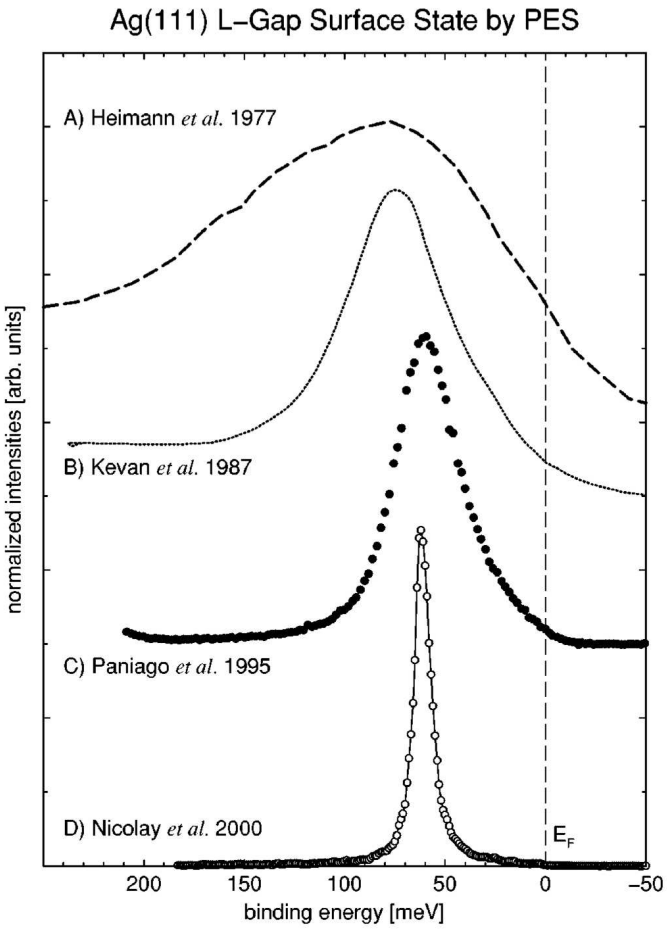

Figure 4.1: Technological development in photoelectron spectroscopy (PES) since the first observation of the Ag(1 1 1) surface state in photoemission spectra: (A) from Heimann et al. [95], measured at room temperature with Ar I ($h\nu =$ 11.83 eV), angle integrated; (B) from Kevan et al. [96], at room temperature with $h\nu = 13\,\text{eV}$, $\Delta E \approx 60\,\text{meV}$, and $\Delta\theta = 1°$; (C) from Paniago et al. [97], at $T = 56\,\text{K}$ with Ar I, $\Delta E = 21\,\text{meV}$, and $\Delta\theta = 0.9°$; (D)from Reinert et al. [94], at $T = 30\,\text{K}$ with He I ($h\nu = 21.23\,\text{eV}$), $\Delta E = 3.5\,\text{meV}$, and $\Delta\theta = \pm 0.15°$. Figure reproduced from Reinert et al. [94].

to be treated as an additional tuning parameter. In ARPES studies of single crystals, there is always a complication in the interpretation of the results due to the difficulty in separating the spectral components associated with the bulk states from those of the surface states. This difficulty is resolved in studies on thin films, as the concepts of bulk states and surface states are ill-defined in the limit of thin samples; all electronic states of the film are accessible from the surface, and all surface states effectively permeate the entire sample, provided the film is only a few unit cells thick.

4.1 Elements of the in-house ARPES system

The fundamental components of an ARPES system are an electron analyzer; a monochromatic photon source; a cryostat that holds the sample at the desired temperature, with a mechanism to change the angle of the sample relative to the analyzer; and a transfer system to introduce and secure the sample in the setup (see Figure 4.2). In most modern ARPES setups, including the in-house system at UBC, angular positioning of the sample is accomplished through a moving cryostat. While analyzer resolutions, cryostat temperature monitoring accuracy, cryostat angle-setting accuracy, and photon source linewidth set a limit on the accuracy of ARPES measurements by the system, the measurements can easily be compromised by a number of other factors, such as the thermal contact between the cold head of the cryostat and the sample itself, the quality of the vacuum, and, most important, residual electric and magnetic fields inside the analysis chamber, particularly those that vary in time. Introducing the MBE to the system provides another design challenge in that the sample grown in the MBE must be able to be passed to the cryostat without exposing the grown surface to any contaminants. The constraints used in designing each of these components are addressed.

4.2 Electron analyzer

To determine the energy and angle of photoelectron emission we chose to use a hemispherical analyzer consisting of two concentric hemispheres between which a centripetal electric field is applied, an entrance hole for the incoming electrons, and an electron detector [98]. In most modern ARPES systems, the electrons enter the hemispheres through a slit array positioned at $r = A$, where A is

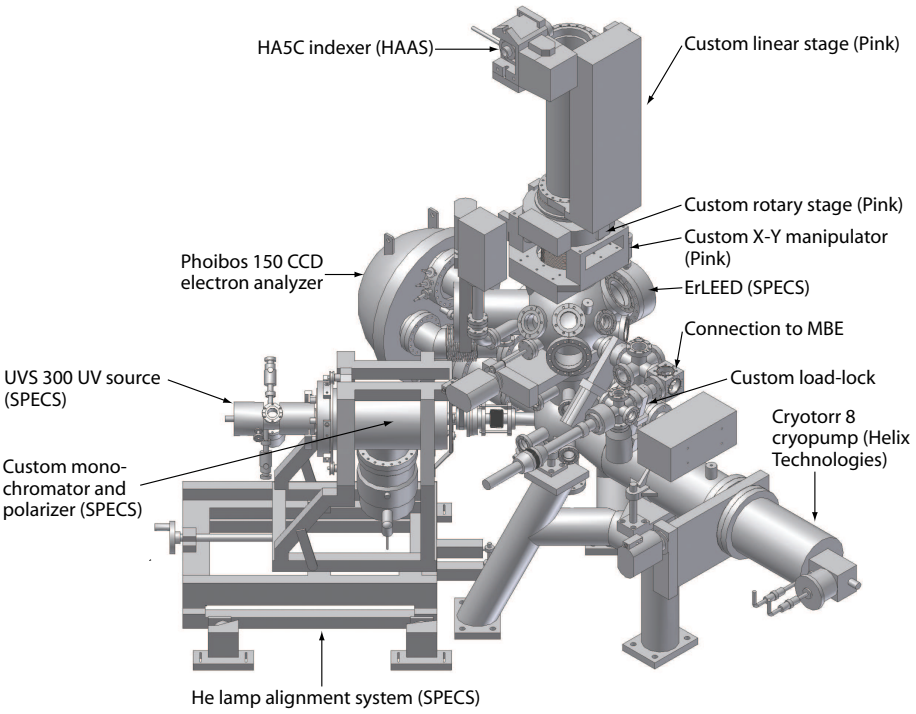

Figure 4.2: The UBC ARPES system (cryostat and transfer system not shown).

the average radius of inner and outer hemisphere, and travel 180° around the hemispheres to an electron detector.

The analyzers in modern ARPES systems, including the ours, differ from those described in Moore et al. [98] in that they have electrostatic lenses in front of the entrance slit, which are used to focus the electrons onto the analyzer entrance slit, as shown in Figure 4.3. The lens system has a major impact on the energy resolution of the system. From the following analysis it can be seen that the theoretical energy resolution is proportional to the so-called pass energy, the kinetic energy required by an electron to follow a circular orbit in the hemispheres. The resolution could, in theory, be made arbitrarily good by having the pass energy approach zero. In practice the fact that count rates decrease with lower pass energies and that the effects of stray electric and magnetic fields become more significant with smaller electron velocities create practical limits to the energy resolution. Nevertheless, to achieve the resolution required to do meaningful data analysis, it must be possible to specify the pass energy at which the electrons are measured. This typically means lowering the kinetic energy of the incoming electrons, which is accomplished by changing the potential in the hemispheres. It is the voltage difference between the hemispheres that sets the pass energy, while the potential energy midway between hemispheres, at the slit, is given by

$$V_{\text{slit}} = \frac{V_1 + V_2}{2} + \frac{V_2 - V_1}{2}\frac{R_2 - R_1}{R_2 + R_1}, \tag{4.1}$$

where V_1 and R_1 are the voltage and radius of the inner hemisphere, respectively, and V_2 and R_2 are the voltage and radius of the outer hemisphere. If the potential on each hemisphere is lowered by an equal amount, δV, the pass energy is unaltered but the potential energy of the electrons in the hemispheres is increased by $e\delta V$. Electrons coming from the sample at zero potential will thus have their kinetic energy reduced by $e\delta V$. By appropriate choice of $e\delta V$ it is theoretically possible to study electrons that exit the sample at an arbitrary kinetic energy at any pass energy.

Without an electrostatic lens system, changing the overall potential of the hemispheres would change the electron trajectories between the sample and the entrance slit, resulting in the analyzer studying different emission angles as the kinetic energy of the incoming electron changed. The electrostatic lens system has its potentials adjusted as the hemisphere voltages change such that the focusing properties of the analyzer are theoretically constant as δV is adjusted

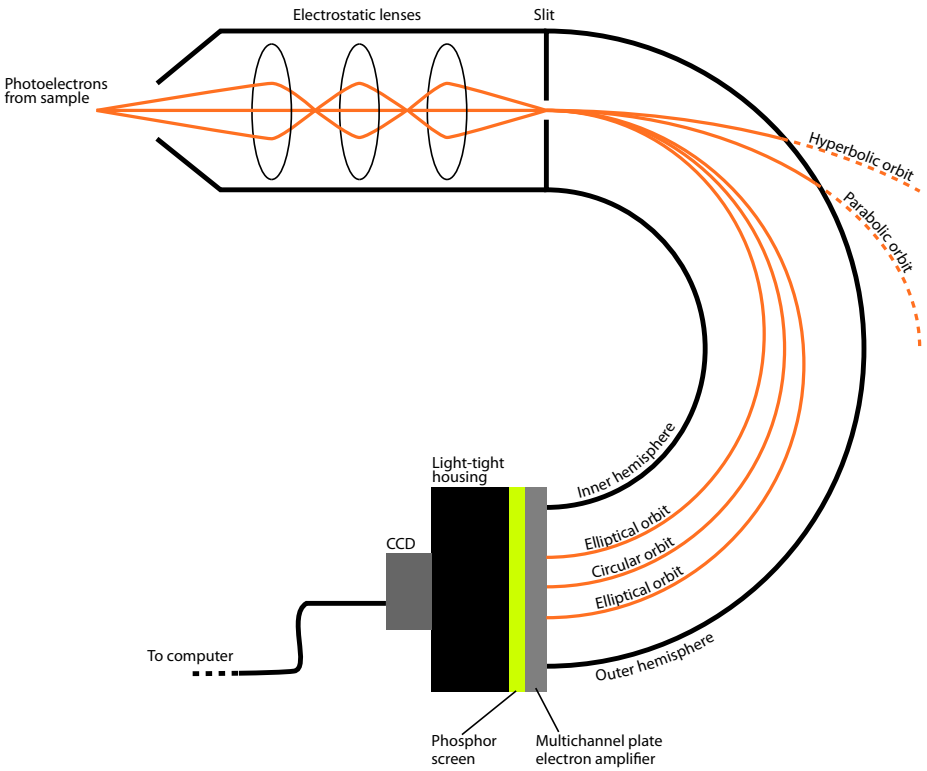

Figure 4.3: Analyzer schematic showing paths of electrons at or near the pass energy and paths of electrons of much higher energy.

to study electrons at different energies.

Another major difference between the analyzers described in Moore et al. and those used in most modern ARPES systems is that the latter have a 2D electron detector, consisting of a double-layer multichannel plate (MCP) [98] to amplify the electron signal, followed by a phosphor screen, onto which the electrons emitted from the MCP are accelerated. A CCD camera detects the light generated by the electrons hitting the phosphor screen. Using a 2D electron detector allows energies moderately above and below the pass energies, as well as electrons coming into the hemispheres at different points along the slit, to be detected. Thus, the energy and emission angle of an electron can be determined by the position at which it is detected.

The analyzer's electrostatic lenses can be used to focus in two modes: magnification and transform. Magnification mode images the sample onto the entrance slit. The electrons that make it through the slit correspond to a so-called cut of position space. The energy spectra of each position along the cut can thus be detected, but no angular information is recovered. Conversely, transform mode Fourier transforms the incoming electrons, focusing emitted electrons at a given angle to a unique location on the slit, regardless of the location of electron emission. A cut along angle space thus enters the hemispheres. In transform mode no spatially resolved information can be obtained, and electron energy spectra as a function of angle along a cut in angle space are obtained. The following discussion refers to transform mode, as it is the relevant mode for ARPES. The discussion of electron focusing pertains to both modes, however.

The hemispheres are each charged and thus create a $1/r^2$ electric field, pointed in the $\hat{\mathbf{r}}$ direction. An analysis of particles acted on by an inverse square force is presented in Fetter and Walecka [99]. We will borrow their formulae. The coordinates used for the following discussion are illustrated in Figure 4.4.

The angular momentum of a particle acting under a central force is a constant of motion; the motion is thus confined to the plane defined by the particle's initial momentum and the origin on the central force. The motion of the electron can be described on polar coordinates. The coordinates are defined such that the electron starts at $\theta = 0$ and that $\dot{\theta} > 0$.

Let A be the distance from the centre of the slit to the centre of the hemispheres. The pass energy (E_{pass}) is defined as the kinetic energy (E_k) required for an electron starting at $r = A$ along $\hat{\theta}$ to follow a circular orbit. We assume throughout the discussion that the electrons have sufficiently low kinetic energy to follow closed orbits; parabolic or hyperbolic orbits could not hit the detector

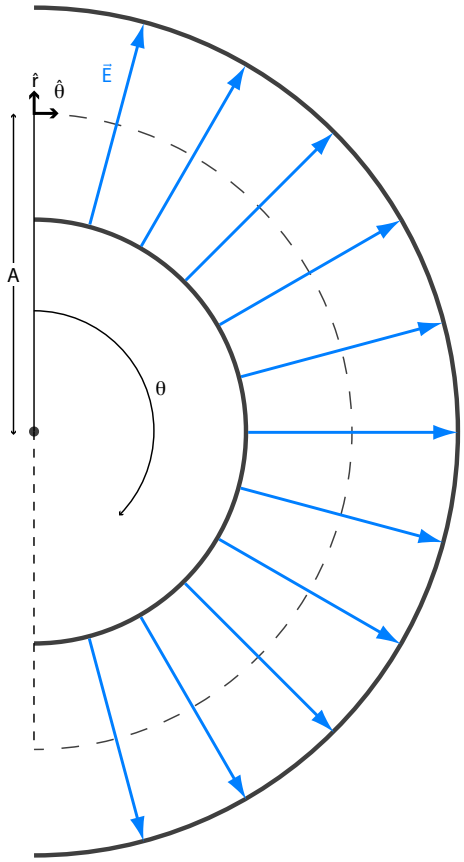

Figure 4.4: Coordinate system used to discuss electron paths in analyzer hemispheres. The coordinate system is centred at the hemisphere centres. The entrance slit is located at $\theta = 0$ and $r = A$.

and thus are not considered. We will first consider an electron emitted along $\hat{\theta}$, which gives a mathematically simple relationship between the kinetic energy of the electron (E_k) and r when $\theta = \pi$. An expression for electrons emitted with at an angle β relative to $\hat{\theta}$ is then derived, which is shown to have second-order dependence on β.

For the case of an electron emitted along $\hat{\theta}$, we exploit the fact that the orbit is either circular or elliptical (see Figure 4.5). An elliptical orbit has a non-zero $\hat{\mathbf{r}}$ velocity component everywhere but at the apsides; the electron enters the hemispheres at one apsis and hits the detector at the other. As a result, the distance from where the electron enters the system to where it hits the detector is the major axis of the ellipse. If we define the potential such that if the $1/r^2$ electric field were continued past the outer hemisphere to infinity, an electron at infinity would have a potential of zero, then the formulae for $1/r^2$ forces relating the kinetic energy and potential energy (U) of an orbit to the length of the major axis are directly applicable [99].

For a circular orbit, $U = -2E_k$. We thus obtain that for an orbit with a major axis of $2A$, $U_{\text{pass}} = -2E_{\text{pass}}$. The total energy of an orbit is inversely proportional to the major axis, and the product of total energy and major axis is thus a constant. By substituting in the values for the circular orbit with kinetic energy of E_{pass}, this constant is found to be $2A(U_{\text{pass}} + E_{\text{pass}}) = -2AE_{\text{pass}}$.

Consider an electron entering the analyzer at $r = A$ with $E_k = E_{\text{pass}} + \delta E$. Let the value of r when $\theta = \pi$ be $A + \delta A_0$. We can exploit that the product of total energy and the major axis is a constant to write

$$(2A + \delta A_0)(-E_{\text{pass}} + \delta E) = -2AE_{\text{pass}}, \tag{4.2}$$

which gives

$$\delta A_0 = \frac{2A\delta E}{E_{\text{pass}} - \delta E}. \tag{4.3}$$

We can see that for small δE, δA_0 will respond approximately linearly. In most analyzers the detector area allows electrons within 5% of E_{pass} to be detected; thus the energy scale changes by 10% over the detector.

For an electron of kinetic energy $E_{\text{pass}} + \delta E$ that enters the hemispheres with a non-zero β, we note that the orbital energy, and thus the major axis of the elliptical orbit, is the same as for an electron of the same energy with no $\hat{\mathbf{r}}$ velocity component. In the following we define δA as above, such that when the

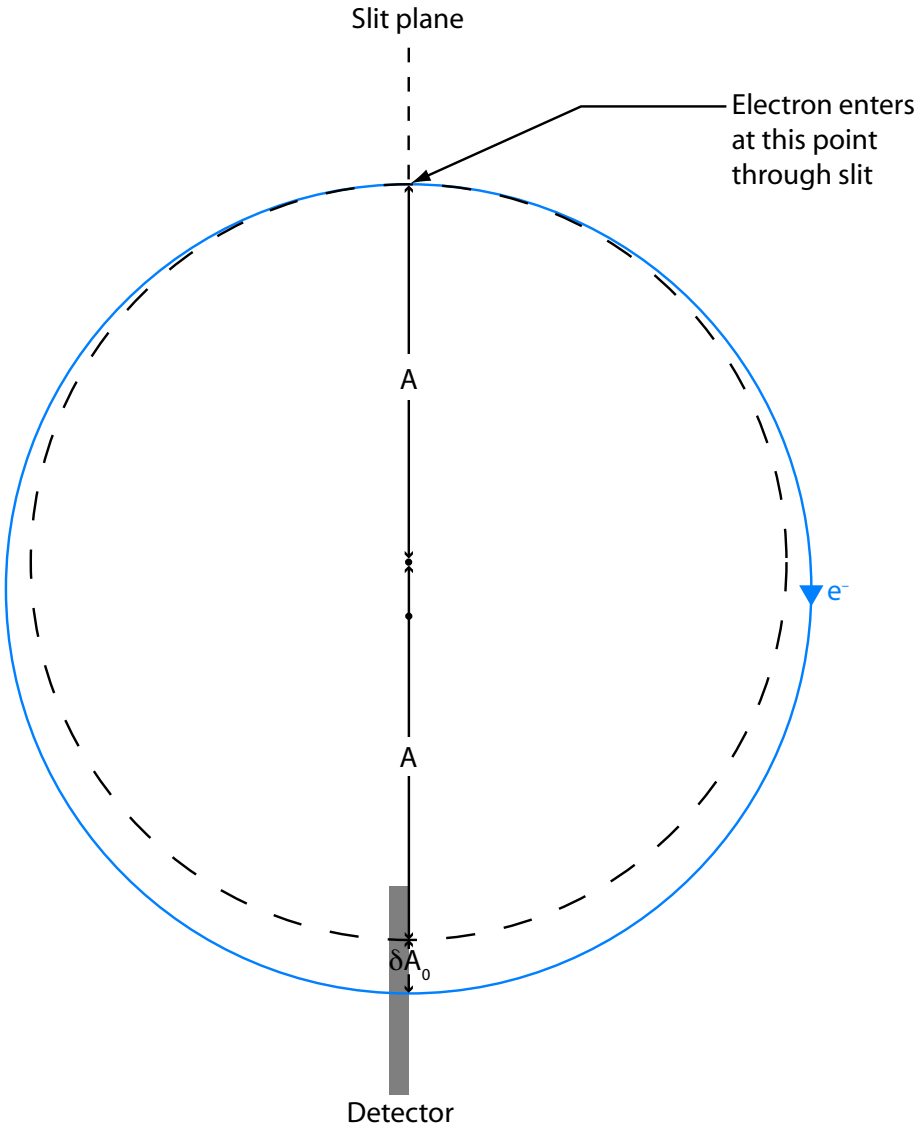

Figure 4.5: Analyzer hemisphere orbits for electrons entering normal to the slit plane. An electron with $E_k = E_{\text{pass}}$ will follow a circular orbit of radius A. An electron with $E_k = E_{\text{pass}} + \delta E$ will follow an ellipse with one focus at the hemisphere centres. Where the electron enters through the slit and the hemisphere centres both lie on the major axis of the ellipse. The electron hits the detector plane at $A + \delta A_0$.

electron is at $\theta = \pi$, $r = A + \delta A$. δA_0 can now be viewed as the value of δA in the $\beta = 0$ case. We show that δA differs from δA_0 as order β^2 (see Figure 4.6).

We then exploit the property that the sum of the lengths of line segments from each focus of an ellipse to a point on the perimeter is equal to the major axis, which is determined by the electron's kinetic energy [99]. As one focus is at the centre of the hemispheres, a distance A from the point where the electron enters, the other focus lies on a circle about the electron entrance point of radius $A + \delta A_0$. The angle formed by the hemisphere centre, electron entrance slit, and second focus of the ellipse is 2β, which is found by holding the the sum of distances to the foci constant along the electron trajectory.[2] The sum of the lengths of the lines from the hemisphere centre to the point where the electron hits the detector and from where the electron hits the detector to the second focus is also $2A + \delta A_0$. From here elementary trigonometry gives:

$$A + \delta A = \frac{(A + \delta A_0)(1 - \sin^2 \beta)}{1 + (1 + \delta A_0/A) \sin^2 \beta}, \tag{4.4}$$

$$\delta A = \frac{\delta A_0 - 2(A + \delta A_0) \sin^2 \beta}{1 + (1 + \delta A_0/A) \sin^2 \beta}. \tag{4.5}$$

Doing a Taylor expansion and neglecting all terms of order $\beta^2 \delta A_0$ and β^4 gives

$$\delta A = \delta A_0 - 2A\beta^2, \tag{4.6}$$

where β is in radians. This expression is second order in β, such that to first order all electrons emitted at one point with the same energy will be focused to the same point on the detector. Further, the β^2 term has a negative coefficient; electrons that enter at such an angle as to make the β^2 term significant will appear as having higher binding energy than they actually do. This is a

[2] The entrance slit is a distance A from the centre of the hemispheres and a distance $A+\delta A$ from the other focus. Let α be the angle formed by the centre of the hemispheres the entrance slit and the second focus. We use Cartesian coordinates with the origin at the centre of the hemispheres and the entrance slit at $(0, A)$. Let L be sum of the distances from the foci to a point (x, y). $L = \sqrt{x^2 + y^2} + \sqrt{(x - (A + \delta A_0)\sin(\alpha))^2 + (y - A + (A + \delta A_0)\cos(\alpha))^2}$. We differentiate L along $\hat{\beta}$. $\frac{dL}{dl} = \sin\rho\cos\beta - \sin\varphi\cos\beta + \cos\rho\sin\beta + \cos\varphi\sin\beta = \sin(\beta + \rho) + \sin(\beta - \varphi)$, where ρ is the angle formed by the entrance slit, the centre of the hemispheres and (x, y) and thus $\rho = \tan^{-1}\frac{x}{y}$. Similarly, φ is the angle formed by a line through the centre of the hemispheres and the entrance slit and a line through the second focus and (x, y) and thus $\varphi = \tan^{-1}\frac{(A+\delta A_0)\sin\alpha - x}{y - A + (A+\delta A_0)\cos\alpha}$. Since along an electron orbit the sum of distances from the foci to a point on the orbit is a constant, we set $\frac{dL}{dl} = 0$, which gives $\beta = \frac{\varphi - \rho}{2}$. At the slit, $\rho = 0$ and $\varphi = \alpha$, giving $\alpha = 2\beta$.

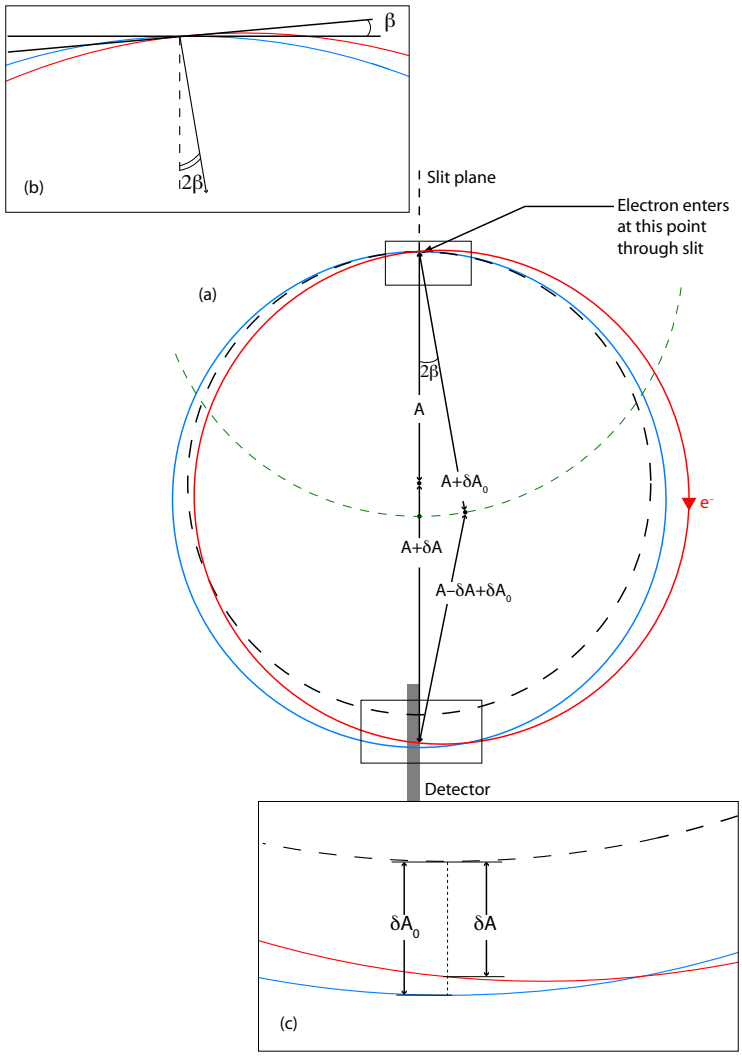

Figure 4.6: Analyzer hemisphere orbits for electrons entering off normal to the slit plane. The difference in detected position from the $\beta = 0$ orbit scales as β^2. (a) The combined lengths of two line segments connecting a point on the ellipse to the foci is equal to the semi-major axis, which is equal to $2A + \delta A_0$. Applying this property twice gives a triangle whose lengths can be solved to give δA, as in Equation 4.3. (b) Enlarged inset showing the relationship between β and the angle formed by the line segments extending from the slit to the foci. (c) Enlarged inset showing the difference between δA and δA_0.

far better scenario than the converse, where higher–binding energy electrons could end up promoted to the Fermi level. Practically, β can be controlled to make the effects of the β^2 term smaller than other contributions to the energy resolution: a smaller entrance aperture at an image plane in the lenses blocks electrons emitted away from the analyzer focus from reaching the slit. The slit is a transform plane, and the angle of electron incidence on the slit is directly proportional to the spatial distribution at the image plane and hence the size of the aperture.

Distilling the above, we arrive at a relationship (neglecting β^2 terms) between the incoming electron kinetic energy, the pass energy, and position on the detector plane. In the discussion above, we defined a set of coordinates relative to the location of the incoming electron, which was not pinned to any aspect of the analyzer geometry other than A; given a curved slit of radius A, the kinetic energy of the electron determines the distance from the hemisphere centre, and the location on the slit determines the angle α. Energy and angular coordinates are naturally orthogonal (see Figure 4.7).

Slits of radius A are not used, however. At first glance, the results from a slit of radius A would not be entirely intuitive to interpret: the data would be collected along a curved cut through angle space, and the Fermi edge would appear circular. Ideally the user would be presented with a flat Fermi edge, and the cut through angular space would be flat. Achieving these properties simultaneously is not possible with the focal properties of a hemispherical analyzer. Each can, however, be obtained with an appropriate slit shape. With a flat slit, the cut of angle space is flat. The direct correspondence between polar angle of the where the electron emerges from the slit and where the electron hits the detector is not affected, but the relationship between energy and radius now changes as a function of polar angle. The Fermi surface has a radius of curvature approximately equal to $A/2$. Consider electrons entering along the straight slit, all of the same energy, but at different locations along the slit. Each will have the same orbital energy, and hence the same major axis, but the value of r along the slit is not constant; $r = A/(\cos\alpha)$. The major axis of each electron orbit is $2A + \delta A_0$, so the distance from the origin of the detected electron is $2A + \delta A_0 - A/(\cos\alpha)$.

Conversely, electrons with $E_k = E_{\text{pass}}$ entering a curved slit described by $r = 2A - A/(\cos\alpha)$ will arrive at the detector at $r = A/(\cos\alpha) + \delta A_0$. When $\delta A_0 = 0$, this is a straight line. This is the standard curved slit provided on analyzers; for the remainder of the discussion "curved slit" will refer to this

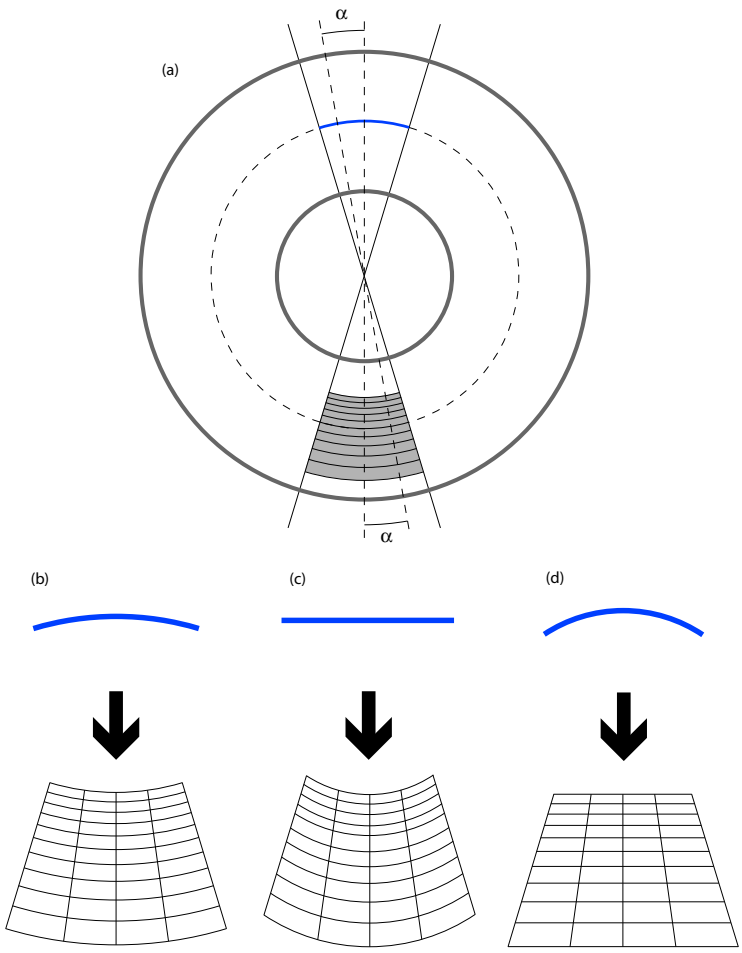

Figure 4.7: The effect of analyzer slit shape on the detected electron distribution. In all drawings, the lines depicting different electron energies represent a uniform energy spacing. (a) For all slit types, the electron will land on the slit plane 180° from where it passed through the entrance slit. The radial location will be a function of E_k/E_{pass} and, for slits not concentric with the analyzer centre, the location at which the electron passed through the slit. (b) Electrons entering the analyzer through a concentric slit will be focused onto concentric rings of equal energy. The position the electron entered along the entrance slit and energy thus are on an orthogonal coordinate system. (c) Electrons entering through a straight slit at the pass energy will land on a curve with twice the curvature of those from a concentric slit. (d) Electrons at the pass energy entering through a slit described by $r = 2A - A/(\cos\alpha)$ will land on a straight line.

geometry unless otherwise noted. For non-zero values of δA_0, the deviation from a straight line is $(1 - 1/\cos\alpha)\delta A_0$, which is second order in α but first order in δA_0. A curved slit is thus a good approximation to an arc of radius $A/2$ about a centre located at $(A/2, 0)$ for small α. The corresponding cut through angle space is thus approximately twice as curved as for the hypothetical slit of radius A.

While a slit of radius A provides neither a flat cut through angle space nor a flat Fermi edge, it does provide data on polar coordinates, which are orthogonal. A straight slit provides a straight cut in momentum space but a doubly curved Fermi edge, while the standard curved slit provides a flat Fermi edge, provided δA_0 is small. Both straight slits and curved slits provide data on non-orthogonal coordinate systems. They both also create more astigmatism than the conceptual $r = A$ slit, as the electrons at the far ends of the slit experience much stronger fringe effects (see Figure 4.8). This astigmatism and non-orthogonality of coordinates become progressively more significant as analysis on ARPES data become more quantitative and as the resolution of ARPES systems increases.

Scienta electron analyzers have long been the workhorses of modern ARPES systems [6]. They feature intentionally chromatic electrostatic lens elements that focus electrons with higher kinetic energies more tightly such that the entrance slit spans a greater angular range than for electrons with lower kinetic energies; in so doing the electron positions on the detector appear on a rectangular coordinate system with one axis denoting energy and the other axis denoting angle. In fact, although the image at the detector is still trapezoidal when using the standard curved slits, the coordinate grid itself is Cartesian. Moreover, Scienta analyzers also have lens elements that can be used to shift the effective focus, allowing the user to correct misalignment between the focus of the light source and the analyzer focus. Although these features are convenient, they are sources of astigmatism.

Our system uses the Phoibos 150 CCD analyzer, manufactured by SPECS, which has emerged as a competitive high-resolution electron analyzer. The Phoibos 150 presents several advantages. First, it uses a double layer of μ-metal[3] shielding to screen external magnetic fields and uses titanium fasteners, which do not display ferromagnetism regardless of their history, inside the analyzer

[3] μ-metal is a high-permeability alloy used for magnetic shielding. Its use is detailed by Jiles [100]. The field in the chamber is measured to be 2 mG. As the chamber is single layer as opposed to the analyzer's double shielding, the analyzer field can safely be assumed negligible compared to that of the chamber.

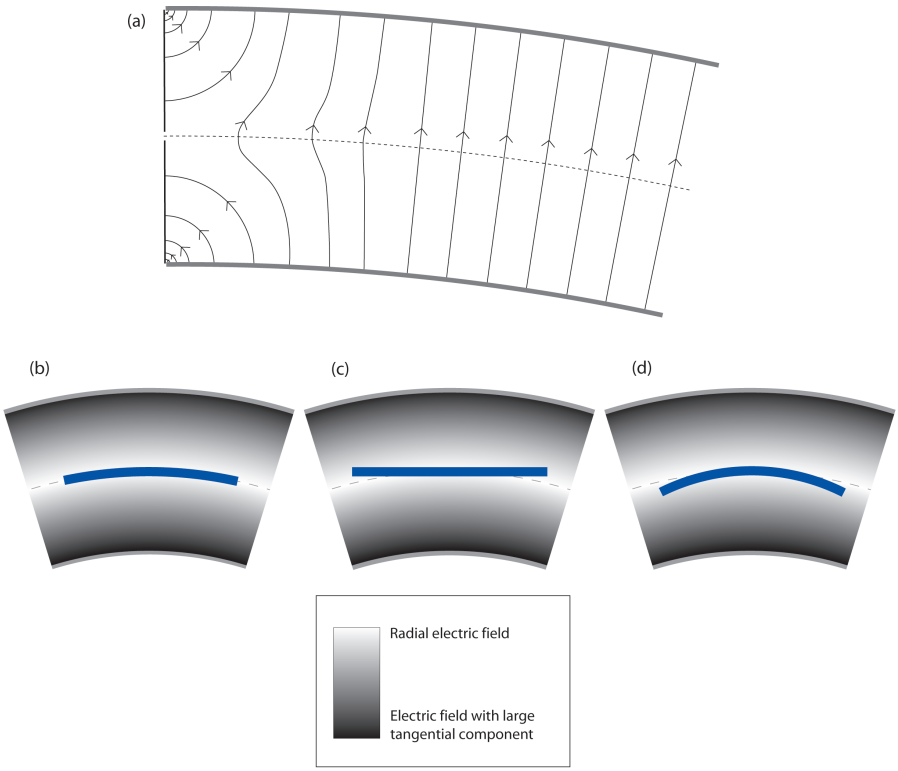

Figure 4.8: (a) Electric field inside the hemispheres, near the slits. The slit plane is at a uniform potential, and hence there are strong fringe fields towards the corners where the hemispheres near the slit plane. The slit plane is normal to the page, coincident with the face of the hemispheres. (b) Electrons leaving a concentric slit will experience only a radial electric field, and the field will not depend on the location along the slit at which the electron entered. (c) Electrons entering through a straight slit will encounter different amounts of non-radial electric field as a function of where on the slit they entered the hemispheres. (d) Electrons entering through the conventional curved slit will also experience different electric fields depending on where they were emitted along the slit.

body to ensure that the lowest possible residual magnetic fields are maintained. Second, the Phoibos 150 uses machined hemispheres, as compared with the traditional formed hemispheres.[4] Formed parts have much lower tolerances than machined parts [102] and introduce anisotropic strain in the formed metal [101], which can allow formed parts to deform as they stress-relieve over time, thus degrading analyzer accuracy.

A unique feature of the SPECS analyzers is the approach taken with regards to interpretation of the positions of electrons reaching the 2D detector. Rather than using lens elements to physically steer the electrons to produce a rectangular coordinate system at the detector, the SPECS system simply outputs the electron map in its unadulterated keystone shape. With appropriate software, these data can be converted to a rectangular coordinate system. However, with the absence of the extra lens elements, the Phoibos 150 does not have the ability to shift the analyzer focus.

We, in collaboration with SPECS, developed software that allows the characterization of the analyzer response function. This response function is inverted, allowing the software to return an intensity plot with angle and energy as linear and orthogonal coordinates. This procedure greatly simplifies analysis of the data and is done in real time such that those performing the experiments can see clearly what they are measuring.

4.2.1 Analyzer resolution

Test reports for our Phoibos 150 CCD electron analyzer show an ultimate angular resolution of 0.11° and an ultimate energy resolution of 1.0 meV. Since analyzer resolution is strongly affected by stray electric and magnetic fields within the analysis chamber, the analyzer was tested in our analysis chamber, in its final mounting position, to ensure that the measured resolution can in fact be realized in practice.

The testing apparatus for angular resolution consisted of an electron gun, a stainless steel target, and a slit array (see Figure 4.9). Electrons emitted from the surface of the target pass through the slit array and into the analyzer. The slits have a width of 100 μm and are placed 35 mm from the target, corresponding to an angular opening of 0.16°. The full width at half maximum (FWHM) of the beam from the SPECS EQ 22/35 electron gun is reported to

[4] Scienta hemispheres have the distinctive marks from the shear spinning forming process [101].

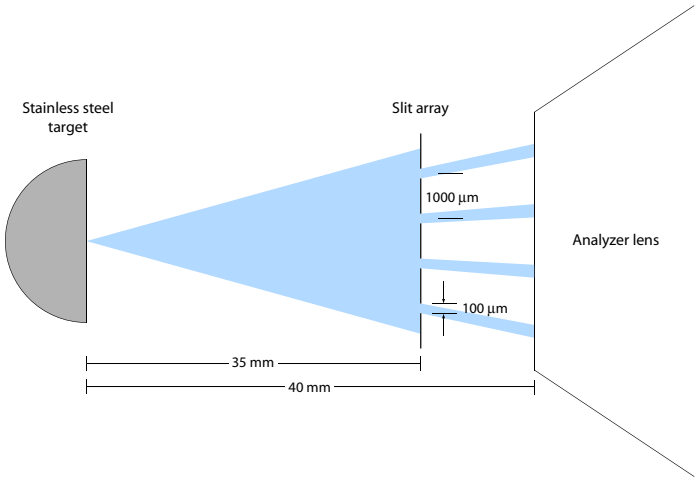

Figure 4.9: Schematic diagram depicting the analyzer angular resolution test apparatus. Electrons from an electron gun scatter off the stainless steel target and pass through the slit array before entering the analyzer.

be as small as 50 μm, corresponding to an angle of 0.08°, but measuring the electron spot size at the time of testing was not possible. The smallest FWHM for the image of the slit detected by the analyzer during testing was 0.21°. Let $F_{\text{ang res}}$, $F_{\text{meas ang}}$, F_{slit} and F_{e^-} be the FWHMs of the analyzer angular resolution function, measured angular distribution, angle formed by the slits, and the angular distribution of the electron spot size. Subtracting the contributions to this measured angular width due to the minimum electron spot size and the slit width gives an analyzer electron resolution of 0.11° according to the following equation:[5]

$$F_{\text{ang res}} \approx \sqrt{F^2_{\text{meas ang}} - F^2_{\text{slit}} - F^2_{e^-}}. \tag{4.7}$$

Note that this value represents the worst $F_{\text{ang res}}$ could be, since, without a direct measurement of the spot size from the electron gun, it is impossible to know with certainty that the gun was optimized to produce the reported minimum spot size.

To produce monochromatic electrons for the energy resolution test, Xe atoms were bombarded with He emission. The He lines have a FWHM, F_{He}, of 1.0 meV,

[5]The equation would be exact if it used the standard error instead of the FWHM. In ARPES analysis it is usually not practical to use standard error. It is difficult to subtract the background from the feature of interest reliably enough to get a reproducible standard error.

and Doppler broadening of the Xe target gas, F_{Xe}, introduces a 3.3 meV width to the energy of the emitted electrons. Considering the contributions of the He and Xe widths, the FWHM of the emitted electron linewidth, $F_{\mathrm{meas\ E}}$ as measured by the Phoibos 150 CCD of 3.6 meV corresponds to an analyzer energy resolution, $F_{\mathrm{energy\ res}}$ of 1.0 meV, as given by:

$$F_{\mathrm{energy\ res}} \approx \sqrt{F^2_{\mathrm{meas\ E}} - F^2_{\mathrm{He}} - F^2_{\mathrm{Xe}}}. \tag{4.8}$$

This calculation, however, does not take into account the stray electric and magnetic fields produced by the Xe gas cell. The gas cell confines the Xe electromagnetically, producing oscillation fields, which are detrimental to the analyzer resolution. The gas cell is designed such that these fields are mainly cancelled outside of the gas volume, but whatever residual fields reaching the analyzer will have a negative effect on energy resolution. As a result, the true value of $F_{\mathrm{energy\ res}}$ could be better than the 1.0 meV quoted.

The impressive results of these tests not only indicate the potential of the Phoibos 150 CCD for ARPES studies but also demonstrate good shielding by the μ-metal analysis chamber.

4.3 Helium lamp and monochromator

The UBC ARPES system uses a helium lamp—the UVS 300, manufactured by SPECS—as its UV source. The UVS 300 can produce a photocurrent of 200 nA[6] and has a linewidth of 1 meV. Photons from the UVS 300 enter a custom polarizing monochromator, also made by SPECS. In order to expose the sample to maximal intensity, the photons from the monochromator are conveyed via a copper capillary to within 5 mm of the sample. The interior of the capillary is elliptical, to preserve polarization.

The unique feature of the monochromator assembly is that it allows the polarization to be rotated—which is accomplished by rotating the entire assembly of lamp, monochromator, and associated pumps about the capillary axis—while under vacuum. Our source delivers a 500 μm spot, more than 90% polarized (see Figure 4.11(a)).

To illustrate the importance of having control over polarization, we show the effect polarization can have in matrix-element effects and how polarization

[6]The specification refers to the photocurrent induced on a plate onto which all the UV beam is directed. As photoelectrons leave the plate, the current delivered to the plate to keep it at a constant potential is measured.

control can be used to gain insight from matrix-element effects. We consider the following experimental geometry: the axis of the analyzer lenses and the vector normal to the sample surface define a plane orthogonal to the sample surface. First, we observe that the final state, ${\psi_f}^{\mathbf{k}}$ must have even parity with respect to the plane defined by the analyzer and sample normal in order to have a non-zero intensity on the analyzer-sample normal plane, and thus at the analyzer. We will therefore only consider final states with even parity.

We first consider a linearly polarized photon, with polarization vector on the analyzer-sample normal plane, interacting with a state, ${\psi_i}^{\mathbf{k}}$, that has odd parity with respect to the analyzer-sample normal plane (see Figure 4.10(b)). The polarization vector of the incoming photon, and hence the vector potential, contains only in-plane coordinates and thus is symmetric with respect to the analyzer-sample normal plane. Consider the form of the matrix element

$$M_{f,i}{}^{\mathbf{k}} = \langle (\psi_f)^{\mathbf{k}} | H_{int} | (\psi_i)^{\mathbf{k}} \rangle = \langle (\psi_f)^{\mathbf{k}} | - \frac{e}{m} \mathbf{A} \cdot \mathbf{p} | (\psi_i)^{\mathbf{k}} \rangle. \tag{4.9}$$

We now have an even operator acting on an odd initial state, and an even initial state, resulting in an odd integrand, and thus

$$M_{f,i}{}^{\mathbf{k}} = 0. \tag{4.10}$$

With polarization perpendicular to the analyzer-sample normal plane, and an odd initial state, we have an odd operator acting on an odd initial state, giving an even integrand and a matrix element that is not in general zero (see Figure 4.10(c)).

Similarly, with an even initial state, polarization in the analyzer-sample normal plane gives a matrix element that is in general non-zero see Figure 4.10(d)), but polarization perpendicular to the plane makes the matrix element zero (see Figure 4.10(e)).

In general, the incoming photon is not in the analyzer-sample normal plane and the initial state is not even or odd with respect to the analyzer-sample normal plane. The general case does not have simple criteria for determining when the matrix element will be zero, but rotating the polarization does typically have large effect on the matrix elements and thus on the photoemission intensity. In a typical photoemission experiment on a system with correlated electrons, the spectrum from each band is relatively broad such that the signals from two or more different bands strongly overlap with each other. The matrix element for each band will in general behave differently as the polarization

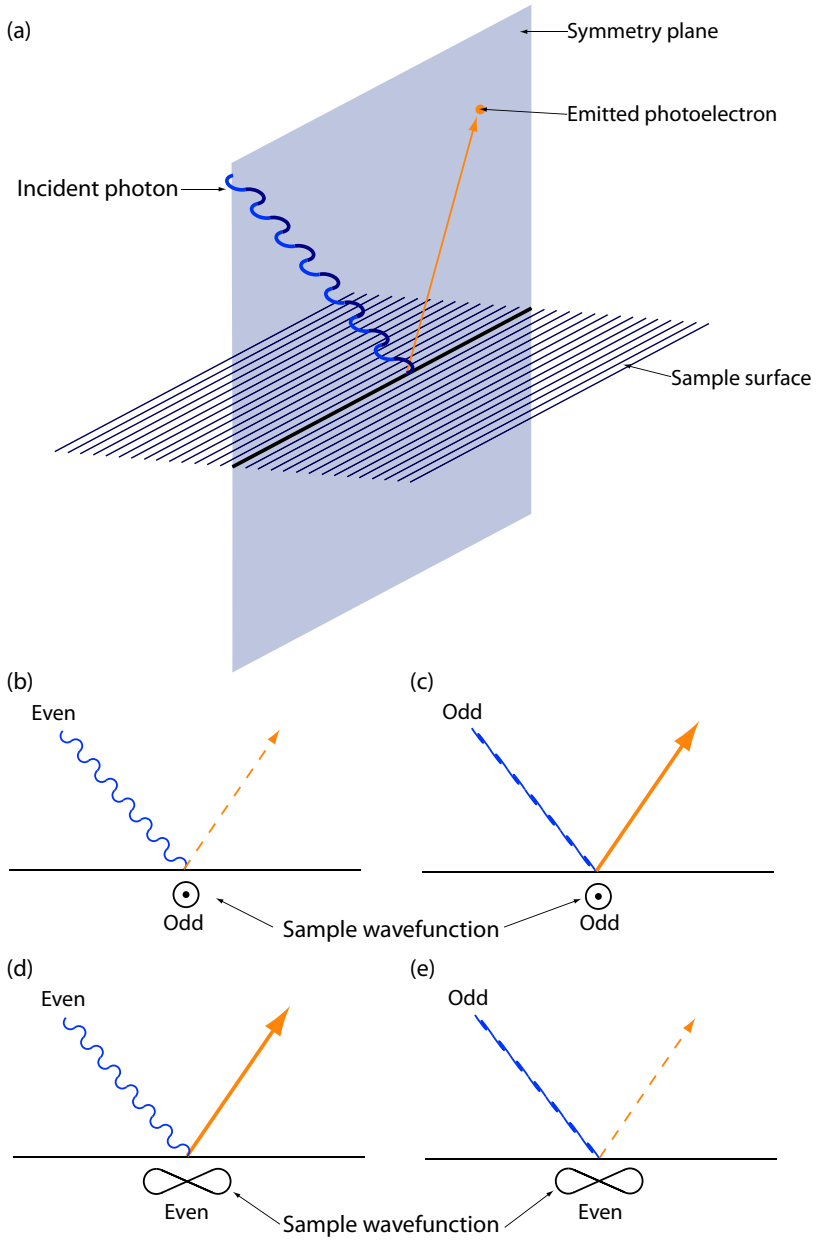

Figure 4.10: (a) Symmetry arguments can be made only if the incident photon and outgoing electron trajectories define a plane normal to the sample surface. (b-e) Conditions for zero (dashed arrow) and non-zero matrix elements (solid arrow).

changes, allowing the contributions from each band to be disentangled.

Polarization control has been done only recently at synchrotron beamlines with the development of elliptically polarizing undulators, and never in a lab-based system. Durr et al. [103] use synchrotron radiation with rotatable polarization to investigate polarization and photon energy effects on the spectra from $Sr_2CuO_2Cl_2$, which is an undoped antiferromagnetic cuprate of significant scientific interest. Approaching *d*-wave superconductivity from the charge transfer insulating antiferromagnetic undoped state may provide insights on the pairing mechanism in high-T_C superconductivity. Some aspects of these measurements were repeated using our lab-based ARPES system, which serves to demonstrate the potential of our system to both understand and profit from polarization effects. The ARPES spectra shown in Figure 4.11(c) for the high-T_C cuprate $Sr_2CuO_2Cl_2$, which was previously aligned in situ by LEED and verified in its stoichiometry by XPS (see Figure 4.11(b)), provide a beautiful demonstration of the power of our instrument.

The rotation of the entire UV source and monochromator system must be precisely aligned such that the photon spot coincides with the analyzer focus throughout the range of motion. To ensure that the spot does not precess during rotation, the aiming of the monochromator needs to be adjustable within the rotating portion of the frame. Once the spot is adjusted to not precess, the aiming of the entire rotating assembly needs to be adjusted to coincide with the analyzer focus. This alignment must take the form of a rotation about the vacuum flange to which the monochromator mounts, in order to prevent mechanical damage to the delicate polarization-preserving capillary tube and the coupling of the monochromator to the chamber. The 380 kg mass of the system forces another design departure from existing ARPES systems. Rather than having the lamp and monochromator manipulated through a port aligner, the entire system is supported and aligned through an external structure. To align the system without damaging the capillary and flex coupling between the monochromator and chamber, the angular motion of the system must be about the centre of the flex coupling (see Figure 4.12).

This system, which includes the helium lamp, monochromator, and two turbopumps suspended on two stainless steel rings, was designed in collaboration with SPECS. The rings are mounted on bearings and geared to be driven by a stepper motor. The mounting of the monochromator assembly to the rings is adjustable, to facilitate aligning the output beam to the axis of rotation.

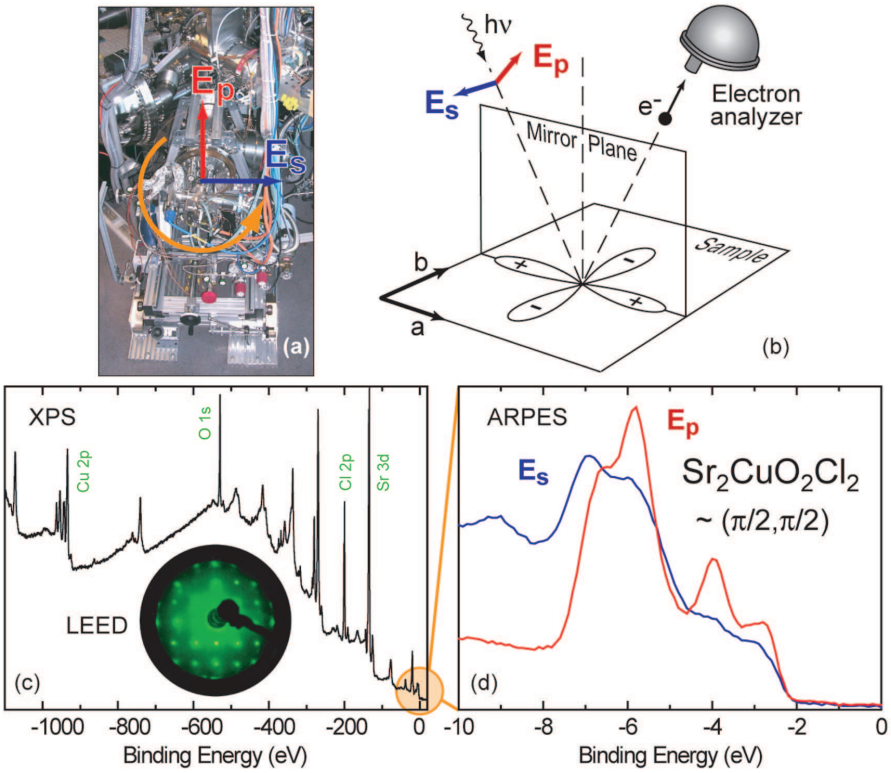

Figure 4.11: A demonstration of light source polarization effects on $Sr_2CuO_2Cl_2$ spectra. (a) Rotatable, polarized UV photon source. (b) Sketch of experimental geometry showing the plane used to define state symmetry in the text. (c) Core-level x-ray photoelectron spectroscopy (XPS) data and low-energy electron diffraction (LEED) from $Sr_2CuO_2Cl_2$. (d) Polarization-dependent ARPES data measured at the nodal point k=(π/2,π/2) by rotating the lamp around its axis as in (a). The strong dependence of the ARPES signal reveals the symmetry of the electronic states, as sketched in (b).

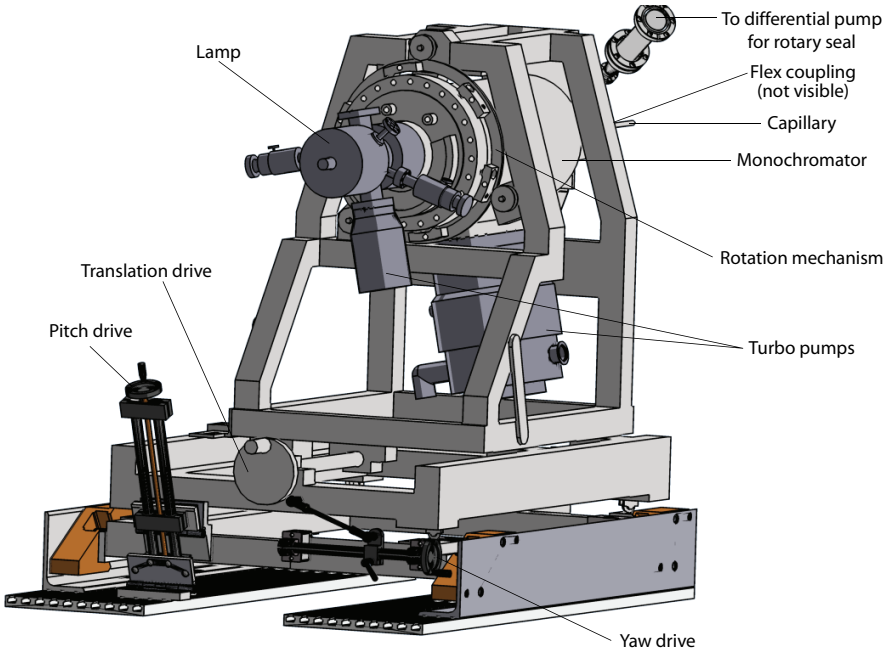

Figure 4.12: The lamp and polarizing monochromator are rotated by a precise multi-axis alignment system. The rotation takes place about the centre of the flex coupling joining the lamp to the chamber, which is coaxial with the capillary. The view of the flex coupling is blocked by the frame.

4.4 Cryostat and manipulator

The cryostat and manipulator present major design challenges. The ideal cryostat and manipulator combination allows the sample to be accurately positioned (at the focus of the analyzer while maximizing overlap of the photon beam on the sample), at an arbitrary temperature, without introducing any stray electric or magnetic fields and without contaminating the vacuum. Further, we must be able to set the angular position of the sample with at least two angular degrees of freedom to an accuracy higher than the resolution of our analyzer (0.11°). A third angular degree of freedom is also desirable. Although such a third degree of freedom would seldom be used mid-measurement, it would be useful for sample alignment.

A flow cryostat and manipulator for the UBC ARPES system have been designed and constructed (see Figure 4.13) through a joint initiative between the UBC Quantum Materials group and Quantum Technologies, a Vancouver-based scientific instrument manufacturing firm specializing in cryogenics. The cryostat is a major step forward in ARPES technology. It can hold the sample to any temperature between 2.7 K and 300 K, and it has two angular degrees of freedom that are accurate to within 0.01 degrees. Further, the sample holder can be rotated about its axis manually, with direct feedback from the LEED to accomplish sample alignment. The cryostat structurally consists of a top flange with a 1.5" stainless steel tube extending down into the vacuum space. This tube is brazed onto a copper tube with an external flange mid-length, which attaches to the cold shield. Brazed to the lower end of the copper tube is another capped stainless tube. The bottom area is the phase separator where the liquid helium collects. Helium that has vaporized while going through the transfer line rises from the phase separator and establishes a thermal gradient up to the top of the cryostat. The flange on the middle copper section provides the mechanical and thermal connection to the cold shield.

The flip stage, where the sample holder is clamped, pivots on bearings mounted to the cold shield. The motion is actuated via a rod coupled to the back of the flip stage by another bearing. The control rod is thermally tied to the cryostat body and couples to the outside through a bellows. Copper braids are clamped to the flip stage on one end and to the reservoir on the other to achieve a thermal link.

Although ARPES cryostats are cooled by liquid helium, which has a boiling point of 4.2 K, most existing ARPES cryostats are only able to achieve sample

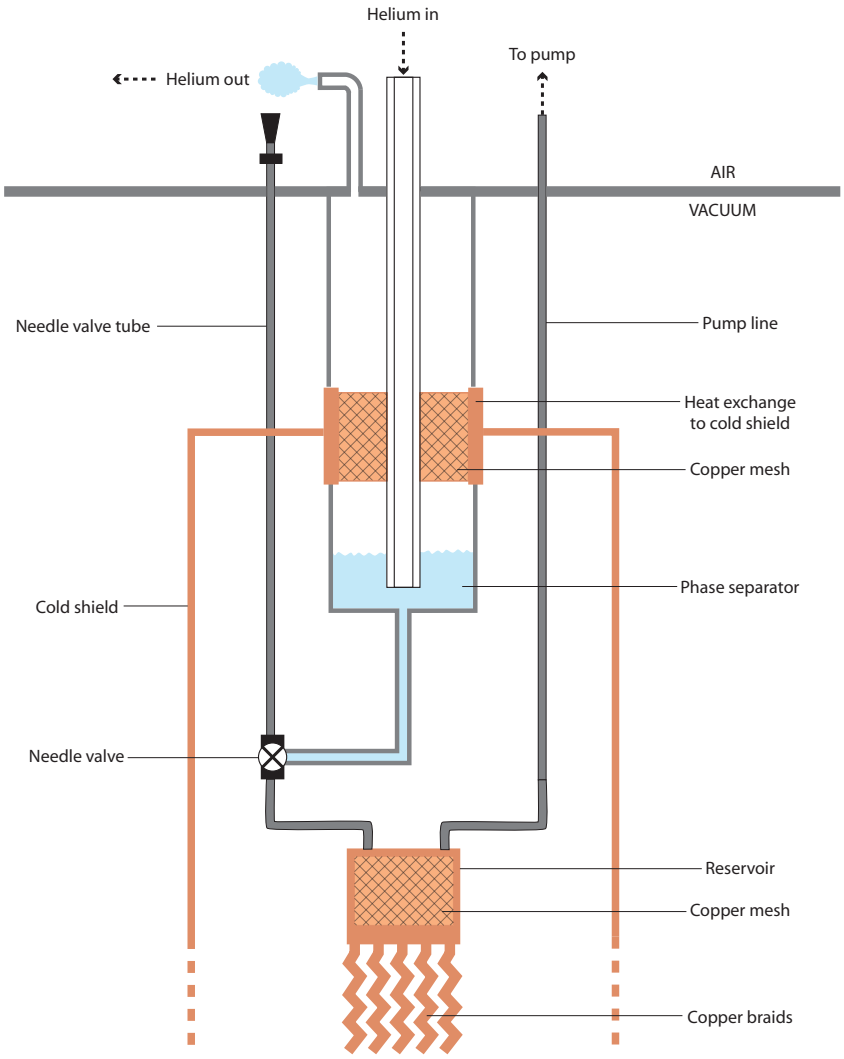

Figure 4.13: Cryostat schematic. From the phase separator liquid helium goes down to the pumped reservoir and gas goes up to cool the shield and maintain a thermal gradient up to the top of the system. The reservoir is thermally connected to the flip stage through gold-plated copper braids.

temperatures of $\sim 15\,\mathrm{K}$. The experiments in Chapter 2 and Chapter 3 were both done at state-of-the-art facilities and reached minimum sample temperatures of 10 K and 20 K, respectively. The challenge in cryostat design therefore lies not only in mitigating the effects of sources of heat external to the cryostat but also in pinpointing the sources of temperature gradients between the cold head and the sample and minimizing their effects.

Thermally insulating the flip stage from external heat that can travel through the control rod or pivot points has been achieved by choosing appropriately insulating cryostat materials (see §4.4.2). However, the cold head is connected to the sample entirely through copper components, the thinnest of these—and hence most potentially thermally insulating—being the copper braid. The temperature difference from one end of the copper braid to the other, based on the conductivity of copper, typical braid lengths and thicknesses, and the heat load on the sample should be less than 1 K. As a concrete example, a sample with a 10 mm square exposed to 300 K radiation will absorb at most 46 mW. This is found by setting the emissivity to 1 in the Stefan-Boltzmann law. The conductivity of oxygen-free high-conductivity copper at 4 K varies considerably depending on the crystallinity of the copper, but 320 W/mK is a safe lower bound [104]. Using a 15-cm-long braid with a cross-section of $25\,\mathrm{mm}^2$ gives a temperature difference of 863 mK.

Thermal gradients should be similarly small along the copper walls of the cold head, the flip stage, and the sample holder. The fact that most existing cryostats typically have a 10 K or more temperature difference between the cold head and the sample suggests that the bulk of the gradients appear across the contacts between these various elements.

Salerno and Kittel [105] reviewed the literature on the thermal conductivity of physically clamped joints at low temperatures and in vacuum and discovered that the parameters with the most significant effects were material constants, surface cleanliness (i.e. free of not only non-native contaminants but also oxide layers), and clamping force. Surface flatness, smoothness, and area were shown to have little to no effect on thermal conductivity of oxygen-free high-conductivity copper [106] within experimental resolution. Thus, our aim in our cryostat design was to make our clamped surfaces inoxidizable—by gold-plating our copper braids and their mating surfaces on the cold head and the flip stage—and to maximize clamping force at all of the joints. The copper braids are crimped into copper lugs, which are bolted onto the helium reservoir and flip stage. All the contacts, including the copper braids, are gold plated.

As well, the method for clamping the sample holder to the flip stage allows for far more clamping force than previous designs.

The coordinate convention followed in the description of the cryostat is as follows: the x- and y-axes are parallel to the ground. x represents translation perpendicular to the analyzer lens, while y represents translation along the axis of the analyzer lens. z represents vertical translation. θ represents rotation about the z-axis; the sample is normal to the analyzer when $\theta = 0$. x, y, z and θ motion are controlled with the xy stage manufactured in-house and with custom θ- and z-stages manufactured by Pink Vacuum. ϕ represents rotation about the x-axis when $\theta = 0$, and the ϕ-axis rotates with θ. ω represents rotation about the normal to the sample, and hence, the ω-axis rotates with both θ and ϕ. ϕ rotation is controlled by a CNC indexer, manufactured by HAAS, while ω rotation is accomplished manually. θ and ϕ are meant to be actuated continually during measurements, while ω is meant to define the orientation of the sample and thus is set at the beginning of a measurement (see Figure 4.14, 4.15).

4.4.1 Cooling and temperature control

Cryostat cooling is provided by liquid helium. Liquid He enters the cryostat through a transfer line into a phase separator. Helium gas is exhausted from the top of the phase separator, where it is used to cool the heat shield, and exits the system. Liquid He leaves the bottom of the phase separator, through a flow-controlling needle valve, and travels to the cold head via a tube. Exhaust He gas from the cold head is returned via a second tube. The cold head is thermally linked to the flip stage by gold-plated copper braids (see Figure 4.16).

In a system with a significant heat load, there can be a significant difference between the temperature of the cold head and the liquid helium contained inside. The Leidenfrost effect [107] prevents direct physical contact between the liquid and the walls of the cold head. In room-temperature liquids the Leidenfrost point is on the order of 100 K greater than the liquid's boiling point. In liquid helium the low latent heat of vaporization results in a Leidenfronst point of less than 2 K above the boiling point, at atmospheric pressure [108]. At a temperature difference of 2 K, the heat flux is only 0.19 W/cm^2. In order to ensure that the cold head can get below the Leidenfrost point, the effective surface area of the helium space in the cold head was increased by filling the cold head with copper mesh.

In the UBC cryostat, copper braids are used as a thermal conductor from

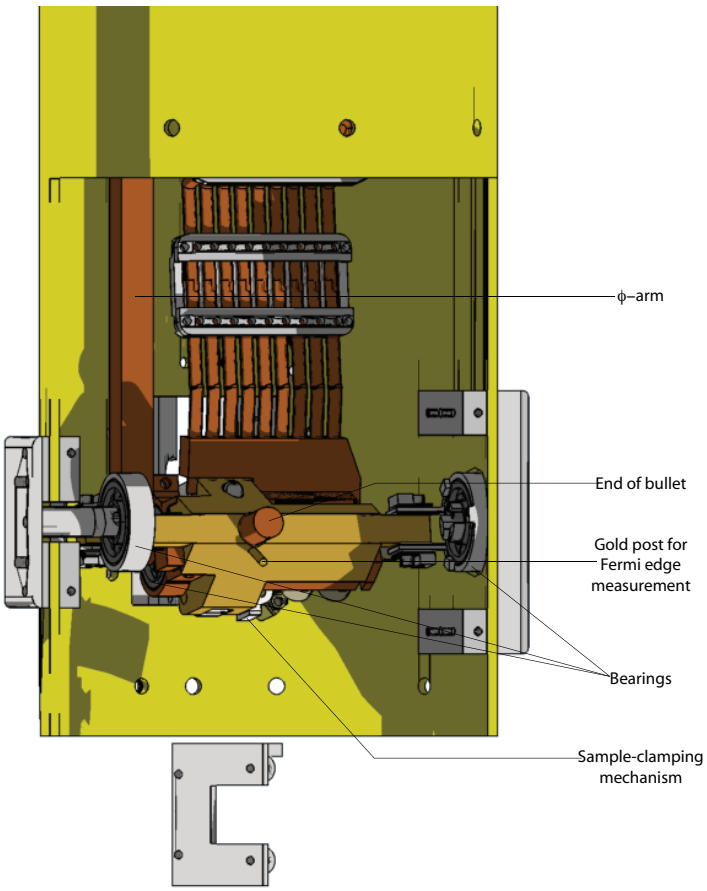

Figure 4.14: Cryostat bottom. (Front plate of cold shield omitted. The holder for the tungsten wire used for angular resolution tests is affixed to the front plate.)

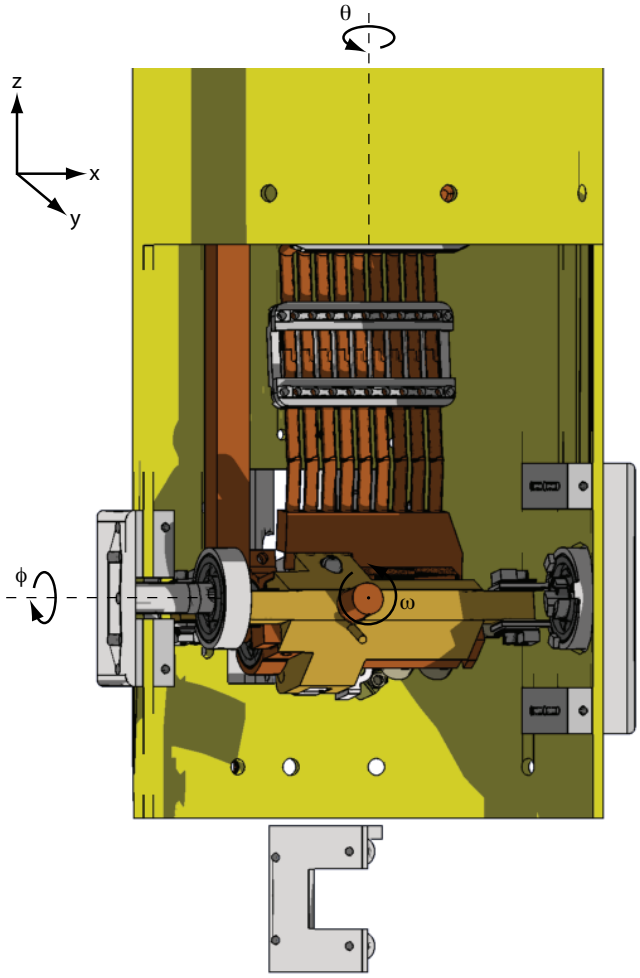

Figure 4.15: Coordinate system for cryostat motion.

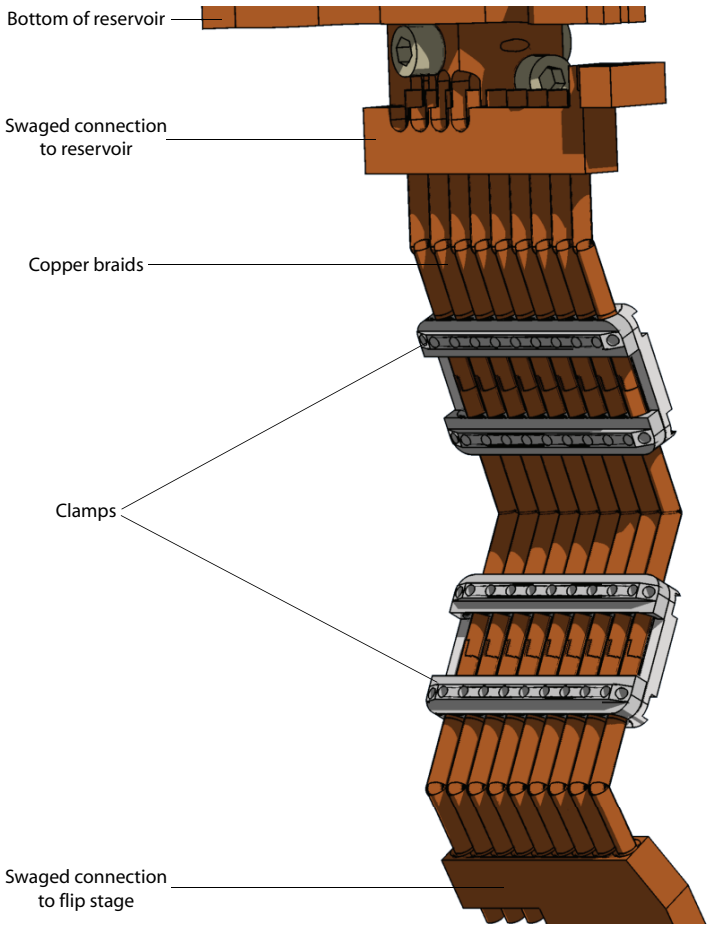

Figure 4.16: The copper braids thermally linking the cold head to the flip stage are gold plated and swaged into gold-plated copper fittings on both sides of the connection. The braids are clamped together with two aluminum plates, which keep the bending of the copper braids during flip stage motion predictable and away from the cold shield walls.

the liquid helium reservoir to the cold flip stage. This method of cooling has been used extensively in ARPES cryostats previously. The connections to these braids are usually made by clamping. The thermal resistance of the clamped connections is typically much larger than that of the copper braids themselves. At low temperatures, in vacuum, the resistance of the thin copper-oxide layer on the surface of the braids and the clamping surface is much greater than the resistance of the braids themselves [104, 105]. In order to reduce the thermal resistance of the connections to the braids, both the braids and their mating surfaces were gold plated. The gold-plated braids were then swaged into gold-plated holders, which are bolted in place to form a demountable connection. The gold-plated surfaces do not oxidize and thus provide an optimal thermal contact.

A four-wire resistance measurement was performed on the completed assembly, from the reservoir to the sample holder, showing that 80% of the electrical resistance—and hence at least 80% of the thermal resistance, by the Wiedemann-Franz law [109]—came from the braids themselves as opposed to the joints.

Diode temperature monitors are attached to the cold head and to the inside of the phase separator, which also contains a liquid-level sensor. Non-inductively wound heaters are located inside the phase separator and on the flip stage. Below 4 K, the phase separator is filled with liquid, and only the heater on the flip stage is used to control the temperature. The helium exhaust is pumped on in order to reduce the liquid temperature to 2 K. At higher temperatures, liquid helium entering the cold head could undergo explosive boiling, resulting in temperature instability. Thus, above 4 K, the heater in the phase separator is used to eliminate liquid helium such that cooling of the cold head is done by gaseous helium.

4.4.2 Cryostat materials

Materials used in the construction of the cryostat must be UHV (ultra-high vacuum) compatible and must not produce any stray electric or magnetic fields. These constraints greatly limit the range of materials that can be used. The small range of UHV-compatible engineering materials—a few types of glass, some metals, some ceramics, and a small number of other materials [98]—is further reduced by the magnetic field restrictions, which are more stringent than would first appear: many materials that are not magnetic at room temperature

undergo a magnetic transition at cryogenic temperatures. Insulating materials also have to be used with caution; if they can be hit with photoemitted electrons, they will charge and thus introduce stray electric fields. The parts of the cryostat that move have even more stringent requirements: of the UHV-compatible metals appropriate for dynamic contact, which is needed for the angular positioning of the samples, most are not ferromagnetic at room temperature but undergo a ferromagnetic transition as they cool to temperatures appropriate for ARPES measurement, thus precluding their use. On top of these constraints, materials chosen must have the right thermal properties—either good conducting or insulating behaviour—depending on their locations in the cryostat. Further, the thermal expansion coefficients of candidate materials must be considered to ensure that the system is not distorted as the cryostat temperature changes, to prevent deformation and failure of components and to ensure that the sample position and angle are not affected by adjustments in temperature.

Away from the reservoir and flip stage, temperatures are not as low—therefore, ferromagnetic transitions are less likely, and the presence of small magnetic moments is acceptable. Thus, for system components away from the cold head, 316 stainless steel and UNS C10200 oxygen-free electronic copper were chosen for their vastly different thermal conductivities [104], with UNS C10200 having a thermal conductivity at all relevant temperatures more than 1000 times greater than 316 stainless steel. Further, the coefficients of thermal expansion of these materials are matched to within 10% at all relevant temperatures [110].

Near the cold head, temperatures are sufficiently low that stainless steel could undergo a magnetic transition if it were used; thus, it must be abandoned as a material choice. UNS C10200 is also abandoned in favour of the higher-purity alloy UNS C10100, as the conductivity near the sample is more critical. Titanium, 6061-T6 aluminum alloy, and beryllium-copper are all used for smaller high-strength components in this area.

The bearings used for the θ rotation also presented demanding material constraints. To maintain UHV compatibility, the bearings cannot be lubricated. This restriction already presents a challenge for the bearing material, since in vacuum, galling and cold welding occur readily without lubrication [98]. Further, the bearings have to provide a reliable thermal break between the heat shield on which they are mounted, which is maintained at $\sim$80 K, and the cold head, which is designed to cycle between 2 and 300 K. The bearings must also be able to withstand the differential thermal expansion between the inner and

outer races at different temperatures. On top of these requirements, the bearing must also be non-magnetic.

Si_3N_4 ceramic is used as a bearing material for applications requiring resistance to thermal shock and is non-magnetic, although it does have a high thermal conductivity. Nonmetals do not suffer from the galling and cold-welding problems faced by metallic bearing surfaces, and outgassing in ceramics is generally not a problem [98]. In vacuum, however, the bulk of the thermal resistance of composite objects is often due to the thermal contact between components. The conductivity of a physical contact between two materials gets progressively better as the yield strength of the softer material decreases. Conversely, Si_3N_4 ceramic is extremely hard (80 Rockwell C), so it is not unreasonable to expect the contact area, and hence the thermal conductivity, between two Si_3N_4 mating surfaces to be small despite the high thermal conductivity of the bulk material.

Cerobear manufactured custom Si_3N_4 607 ball bearings[7] with titanium cages for construction of the flip stage. We measured the heat flow across a Si_3N_4 608 bearing with inner and outer races at 66 and 4 K, respectively, with a mechanical load equal to the weight of the flip stage, and found the heat flow to be 10 mW, rendering the heat load from the bearings much less than the calculated heat load from thermal radiation onto the sample.

4.4.3 ϕ angle manipulation

The ϕ angle is set by a HAAS HA5C CNC indexer, which has a positioning accuracy of 0.008°. The top bar of the parallelogram and the indexer are mounted on top of the manipulator, outside of the vacuum. The moving vertical parallelogram arm is coupled to the vacuum space by edge-welded bellows, while the cryostat body and heat shield act as the stationary arm. The flip stage itself acts as the lower parallelogram arm. The coefficients of thermal expansion of the vertical parallelogram arms are matched, and the arms are thermally tied together in numerous places to ensure matching temperatures, thereby removing differential thermal expansion problems from the vertical arms of the parallelogram. Analysis of the angular error caused by bearing clearances and differential thermal expansion not already taken into account are non-trivial, but even the most conservative analysis indicates that it is irrelevant compared with the angular resolution of the analyzer.

[7] 607 and 608 refer to standard bearing unit sizes [111].

4.4.4 z translation

z motion is accomplished by a relatively standard manipulator. The differences between stock manipulators and the custom z-stage manufactured by Pink is mainly size. In order to minimize bending of the cryostat from uneven heat loads and to hold the complex θ-manipulation system, a comparatively large diameter of 100 mm was chosen for the cryostat, which necessitated a larger z-stage. Further, the 21.8 kg mass of the CNC indexer, hanging over the edge of the manipulator, is large enough to distort the stock manipulators and degrade the angle-setting accuracy. Two massive 40 mm columns provide the Pink manipulator with the necessary stiffness. The z-stage is equipped with a linear scale to allow computerized motion control.

4.4.5 θ rotation

Because of the size and weight requirements imposed by the CNC indexer and the z-stage, the θ–rotation stage requires a larger bore and greater mechanical strength than standard rotation stages. Unlike normal rotation stages, where the load is placed on the seals, resulting in rapid seal wear, high rotation forces, and limited load-bearing capacity, the bearing force of the Pink stage is supported by a 220-mm-diameter 4-contact ball-bearing. The θ-stage is driven by a worm gear/worm mechanism and is equipped with a rotary encoder mounted on the worm for computerized motion control.

4.4.6 $x - y$ translation

The $x - y$ motion is manually actuated. Like the z- and θ-stages, it is larger than commercially available stages. It is also equipped with linear encoders, although they are not used for feedback. In order to accommodate the larger stresses as a result of the large off-axis load and the vacuum pressure from the larger-area bellows, crossed cylindrical linear bearings are used, and in order to provide more robust and backlash-free positioning, ball-screws and ball-nuts are employed [112].

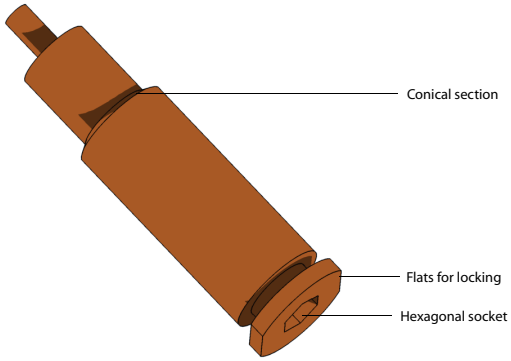

Figure 4.17: The copper "bullet" sample holder. The conical portion of the sample holder is driven into the flip stage by a screw-actuated mechanism. The bullet is manipulated by the hex socket and concentric hole. Bullets with varying final diameters have been fabricated; bullets are chosen to match the sample size, minimizing the detection of electrons emitted from materials other than the sample.

4.4.7 Sample holder and ω rotation

Samples are mounted on a "bullet" (see Figure 4.17). For maximal thermal conductivity, the bullet is a single piece of copper.[8] It is designed to be mountable in any rotational position so that the crystal axes of the sample can be aligned with the axes of the ARPES system, and hence the bearing surfaces of the bullet are rotationally symmetric. The bullet's main features are a conical section that can be driven into a corresponding conical portion of the flip stage, a retaining groove, and an enlarged back section with two flats. At the back of the bullet is a long hole down the axis and a shorter co-axial hexagonal hole nearer the surface. A vacuum ball-end hex key screwdriver installed onto the chamber can positively couple to the hexagonal hole and be used to rotate the bullet—and hence the sample—along the ω-axis.

The design of the bullet not only allows for it to be forcefully clamped onto the flip stage to maximize thermal conductivity, but it also allows for the sample holder to be held from the rear, a requirement imposed by the system's integrated MBE. Any mechanism attempting to grab an MBE-grown sample

[8] For high-temperature applications in the MBE system, molybdenum bullets were also made.

from the front would outgas and contaminate the sample.

Bullets for use in the MBE would have a substrate, affixed to the face with silver paste, onto which the sample would be grown. During growth, the sample must be heated and its temperature must be determined. Our system uses a CO_2 laser to heat the sample and a two-colour pyrometer to measure sample temperature. The bullet is well-suited to both of these applications: the hole at the rear of the bullet can be coated with Aerodag, a spray-on graphite emulsion that dries to UHV levels, making the hole, owing to its long aspect ratio, an effective blackbody. Hence, virtually all of the laser's energy incident on the hole goes into heating the bullet. Moreover, since the 10-μm light from the laser does not go through the pyrometer window, we can perform pyrometry directly off the blackbody and thus measure a reliably reproducible temperature.

Since the bullet must be grabbed from the rear, the flip stage was also designed to accept samples from the rear, which offers unique opportunities. Having an unobstructed view of the front of the sample allows the use of low-energy electron diffraction (LEED) to monitor the orientation of the sample while the sample is rotated from the rear, allowing accurate sample positioning. Further, mechanisms for firm clamping of the bullet into and retraction of the bullet from the flip stage can be mounted to the back of the flip stage without interfering with electron trajectories.

At the back of the flip stage is a block of aluminum that serves to drive the bullet into the flip stage. On one side it is connected to the flip stage with a hinge, and on the opposite side is a screw that clamps the block firmly into the back of the flip stage, driven by the same vacuum screwdriver that can be used to rotate the bullet. Using a screw allows for much more clamping force to be applied compared with conventional spring mounting used in most other ARPES systems. The torque used to rotate the screw is the sum of torque due to friction between the cap of the screw (titanium) and the aluminum clamping block, and the torque from the screw threads. The relationship between load on a screw and the torque required to move it is given by $\tau_t = Q \times r \times \frac{2\pi\mu_t r + p}{2\pi r - \mu_t p}$ [113] where p is the pitch of the screw, r is the pitch diameter, and μ_t is the coefficient of friction between the titanium screw threads and the mating gold-plated copper internal threads. The torque from the friction between the screw cap and the aluminum block is an elementary calculation:

$$\tau_c = \int_0^{2\pi} d\varrho \int_{R_1}^{R_2} P \times R \times \mu_c \, R \, dR = \frac{2}{3}\pi P \mu_c (R_2^3 - R_1^3), \qquad (4.11)$$

where R_2 and R_1 are the radius of the head of the screw and the radius of the hole the screw passes through, respectively, and P is the pressure between the screw head and aluminum block.

The load on the screw, Q, is given by $Q = \int_0^2 \pi \int_{R_1}^{R_2} P\, R dR = \pi P(R_2^2 - R_1^2)$

Solving for P and subbing into (4.11), we get

$$\tau_c = \frac{2}{3} Q \mu_c \frac{R_2^3 - R_1^3}{R_2^2 - R_1^2}. \tag{4.12}$$

Adding τ_c and τ_t and solving for Q gives

$$Q = \frac{\tau}{\frac{2}{3}\mu_c \frac{R_2^3 - R_1^3}{R_2^2 - R_1^2} + r\frac{2\pi\mu_t + p}{2\pi r - \mu_t p}}. \tag{4.13}$$

Examination of this expression shows that the clamping force falls as p, μ_t, μ_c, r, R_1, and R_2 increase.

For our system, we are using a 10-24 titanium alloy (Ti-6Al-4V) screw, which bears on an aluminum surface and engages gold-plated copper threads. The relevant coefficients of friction are not readily available in the literature for these materials in vacuum at cryogenic temperatures.

In general, coefficients of friction between unlubricated metals in vacuum are much higher than they are in air, as they cold weld and gall. The tendency to gall can be reduced by using dissimilar metals for bearing surfaces [98]. A titanium screw was chosen, as it is much harder than either aluminum, copper, or gold, and it meets the other requirements of the system, such as being non-magnetic and ultra-high vacuum compatible. No evidence of galling has yet appeared on the bearing surfaces.

Our vacuum screwdriver has a maximum torque of 0.5 Nm. Setting $\mu_t \doteq 0.41$, $\mu_c \doteq 0.41$ and taking the dimensions of a 10-24 thread [113] gives a force of 299 N. This is applied to a 2:1 lever, giving a clamping force on the bullet of 598 N.[9]

An analogous equation for the clamping force from a spring-actuated clamping mechanism isn't readily derivable because of the variety of spring-actuated clamping mechanisms used. Mechanisms that involve the transfer arm or vac-

[9]This result is not precise, as there is uncertainty in the coefficients of friction. The coefficients of friction used are for clean, unlubricated samples in air at room temperature [114]. The value of 0.41 for μ_t is for the correct metals: Ti-6Al-4V and 6061-T6 aluminum alloy. Friction data were not available for any titanium alloy on either copper or gold, however. The only data for any refractory metal on either copper of gold were for tungsten on copper, which had a coefficient of 0.41.

uum screwdriver directly applying axial force to compress the spring are limited to the maximal axial force of their device. For our vacuum screwdriver this is 30 N. Mechanisms that involve sliding a sprung clip over a surface of the sample holder or sliding the sample holder under a sprung clip must be designed such that the force applied by the vacuum screwdriver or transfer arm is greater than the product of the clamping force and the sum of the coefficients of friction of all sliding surfaces. This effectively limits the clamping force to at most a factor of two (one sliding surface with a coefficient of friction of 0.5) greater than the force applied by the transfer arm or vacuum screwdriver. A mechanism that involves turning a sample holder with a bayonet-style locking mechanism is effectively a combination of the transfer arm or vacuum screwdriver's directly compressing a spring and its turning a large, high-pitch screw. The most quantitative measure of the difference in clamping force between the UBC system and standard designs is shown by the temperature difference between the sample and the cold head, which for the UBC system is 1 K.

Since a bullet is forcibly driven into the flip stage, we took steps in the design of the flip stage to ensure that the bullet would not become irretrievably stuck (see Figure 4.18). The titanium alloy hook that engages the groove in the bullet pushes the bullet into the flip stage as the screw is tightened. When the screw is loosened and backed off, a circlip on the screw bears against the aluminum clamping block, drawing it back, which in turn causes the titanium hook to bear against the back flange of the bullet, dislodging it from the flip stage.

4.5 Transfer system

In order to introduce a sample for study into the ARPES setup without venting the chamber, there must be a transfer system consisting of a load lock and a mechanism for moving the sample holder (i.e. the bullet) within the chamber. The in-house ARPES system at UBC presents a further challenge, since we must also be able to transfer samples from the MBE to the cryostat. The MBE-grown samples must be grabbed from behind, since a transfer mechanism that attempts to grab the sample holder from the front would outgas and contaminate the samples.

This section describes the mechanism for moving a sample into and between the various chambers of the in-house ARPES system. For a full description of the bullets used to hold samples and the procedure for clamping one into the

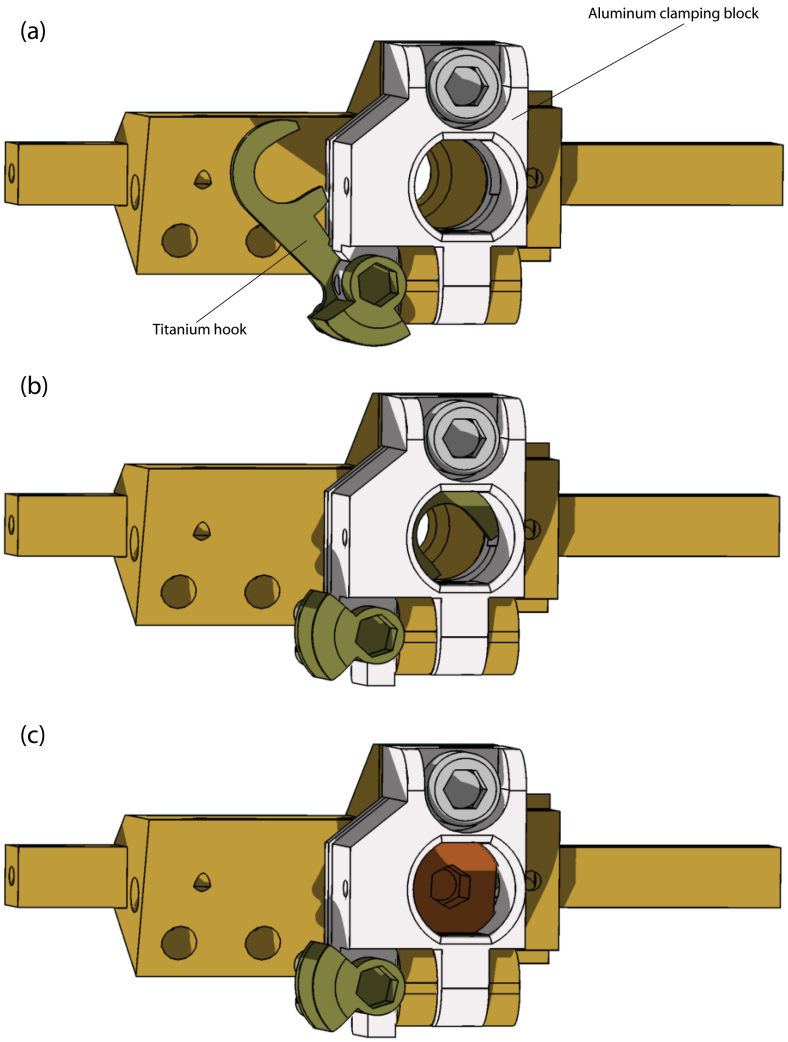

Figure 4.18: (a) With the titanium hook retracted, the bullet can be inserted into the flip stage through the clamping block. (b) With the hook inserted, the bullet is held captive in the aluminum block by the groove at the back of the bullet. When the screw is tightened, the bullet is driven into the flip stage, and when the screw is loosened, a circlip on the screw pulls the block and bullet out, dislodging the bullet. (c) The bullet locked into the flip stage. When the screw is loose, the bullet may be rotated via the hex socket, allowing for alignment by LEED.

cryostat, refer to §4.4.7.

4.5.1 Transfer arm

The main transfer arm accepts samples from either the main chamber load locks or the MBE and moves them to the cryostat. In particular, the main transfer arm must be able grab the bullet actively and securely, translate it, rotate it, and actively release it. A second, similar transfer arm is also used in the MBE chamber.

I developed the grabbing tool, which grabs the bullet from the inside, and designed it to interface with a standard double-magnet active grabbing mechanism (model BHRSS) from Transfer Engineering. Transfer Engineering has integrated our grabbing tool design and fabricated a custom grabbing mechanism for use in our ARPES system.

The grabbing tool is essentially a modified small-hole gage (see Figure 4.19). A traditional small-hole gage consists of a split hollow sphere, the halves of which can be expanded by means of a knurled knob, which turns a screw thread that forces a spreader between the sphere halves [115]. Our grabbing tool has the same split-sphere concept, but the spreader is coupled to the secondary magnet of the grabbing mechanism rather than a knob and screw thread. The sphere end of the grabbing tool fits into the hole at the back of the bullet, and the secondary magnet is used to spread the spheres, securing the bullet onto the transfer arm. The entire transfer arm can then be positioned using the grabbing mechanism's main magnet. Not only does the grabbing tool allow us to manipulate the sample holders in vacuum, but the same concept may be used to manipulate samples on bullets outside of vacuum cleanly and reliably, rather than risking sample contamination or damage by using tweezers.

The double-magnet design of the BHRSS features internal acme threads on the secondary magnet that mate with corresponding external threads on the main magnet. Rotating the secondary magnet with respect to the main magnet actuates the sample-grabbing mechanism. Handling only the main magnet causes the magnets to move together as a unit; the sample grabber stays engaged or disengaged as the grabber is moved and rotated. A single revolution of the secondary magnet relative to the main magnet will lock the grabbing tool.

In order to allow the bullet to be rotated, the end of the transfer arm was designed with a hex key, co-axial with the grabbing tool. The hex key positively couples to the hex hole in the copper bullet and allows the sample to be rotated.

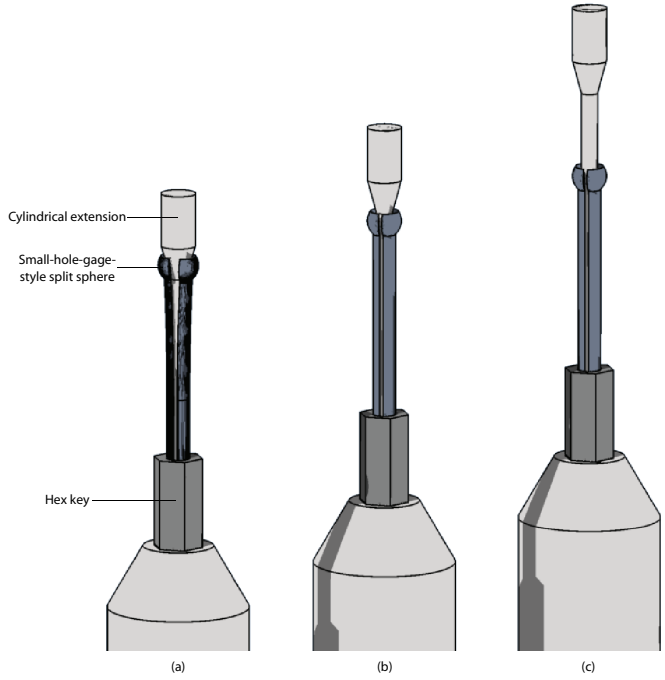

Figure 4.19: (a) The sample-grabbing mechanism at the end of the transfer arm. The small-hole-gage-style split sphere is shown expanded, in the position used to grip the sample. (b) The actuator is farther out, allowing the split sphere to close, taking clamping force off the sample. (c) The actuator can be brought much farther out to actively eject the sample if the need arises.

To allow the bullet to be actively released from the grabbing tool, the spreader in the grabbing tool was designed with a cylindrical extension to its flared edge. When the spreader is pushed towards the bullet rather than pulled back, again using the secondary magnet, the cylindrical extension pushes the bullet off the transfer arm.

4.5.2 Load locks: sample transfer from outside the chamber

The UBC ARPES system has two load locks—one to introduce an external sample on a bullet into the main ARPES chamber and one to introduce a bullet with substrate into the MBE chamber. Each load lock has a door that can be opened and through which a bullet may be inserted, a gate valve to separate the load lock from the chamber when it's vented, a turbo pump, and an ion gauge (see Figure 4.20).

In the load lock, a "garage" sits on a single-magnet transporter from Transfer Engineering. The garage consists of three sheets of stainless steel; the bottom sheet has a small hole that accommodates the tip of the bullet, the middle sheet has a hole that accommodates the bullet up to the flats, and the top sheet has a hole with flats (see Figure 4.21). A bullet can be introduced, nose-down, into the garage and then rotated such that the flats of the bullet and those of the garage no longer align, thus locking the bullet into place. The entire garage can then be pushed through the gate valve, then rotated, by means of the single-magnet transporter, which puts the bullet into a position to be received by the transfer arm in the chamber. The garage has six sets of the bullet-holding holes such that several samples can be loaded into the system at once.

4.5.3 Sample transfer from the MBE chamber

Since the MBE's transfer arm is perpendicular to the ARPES chamber, a sample on a bullet from the MBE chamber must be rotated 90° before it can be studied in the ARPES chamber. This task is accomplished in the transfer chamber, which sits between the MBE and ARPES chambers and includes a cart to carry the sample (see Figure 4.22). The wheeled cart (see Figure 4.23) has a magnetic following material on each end and extends in the MBE chamber to collect the sample, then delivers it to the ARPES chamber. The cart features a central block on which the bullet sits. The transfer chamber has a magnetically actuated

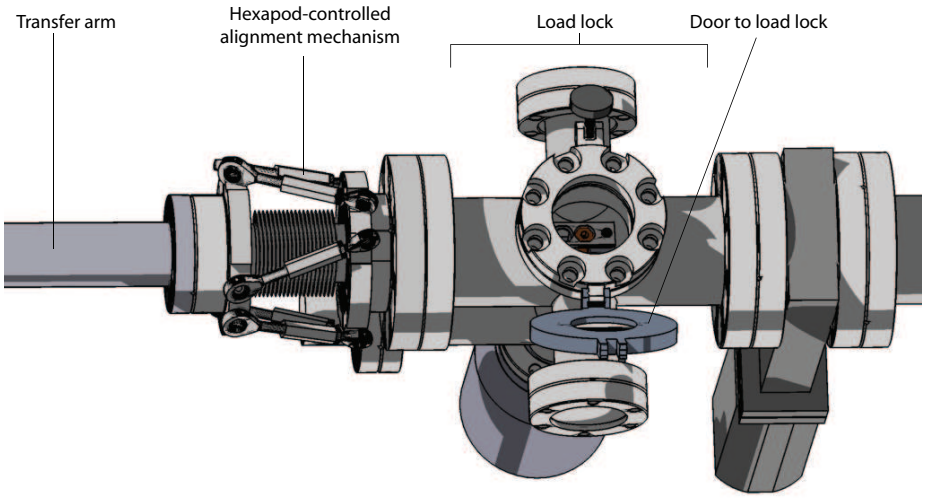

Figure 4.20: The load lock provides a means of keeping up to six samples in vacuum and ready to enter the cryostat. The hexapod or Stewart platform alignment mechanism allows in theory for six-axis adjustment of the transfer arm position, allowing the transfer arm and garage to meet on the same plane. In practice the bellows do not allow rotation about the axis of the transporter. This is inconsequential, as the "garage" (see text) rotates about this axis inside the transporter. This is a non-standard application of the hexapod design. In most instances the the legs move synchronously and are computer controlled [116]. Commercially available port aligners are not rated to support the torque from the weight of the transfer arm magnet. The hexapod design easily handles the mechanical load while simultaneously providing more degrees of freedom and far more precise adjustment in a compact size. The only drawback to this design is that adjusting any one leg affects all axes, so adjustment is iterative.

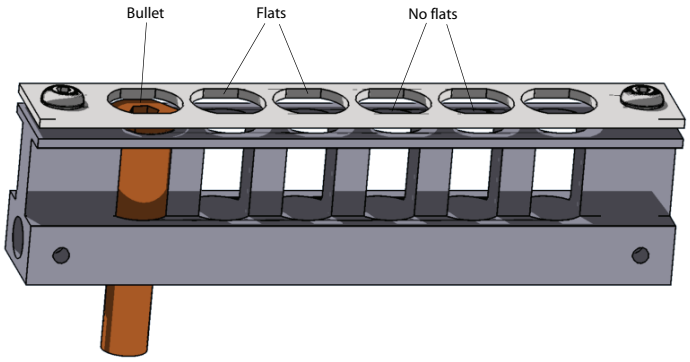

Figure 4.21: The load lock sample garage. A top plate on the garage with flats matching those of the bullet allows the bullet to be turned and locked in place to prevent sample dropping. The holes in the body of the garage are smaller and do not have flats; the back flange of the bullet rests on the face of the garage body.

sample-rotating mechanism that extends from the bottom of the chamber, which can push up the central block from the cart and rotate it by 90° before lowering it back onto the cart. The central block is appropriately keyed so that the rotation is guaranteed to be square. One can therefore use a magnet outside the transfer chamber to pull the cart into the MBE chamber, transfer the bullet onto the central block, pull the cart into the transfer chamber, use the sample-rotation mechanism to rotate the bullet 90°, then, again using a magnet, pull the cart into the ARPES chamber.

4.5.4 Bringing the sample into the cryostat from the transfer arm

At the back of the cryostat are two doors in the cold shield that open to the back of the flip stage and are thermally connected to the cold shield by copper braids. Above the doors, and attached to the cold shield, are sheet-metal beryllium-copper springs—a set of two lock the doors in their closed position, and another set locks the doors in the open position. Where the two doors meet are two holes (each formed by semi-circles cut out of each door) such that one can pull the doors free from the springs—in either open or closed position—by using the groove between the ball and the shaft of the ball-end vacuum screwdriver to catch the edge of the semi-circular hole. Once dislodged from the springs, the doors are pushed with the vacuum screwdriver to their desired position. The lower hole allows the vacuum screwdriver access to the bullet installed in the flip stage, such that it can be rotated, while the upper hole allows the vacuum screwdriver access to the clamping screw, to loosen and tighten the bullet into place, all without having to open the doors in the cold shield.

Thus, once a bullet is on the system's main transfer arm, ready to be introduced into the ARPES chamber for study, the procedure to install it into the cryostat is as follows: the cryostat must be rotated so that the back faces the vacuum screwdriver, at which point one can use the screwdriver to open the doors in the cold shield and secure them in the open position with the springs. Next, the cryostat must be rotated such that the back faces the bullet, after which the transfer arm can be used first to move the bullet through the bullet clamp and into the flip stage and then to rotate the bullet so that the flats secure the bullet in place. At this point the transfer arm may be extracted and the cryostat rotated so that the back once again faces the vacuum screwdriver, which should be used to rotate the titanium clip into place, rotate the bullet

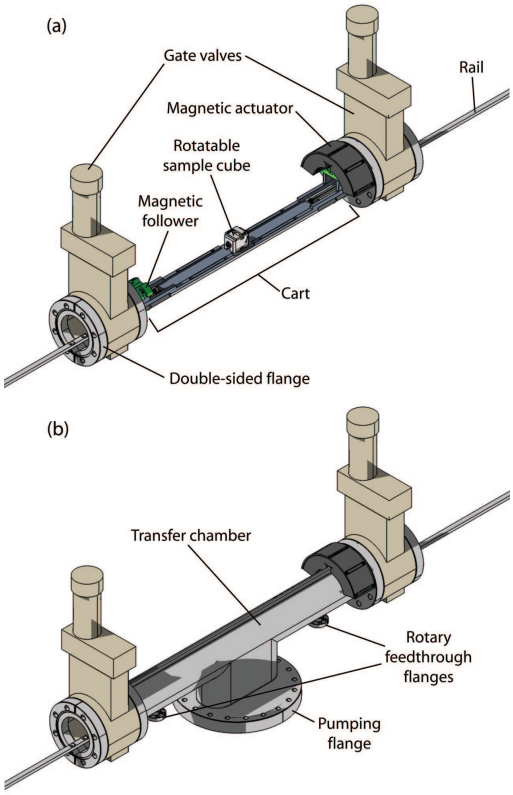

Figure 4.22: MBE to ARPES transfer chamber. In (a) the walls of the chamber are not shown. The cart extends over almost the length of the chamber and has magnetic followers at both ends. At the centre is a block that holds the bullet. An extended rail mounted to the double-sided flanges at each end of the chamber allows the cart to be moved to extend well out of the transfer chamber, such that the central block can enter both the MBE and the ARPES chambers. When the cart is entirely in the chamber, as shown, the magnetic actuator can be lifted off one magnetic follower and placed on the other. This two-follower system gives the cart a travel almost twice the length of the transfer chamber. (b) shows the system with the walls of the transfer chamber shown. The large central flange is a pumping port, and the smaller flanges allow the attachment of a linear-rotary feedthrough. The feedthrough is used to rotate the central block 90°, a feature that is needed because the MBE transfer arm is perpendicular to the ARPES transfer arm.

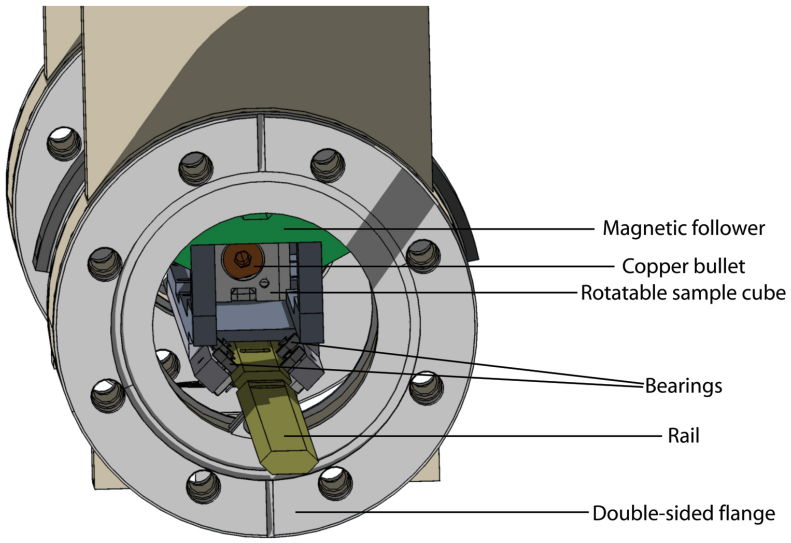

Figure 4.23: A view down the flange, showing how the cart bearings hold the cart captive on the rail.

to the angle needed to perform measurements (determined using either a predefined alignment mark or a LEED measurement to ascertain the direction of the crystal axes), tighten the clamping screw, and close the doors.

Reversing the procedure will extract the bullet, with the circlip mechanism (see §4.4.7) ensuring that the bullet is actively dislodged from the flip stage.

4.6 Conclusion

The UBC ARPES system is a unique and powerful tool. Combining an MBE with an ARPES system allows a much wider range of materials to be studied, compared with a conventional ARPES system. In order to achieve the required mechanical and thermal precision, several novel design features have been introduced, including a systematic optimization of the thermal contact conductivity of all parts of the thermal linkage between the cold head and the sample and the use of Si_3N_4 ball-bearings as both a non-magnetic, UHV-compatible pivot point capable of operating at low temperatures and as a thermal break. The sample transfer system is also a major success. Samples can be readily introduced to

the cryostat from either the MBE or the load lock and can be aligned in situ with unprecedented reliability—to date, no samples have been dropped. With excellent analyzer resolution, the ability to rotate polarization, and a mechanically and thermally accurate cryostat with a broad temperature range extending to 2 K, the new ARPES system, which allows MBE-grown samples to be studied, could produce important results for correlated systems in general, including HTSCs.

Chapter 5

Canadian Light Source ARPES Recommendations

The Canadian Light Source (CLS) is a new synchrotron in Saskatoon, Saskatchewan, at which the UBC Quantum Materials group is building the Quantum Materials Spectroscopy Centre (QMSC) to study correlated systems. Undulators at the high-flux beamline have polarization control, and the beamline has a high-resolution monochromator. The QMSC aims to synthesize and characterize correlated systems, model them, and study them using ARPES.

For material growth, the QMSC will feature MBE systems to grow oxides and organic materials, as well as LEED, resonant high-energy electron diffraction (RHEED), STM, atomic force microscopy (AFM), and XPS for characterization. The endstations will feature two high-resolution ARPES systems—one for conventional ARPES experiments and one for spin-resolved ARPES studies, which uses a spin polarimeter rather than an MCP and phosphor screen and thus detects electron spin but at the expense of resolution and count rate.

The major advantages of a synchrotron compared with an in-house photon source is that the former offers higher flux over a continuous range of photon energies, gives control over polarization, and has a smaller spot size. The higher flux, energy range, and polarization control are profitably used in synchrotron ARPES systems, while the smaller spot size is underused. The QMSC beamline at the CLS will have a spot size of $100\,\mu$m, while our lab-based system, the SPECS TMM 304, has a spot size of 500μm. The smaller spot size has the potential to allow us to study smaller samples and especially samples that cleave poorly, such that only a small portion of the sample gives a clean signal. This is not typically exploited in a modern ARPES experiment, as the motion of the sample is not nearly precise enough to keep the beam on the same portion of the sample as the sample is manipulated.

In this chapter, we consider the UBC ARPES system as a prototype for

the ARPES setups at the QMSC and discuss refinements to the former's design such that the cryostat axes can be aligned sufficiently well given the constraints imposed by the smaller spot size at the CLS. We also investigate the possibility of using a fixed cryostat with a moving analyzer—with this design, once the sample is aligned into the beam, it will stay aligned when the analyzer is moved. The physical requirements of this motion are much less stringent than those for the moving cryostat, as the motion of the analyzer only has to be accurate within the dimensions of the focus of the analyzer (2 mm spot), whereas the beam size from a synchrotron is typically much smaller.

Finally, we also discuss in this chapter an alternative to the standard straight and curved slits used in modern ARPES electron analyzers—one that yields data on an orthogonal coordinate system and that eliminates the astigmatism problems introduced by the traditional slits.

5.1 Automated angular scans: moving cryostat and fixed analyzer

The standard ARPES manipulator design has an xyz-stage to position the sample spatially and a rotation stage on the manipulator to set the θ angle. The other angles must be set through motion within the cryostat. The relative orientation of the xyz- and θ-stages on the cryostat makes significant practical differences to how the manipulator is operated, especially during an automated scan. During an automated scan, angles have to be moved without the sample moving out of the beam or analyzer focus. To accomplish this, not only must the sample be positioned at the analyzer focus, but the centre of rotation of all angular degrees of freedom must coincide with where the beam spot hits the sample; otherwise the sample will precess out of the beam upon rotation.

With an ARPES system built with a θ-stage under the xy elements, such that the xy elements rotate when the θ-stage turns, the xy elements can be used to position the sample at the centre of rotation. This would allow an automated scan of the sample to be performed so long as the centre of rotation happened to be in the analyzer focus. For this to be the case, the analyzer position needs to be adjustable or the welding tolerances of the chamber and the tolerances of the analyzer itself need to be sufficiently tight to ensure that the centre of rotation is in the analyzer focus. If these requirements are not met, then the only option is to use the xy-stage to move the sample to the analyzer focus,

away from the centre of θ rotation. As the sample would then precess with θ rotation, the sample position would have to be re-optimized with every scan, making automated scans impossible without automated correction of x and y as well.

With an ARPES system built with a θ-stage above the xy elements, such that the xy elements do not rotate when the θ-stage turns, the xy-stage can be used to move the centre of rotation of the cryostat into the analyzer focus. In order for this geometry to work, the mechanical tolerances of the manipulator and cryostat have to be less than the beam spot size. While this is difficult to obtain given the number of brazes and welds in the cryostat, if the sample position of the cryostat were adjustable such that it could be brought to the axis of rotation of the θ-stage once the manipulator was assembled, then it would be possible to run automated scans that would keep the beam on the sample without adjusting x or y. This was the goal of the in-house ARPES system at UBC, and the first attempt failed for several reasons.

The angular errors in the manipulator and cryostat were sufficiently large that they were outside of the adjustment range of the cryostat. This problem was corrected with an angled shim placed between the cold shield and the cryostat body, but small misalignments persisted. The adjustment of the cryostat had to be accurate within the lamp spot size—500 μm. Although the mechanical adjustment systems were capable of achieving such precision, the experimental setup did not allow for immediate feedback on the adjustments.

In order to make the adjustment, the axis of rotation of the cryostat had to be determined at operating temperatures—although the cryostat was designed not to distort as it cooled, assuming that this robustness would hold to within the beam spot size is unrealistic. The system also had to be under vacuum, as the distortion caused by vacuum forces is relatively large compared with the beam spot size. Thus, the procedure to make an adjustment to the sample position consisted of cooling the cryostat, setting up a camera on a small tripod looking up through a viewport on the bottom of the system, and taking photos of the system as a function of angle. The photographs were then analyzed to determine the centre of rotation. The distance the sample had to move to be in the centre of rotation was then measured. The system was then vented, the cryostat was removed and partially disassembled to facilitate adjustment, and finally it was reassembled.

This time-consuming method was eventually abandoned, since the cryostat would move with respect to the angle of rotation each time a new copper gasket

was used in the reassembly and installation process.

The experiences from the UBC ARPES system demonstrate that a system with no external xy adjustment between the cryostat and the rotation stage—and no continuous correction of x and y—does not lend itself to automated measurements with small samples and a small spot.

Given the unsuitability of a system with one xy adjustment, either above or below the rotation stage, for automated scans, it appears that the optimal method for allowing a cryostat to automatically rotate the sample in the analyzer focus is to have two separate xy adjustments, one below the rotation stage and one above it. The xy-stage below the rotation stage would allow the axis of rotation to be brought to the analyzer focus while the one above the rotation stage would allow the sample to be positioned on the axis of rotation. Further, this would allow samples where the good spot was off-centre to be handled easily; a small adjustment of the upper xy-stage would suffice to make the system ready to measure, rotating about the sample itself.

On future systems, such as the one being developed at the CLS, should it use the cryostat to accomplish sample manipulation, the technically simplest means of acquiring the needed degrees of freedom would be to simply sandwich the rotation stage between two xy-stages and increase the length of the cryostat body accordingly.

5.2 Automated angular scans: fixed cryostat and moving analyzer

The first ARPES systems used a small electron analyzer mounted on a goniometer in the vacuum chamber, and the goniometer was moved through rotary feedthroughs [117]. Analyzer resolution is limited by the size of the analyzer itself. Equation 4.3 shows that the relationship between the physical separation of the detected electrons for a given difference in energy scales as the dimensions of the analyzer hemispheres. Although the analyzer slit width and the MCP–CCD detector system both contribute to the spatial resolution of the apparatus, the energy scale at the detector depends on the size of the hemispheres, and thus, for a given slit width and detector system, a larger analyzer will ultimately give a higher resolution. Modern analyzer resolution, and hence size, has increased, and the difficulty of moving large objects in vacuum ushered in a change in experimental design—current systems feature a fixed analyzer bolted to a flange

of the chamber and cryostat capable of manipulating the sample angle. In such a system, however, the sample moves relative to the photon beam. If the sample is smaller than the beam, the cross-section of the beam incident on the sample changes as the sample is rotated, complicating quantitative analysis. If the beam is smaller than the sample, further experimental complications arise: as the sample rotates, the portion of the sample that is illuminated changes. On a uniform sample smaller than the beam, the flux on the sample will change, which is not a major concern. On a difficult to cleave sample, however, the ratio of synchrotron light hitting good parts of the sample to light hitting badly cleaved portions would in general change, thereby introducing spurious changes in the relative intensity between electronic features of the good cleave to those from poorly cleaved areas. These problems will only be exacerbated as the ARPES community moves to measuring material systems that do not cleave uniformly.

In contrast, and technical challenges aside, the moving-analyzer design allows for a more robust experimental method and yields more consistent data on difficult samples, since the illumination of the sample does not change at all as the analyzer angles are changed.

In today's ARPES experiments, the demands on the cryostat and manipulator system are extremely high: the sample temperature should be accurately tunable over a broad range, ideally down to a few Kelvin; the sample must have three accurately controllable spatial degrees of freedom and at least two angular degrees of freedom; the angular axes must intersect to within a small fraction of the spot and sample size; and the cryostat must be UHV compatible and it must not introduce any stray electric or magnetic fields. While it is relatively easy to build a fixed, non-magnetic UHV cryostat with the required range of temperatures—commercial options are available [118]—a system that allows for motion of the sample within the cryostat is far more complicated to produce. All existing systems sacrifice some aspect of performance—allowing a higher minimum temperature in exchange for more angular freedom, for instance.

With a moving analyzer, there would be no trade-offs in cryostat design—the cryostat would optimized for the lowest possible temperature, since angular motion within the cryostat would not be a goal of the system. The illumination of the sample would be constant throughout the experiment. The last point to consider, beyond the technical details of the implementation, is the effects that the changes in the geometry would have on the matrix elements. Damascelli et al. [6] discuss the effects of polarization on the photoemission matrix elements. If the incoming photon and the photoelectron are both in a mirror

plane of the initial state, then even and odd initial and final states as well as the photoemission operator $\mathbf{A} \cdot \mathbf{p}$ all can be defined as even or odd with respect to the mirror plane. In this geometry, an even initial state will have its matrix element, and hence photoemission intensity, vanish for s-polarized photons, and an odd initial state will have its intensity vanish for p-polarized photons. For a general arrangement, there is no rule of thumb to determine polarization effects, as there is no coordinate system where even and odd can be defined for both the initial and final states as well as $\mathbf{A} \cdot \mathbf{p}$.

The conditions for having a well-defined parity state are identical for a fixed analyzer with a moving cryostat and a fixed cryostat with moving analyzer. The matrix elements are in general different, however, but neither set of matrix elements has a clear experimental or theoretical advantage. For a fixed analyzer, the detected electrons and the incident photons can only be on a mirror plane of an initial state when the sample is at $\phi = 0$. For $\phi \neq 0$, the photon beam and the detected electrons are in the same plane, but any mirror planes of the sample are misaligned with the plane containing the photon beam and the detected electrons. The polarization of the photons still has a significant effect on the matrix element, but there is no parity argument to determine how orbital symmetries relate to photoemission intensity. The situation is similar but not identical for a moving analyzer. The analyzer's ϕ angle must be set to zero in order to make the incoming photon and the detected photoelectron share a mirror plane of an initial electronic state. When $\phi \neq 0$, the plane defined by the incoming photon and the detected electron is no longer perpendicular to the sample and thus is no longer a mirror plane of any state. The difference between the relative angles involved here and with the moving cryostat is that relative position of the analyzer and photon beam changes with a moving analyzer; in the reference frame of the sample, the analyzer and light source move synchronously for motion accomplished by the cryostat. For analyzer motion, only the analyzer angle changes. In both configurations with a non-zero ϕ, there is no parity argument to determine where matrix elements will be minimal; however, although the matrix elements for each experimental geometry will generally be different, both fully allow for the effects of incident photon polarization to be exploited.

The use of a moving analyzer would allow the sample illumination to stay constant during measurement, allowing for more reliable data and facilitating reliable automated scans. Without the requirements for precise in-vacuum motion, a commercial cryostat could be used, allowing for lower temperatures and more

reliable temperature control. The matrix element situation is slightly different, but the change to a moving analyzer would not likely be detrimental. Early ARPES systems used a moving analyzer, and the change to a fixed-analyzer experimental setup was due to the size of modern analyzers, as opposed to an issue with matrix-element effects.

5.2.1 Edge-welded bellows concept

Using commercially available edge-welded bellows coupled to the analyzer would theoretically allow the analyzer to sweep an angular window of 72° (see Figure 5.1). The challenges involved in implementing such a design are maintaining magnetic shielding and providing reliable, accurate movement. A major limitation to the edge-welded bellows concept is that it is not suited to two-axis motion.

Achieving any compound angle for the analyzer using a two-axis goniometer requires a rotary axis to prevent the bellows from becoming twisted. Software to calculate the torsional motion of the goniometer with respect to the bellows and synchronously control the rotary axis to compensate for that motion would have to be developed. Asynchronous motion, caused either by a motion element failure or by a control system error, would be catastrophic. Thus we investigate the use of a one-axis goniometer in conjunction with a rotatable cryostat. Rotating the cryostat would change the illumination of the sample, but this would have to be done a small number of times during the course of a typical experiment. With the analyzer slit along the $\hat{\theta}$ direction, a goniometer that moves the analyzer on the ϕ-axis would be sufficient to map out an area of angle space 72° by the angular view of the analyzer, which would be 7° or 14° for the modes most often used. This is alone enough to map several complete BZs, all without rotating the cryostat. Even in experiments where the cryostat was rotated, the sample position would only need to be re-optimized between θ rotations, facilitating automatic scans with minimal interruptions. Rotating the cryostat as a whole does not involve any in-vacuum motion and thus is compatible with using a commercially available cryostat.

Magnetic shielding is normally accomplished by a vacuum chamber either fabricated from μ-metal or with internal, press-fit μ-metal shielding. This is coupled to the analyzer's double-layer internal μ-metal shield. The analyzer shielding couples to the vacuum chamber with a μ-metal skirt that extends into the chamber from the analyzer and makes contact with the chamber walls. Such

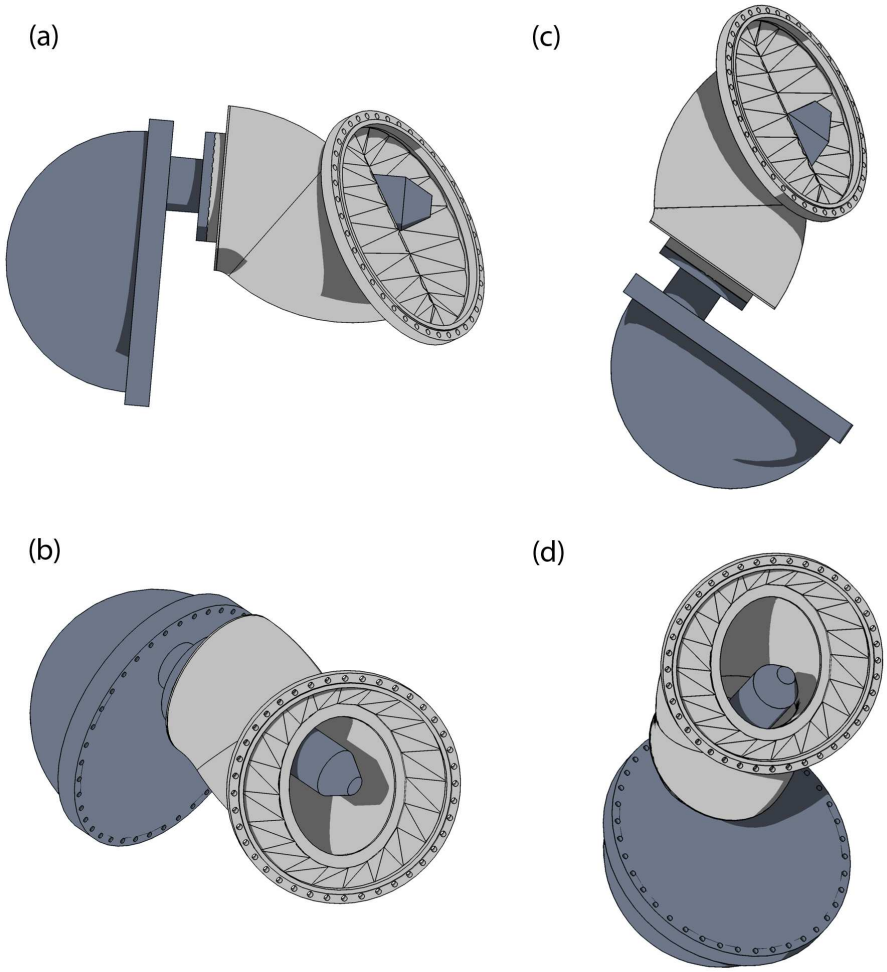

Figure 5.1: The bellows depicted are stock bellows being used with the designed bending radii, with custom flanges attached. The flange on the chamber side is an MDC wire-seal flange, which is mounted at an angle relative to the bellows to allow the beam to reach the cryostat without hitting the flange. (a) The cryostat is in the upper position, 5° above normal. (b) Isometric view of bellows in the upper position. (c) The bellows down as far as possible, at 67° off normal, for a total motion of 72°. (d) Isometric view of the bellows in the down position.

an arrangement is not possible with a moving analyzer. For a moving analyzer to be successful, the magnetic fields experienced by the photoelectron would have to be equal to or less than those encountered in a fixed-analyzer geometry where effectively all of the electron's path is in an area with double μ-metal shielding. Where the double shielding ends, the analyzer shielding is coupled to the chamber, which provides a path for flux to leave the analyzer shielding without being concentrated at the sample.

The fact that, until the electron enters the analyzer, it has only one layer of μ-metal shielding raises the question if a double-layer is really needed. The electron's path length in the analyzer is much larger than the path between the sample and the analyzer's entrance. Further, in high-energy resolution experiments the electron's initial kinetic energy is much greater than the pass energy, making the effects of magnetic fields on the electron's trajectory much more significant in the analyzer than outside. The μ-metal shielding must be continuous to be effective [100]. Without a way to couple the double-layer analyzer shielding to the chamber, a double-layer shielding that encompasses the analyzer range of motion and couples to a double-shielded chamber appears to be the correct approach.

The movement of the analyzer is a relatively simple technical challenge: it has to be able to rotate about the analyzer focus to an accuracy of 0.1°, and run-out of the motion must be much smaller than the 2 mm analyzer focus. Any component of the motion system within the μ-metal shield must be non-magnetic and cannot generate any magnetic signal. By using a worm/worm gear drive with the motor outside the shielding, such a rotation stage can be constructed (see Figure 5.2).

With a design existing that solves the challenges of a moving-analyzer design and the advantages evident, the implementation of a moving analyzer becomes a realistic possibility for the QMSC.

5.3 Analyzer slits

Section 4.2 and, in particular, Figure 4.7 showed that the straight and standard curved slits used in current electron analyzers yield data for a flat cut in angular space and a flat Fermi surface, respectively. However, these slits are sources of astigmatism, owing to fringe effects in the analyzer (see Figure 4.8), and for either curved or straight slits the curves of constant energy and angle on

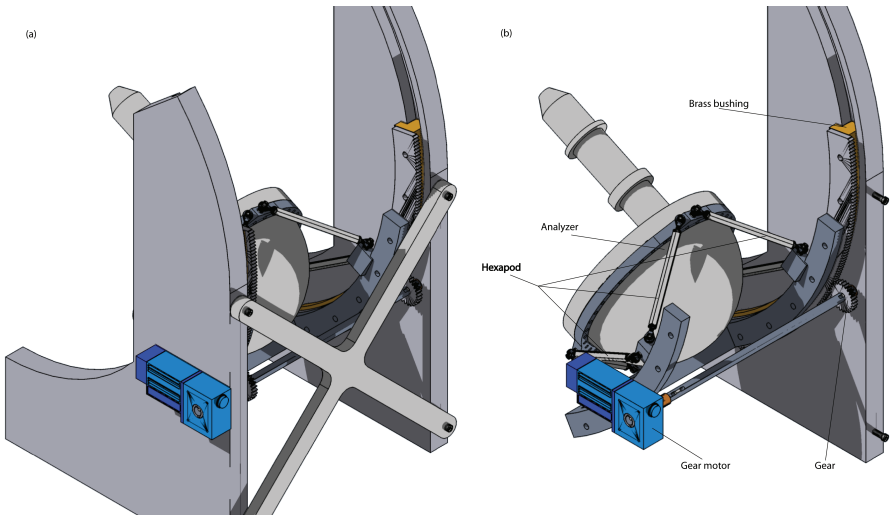

Figure 5.2: (a) The goniometer for analyzer motion. (b) The goniometer with some elements of the left side not shown. The motion is driven by a gear motor, and the motion is guided by brass bushings in grooves in the stainless steel mounting plates. The cryostat is coupled to the goniometer by a manually actuated hexapod or Stewart platform, allowing the focus of the analyzer to be aligned with the centre of rotation of the goniometer [116].

the detector are not orthogonal. As ARPES systems obtain higher resolution, the astigmatism and non-orthogonality of coordinates will become progressively more problematic.

If we use slits with a radius of curvature A (see Figure 4.4), however, the data will appear on a locally orthogonal coordinate system. With the curved slits presently used, the Fermi surface is nominally flat at E_{pass} and close to flat for the detectable range of δE, but the astigmatism introduced presents a major challenge for data analysis. A slit with curvature of radius A, in contrast, introduces a minimum of astigmatism and delivers data that can be put to Cartesian coordinates with a known and mathematically simple transformation.

There is still utility in straight and traditionally curved slits. The use of slits of radius A does not preclude the use of the standard slits, as the analyzer supports many different types of slits. Gains could be made, however, by including slits of radius A as part of the gamut of slits provided with the analyzer.

5.4 Conclusion

The ARPES system constructed at UBC is a powerful research tool in its own right, with its coupling to an MBE system, the ability to rotate polarization, and its setting of a new bar for low temperature with two-axis angular motion. It also serves as a prototype for the QMSC ARPES system being constructed at the CLS. With what we have built at UBC, we are presented with two viable options for reaching very low temperatures with precise multi-axis angular motion: incorporate a second xy-stage on the existing manipulator design to provide a means of obtaining concentric sample motion at an arbitrary position or use a simplified, colder cryostat design together with a moving analyzer. A study of the focusing properties of the hemispheres with different slits points to the use of slits with a radius of curvature equal to that of the distance from the hemisphere centre to the slits. These slits would provide neither a flat Fermi edge nor a flat cut in angle space, but they would provide a minimum in astigmatism and thus, after transformation by computer, would provide the most reliable means of obtaining a flat Fermi edge where gap sizes could be most readily discerned.

Chapter 6

Conclusions

This thesis presented work on two different compounds, Tl2201 and YBCO6.5, as well as the construction of a new ARPES system at UBC and a design study for a to-be-constructed system at the Canadian Light Source. While these works are at first glance disconnected, they can be seen as steps towards understanding cuprate superconductivity through ARPES. Both Tl2201 and YBCO6.5 gave ARPES results on materials that had previously generated important bulk-sensitive results, and both the UBC and CLS ARPES systems will be used to conduct further research on Tl2201 and YBCO6.5, among other compounds, at lower temperatures and at very high resolutions.

The results on Tl2201 and YBCO6.5 substantially advance our understanding of the cuprates. Both systems produced results that were significant when viewed in the context of ARPES measurements, but the results become even more important when viewed in the broader context of experimental results on the cuprates, as they are the first instances where major results have been obtained through both bulk- and surface-sensitive techniques on the same materials.

Tl2201 and YBCO6.5 provide complementary results, as Tl2201 is readily grown from optimally doped to extremely overdoped, while YBCO6.5 is quite underdoped.

Tl2201 and YBCO6.5 are both extremely clean materials, with very low cation disorder and good crystal structure. The long mean free paths in these systems make them appropriate for bulk-sensitive measurements. Both materials have provided significant bulk-sensitive results, while materials easily studied by ARPES have not.

The simple band structure of Tl2201, as well as its good crystallinity and its high T_C as a single-layer compound, makes Tl2201 an ideal candidate to study superconductivity in the overdoped regime without complications from disorder or overlapping bands. The data produced indeed have only one band near the Fermi level and provide a number of clear and important results. The

FS is the first coherent, continuous FS for any cuprate. In addition to the FS, the nodal-antinodal anisotropy reversal was discovered. In the underdoped cuprates, the antinodal features are sufficiently incoherent to break up the FS into disconnected Fermi arcs. It was thought that as doping increased and the system behaved more as a normal metal that the anisotropy would disappear. The Tl2201 results have the unexpected features that the antinodal QPs are much sharper than the nodal ones and that as overdoping increases, the reverse anisotropy increases.

The Tl2201 FS also marks the first agreement between bulk- and surface-sensitive techniques on the FS of any cuprate. The agreement on the FS between our ARPES results and the AMRO results of Hussey et al. provide a strong indication that the Tl2201 FS is a robust result, independent of measurement technique.

Since Tl2201 is an overdoped cuprate and can be overdoped to the point where it is non-superconducting, the Tl2201 data provide another path to understanding the physics of high-T_C superconductivity. On the underdoped side of the phase diagram, superconductivity emerges from an antiferromagnetic insulator as doping is increased. Approaching superconductivity from the overdoped side of the phase diagram allows the system to be treated as a modification to a relatively normal metal. It is very likely that insight gained from approaching superconductivity from both sides of the phase diagram will be needed in order to develop a theoretical model of cuprate superconductivity.

In parallel with the Tl2201 work, we investigated the underdoped side of the phase diagram by measuring YBCO6.5

The doping of YBCO takes place through oxygenation of the copper-oxygen chains, which are maximally far from the copper-oxygen planes that generate the superconducting bands. At some doping levels, including YBCO6.5, it is possible to make the oxygen sites ordered, giving excellent crystallinity and a very sharp superconducting transition temperature. Bulk-sensitive measurements, which require a long mean free path, have been successful on YBCO but have had little success on other underdoped cuprates. YBCO has a different crystal structure than the rest of the cuprates. There is no natural cleavage plane, and the cleaved surfaces are polar. The polar surfaces self-dope to levels much different from the bulk, presenting a significant challenge for any surface-sensitive technique.

By evaporating potassium onto the cleaved surface of a YBCO6.5 sample, the doping level of the surface was brought in line with that of the bulk material,

and a FS was obtained. The as-cleaved YBCO6.5 surface was overdoped beyond the superconducting dome. Evaporating potassium onto the surface allowed the doping level to be continuously lowered, and the evolution of the FS from a continuous surface reminiscent of that of Tl2201 to disconnected Fermi arcs similar to other underdoped cuprates was observed.

The significance of the YBCO work is two-fold. The results themselves are the first ARPES results with the surface doping matching that of the bulk on YBCO. YBCO is an important chemical system because of its clean structure and the bulk-sensitive measurements done on it. The introduction of alkali metal doping to the cuprates opens the possibility of changing the doping of any cleaved surface. The ability to measure the change of spectral features on the same cleave of the same sample as the doping level is changed has the potential to both access doping levels that cannot be obtained in the bulk and provide unambiguous trends as a function of doping on difficult-to-cleave materials.

Together the Tl2201 and YBCO6.5 results significantly advance our understanding of the evolution of spectral features of the FS of cuprates. As both materials are very well ordered and are not complicated by structural modulations or cation disorder, it can be argued that the evolution of the FS as a function of doping seen in these two systems offers a good picture of the generic cuprate FS and QP evolution as a function of doping. Furthermore, both systems have provided bulk-sensitive results, while the bulk-sensitive measurement of other families of cuprates has been less successful. In the case of Tl2201, there is a qualitative agreement between the ARPES and AMRO FSs. In YBCO6.5, it is an open question as to how the disconnected Fermi arcs seen by ARPES reconcile with the detection of electron pockets by Doiron-Leyraud et al. [13]. Having results from complementary techniques on the same system does provide a chance to directly compare the results from each technique, as differences in the results of several techniques can be definitively interpreted as originating from the techniques themselves and not from the material system.

Concurrent with the synchrotron measurements of Tl2201 and YBCO6.5, a new lab-based ARPES system at UBC was constructed. The new system advances the state of the art in a number of areas. The UBC ARPES system incorporates a rotating, polarizing monochromator, which for the first time gives polarization control in a lab-based ARPES system. A new sample transfer mechanism has been developed, which allows samples grown in an attached MBE to be introduced into the ARPES cryostat without the sample surface ever being exposed to the off-gasing that inevitably comes from moving transfer arm

components. The most significant advances, though, are in the cryostat itself. The cryostat can bring the sample temperature to a benchmark low of 2.7 K while maintaining an unprecedented degree of mechanical accuracy. By analyzing where thermal breaks occur, experimentally, through a review of thermal contact literature, and by calculations, we minimized all thermal breaks such that the conductivity of high-purity copper and the temperature of the pumped liquid helium set the limits of the sample temperature. The cryostat motion uses no bushings, no gearing, and no in-vacuum motion. The sample movement is controlled by an out-of-vacuum CNC indexer. The components responsible for motion are thermally linked and use the same materials as the body of the cryostat to ensure that the thermal contraction of motion components is matched to the cryostat body, preventing any offsets from differential thermal contraction.

The advances made by the UBC chamber were developed with the larger goal of building a system where temperature, vacuum, motion, electromagnetic shielding, and elimination of electromagnetic interference were all put on equal footing. Each potential optimization of one component of the system was analyzed for potentially negative effects on other aspects of the system. As a result of this balanced design approach, the system makes a number of major advances while maintaining excellent vacuum and shielding.

In addition to the design and commissioning of the UBC ARPES chamber, a design study was done for the development of a new ARPES system at the Canadian Light Source. With a much smaller spot size than lab-based light sources, the CLS ARPES system has the potential to be able to study both samples that are very small and samples that do not cleave well and only produce useful photoemission spectra over a small part of the cleaved surface. When the good portion of a cleave has to be searched for, automated scans are not reliable, as the good portion of the sample can precess out of the beam. A new system design, which moves the analyzer rather than the cryostat, is presented. With the cryostat fixed, the beam always remains on the same portion of the sample, allowing automated scans and eliminating the possibility of obtaining misleading results from different spot positions on the sample as the angle is changed.

The work presented makes significant advances in the push to characterize cuprate superconductivity through ARPES—through experimental results, but also through advancements in techniques and experimental systems. The work on Tl2201 and YBCO6.5 greatly improves our understanding of the evolution of cuprate Fermi surfaces and quasiparticle lineshapes as a function of doping. The door is opened for more ARPES research on these systems, which hold great

potential to improve our understanding of the cuprates both because they are free of many of the complications of other systems and because they have been successfully measured by bulk-sensitive techniques, allowing for direct comparison between ARPES and bulk-sensitive results. The YBCO6.5 measurements were made possible by the introduction of alkali-metal deposition to solve the polar surface problem. This technique can be used both to deal with polar surfaces and to progressively change the doping samples, even those that do not have a polar surface problem. The UBC ARPES chamber is a significant advance in the state of the art, with large improvements in temperature and motion control. The chamber itself is a valuable experimental tool, but the design advances are of value to any group constructing a new ARPES system. The design study presented for the CLS is a practical path forward, incorporating significant further refinements in measurement reliability and temperature control.

Bibliography

[1] I. Falconer. *Olivia Saves the Circus*. Simon and Schuster, New York, 2001.

[2] W. Holzwarth and W. Erlbruch. *The Story of the Little Mole Who Knew It Was None of His Business*. David Bennet Books, London, 1994.

[3] J.G. Bednorz and K.A. Muller. Possible high T_C superconductivity in the Ba-La-Cu-O system. *Z. Phys. B: Condensed Matter*, 64:189, 1986.

[4] N.W. Ashcroft and N.D. Mermin. *Solid State Physics*. Brooks/Cole, Pacific Grove, California, 1976.

[5] H. Ibach and H. Lueth. *Solid-State Physics*. Springer, Berlin, 1995.

[6] A. Damascelli, Z. Hussain, and Z.-X. Shen. Angle-resolved photoemission studies of the cuprate superconductors. *Reviews of Modern Physics*, 75:473–541, 2003.

[7] J. Orenstein and A.J. Millis. Advances in the physics of high-temperature superconductivity. *Science*, 288:468–474, 2000.

[8] S. Hüfner. *Photoelectron Spectroscopy*. Springer, Berlin, 1995.

[9] A. Damascelli. Probing the electronic structure of complex systems by ARPES. *Physica Scripta*, 109:61–74, 2004.

[10] H. He, P. Bourges, Y. Sidis, C. Ulrich, L.P. Regnault, S. Pailhes, N.S. Berzigiarova, N.N. Kolesnikov, and B. Keimer. Magnetic resonant mode in the single-layer high-temperature superconductor $Tl_2Ba_2CuO_{6+\delta}$. *Science*, 295:1045–1047, 2002.

[11] N.E. Hussey, M. Abdel-Jawad, A. Carrington, A.P. Mackenzie, and L. Ballcas. A coherent three-dimensional Fermi surface in a high-transition-temperature superconductor. *Nature*, 425:814–817, 2003.

[12] R. Liang, D.A. Bonn, and W.N. Hardy. Preparation and x-ray characterization of highly ordered ortho-II phase $YBa_2Cu_3O_{6.50}$ single crystals. *Physica C*, 336:57–62, 2000.

[13] N. Doiron-Leyraud et al. Quantum oscillations and the Fermi surface in an underdoped high-T_C superconductor. *Nature*, 447:565–568, 2007.

[14] D. LeBoeuf et al. Electron pockets in the Fermi surface of hole-doped high-T_C superconductors. *Nature*, 450:533–536, 2007.

[15] C. Jaudet et al. De Haas-van Alphen oscillations in the underdoped cuprate $YBa_2Cu_3O_{6.5}$. *Physical Review Letters*, 100:187005, 2008.

[16] N. Nakagawa et al. Why some interfaces cannot be sharp. *Nature Materials*, 5:204–209, 2006.

[17] W. Chen, D. Qi, X. Gao, and A.T.H. Wee. Surface transfer doping of semiconductors. *Progress in Surface Science*, 84:279–321, 2009.

[18] M.P. Seah and W.A Dench. Quantitative electron spectroscopy of surfaces: A standard data base for electron inelastic mean free paths in solids. *Surface and Interface Analysis*, 1:2–11, 1979.

[19] D.G. Hawthorn, S.Y. Li, M. Sutherland, Etienne Boaknin, R.W. Hill, C. Proust, F. Ronning, M.A. Tanatar, Johnpierre Paglione, Louis Taillefer, D. Peets, Ruixing Liang, D.A. Bonn, W.N. Hardy, and N.N. Kolesnikov. Doping dependence of the superconducting gap in $Tl_2Ba_2CuO_{6+\delta}$ from heat transport. *Physical Review B*, 75:104518, 2007.

[20] H. Eisaki, N. Kaneko, D.L. Feng, A. Damascelli, P.K. Mang, K.M. Shen, Z.-X. Shen, and M. Geven. Effect of chemical inhomogeneity in bismuth-based copper oxide superconductors. *Physical Review B*, 69:064512, 2004.

[21] A. Mans, I. Santoso, Y. Huang, W.K. Siu, S. Tavaddod, V. Arpiainen, M. Lindroos, H. Berger, V.N. Strocov, M. Shi, L. Patthey, and M.S. Golden. Experimental proof of a structural origin for the shadow Fermi surface of $Bi_2Sr_2CaCu_2O_{8+\delta}$. *Physical Review Letters*, 96:107007, 2006.

[22] C. Proust, E. Boaknin, R.W. Hill, L. Taillefer, and A.P. Mackenzie. Heat transport in a strongly overdoped cuprate: Fermi liquid and a pure *d*-wave BCS superconductor. *Physical Review Letters*, 89:147003, 2002.

[23] Y. Shimakawa, Y. Kubo, T. Manako, and H. Igarashi. Neutron-diffraction study of $Tl_2Ba_2CuO_{6+\delta}$ with various T_C's from 0 to 73 K. *Physical Review B*, 42:10165–10171, 1990.

[24] M.R. Norman. Magnetic collective mode dispersion in high-temperature superconductors. *Physical Review B*, 63:092509, 2001.

[25] C.C. Tsuei, J.R. Kirtley, Z.F. Ren, J.H. Wang, H. Raffy, and Z.Z. Li. Pure $d_{x^2-y^2}$ order-parameter symmetry in the tetragonal superconductor $Tl_2Ba_2CuO_{6+\delta}$. *Nature*, 387:481–483, 1997.

[26] M. Platé et al. Fermi surface and quasiparticle excitations of overdoped Tl2201 by ARPES. *Physical Review Letters*, 95:077001, 2005.

[27] T. Yoshida, X.J. Zhou, T. Sasagawa, W.L. Yang, P.V. Bogdanov, A. Lanzara, Z. Hussain, T. Mizokawa, A. Fujimori, H. Eisaki, Z.-X. Shen, T. Kakeshita, and S. Uchida. Metallic behavior of lightly doped $La_{2-x}Sr_xCuO_4$ with a Fermi surface forming an arc. *Physical Review Letters*, 91:027001, 2003.

[28] X.J. Zhou, T. Yoshida, D.-H. Lee, W.L. Yang, V. Brouet, F. Zhou, W.X. Ti, J.W. Xiong, Z.X. Zhao, T. Sasagawa, T. Kakeshita, H. Eisaki, S. Uchida, A. Fujimori, Z. Hussain, and Z.-X. Shen. Dichotomy between nodal and antinodal quasiparticles in underdoped $(La_{2-x}Sr_x)CuO_4$ superconductors. *Physical Review Letters*, 92:187001, 2004.

[29] D.C. Peets, R. Liang, D.A. Bonn, W.N. Hardy, and M. Raudsepp. Growth of orthorhombic Tl-2201 single crystals by the self-flux method. *not published*, cond-mat:0211028v1, 2002.

[30] D.C. Peets et al. $Tl_2Ba_2CuO_{6+\delta}$ brings spectroscopic probes deep into the overdoped regime of the high-T_C cuprates. *New Journal of Physics*, 9:1–32, 2007.

[31] O.K. Andersen. Linear methods in band theory. *Physical Review B*, 12:3060, 1975.

[32] D.J. Singh and W.E. Pickett. Electronic characteristics of $Tl_2Ba_2CuO_6$—Fermi surface, positron wavefunction, electric field gradients, and transport parameters. *Physica C*, 203:193–202, 1992.

[33] S. Sahrakorpi, H. Lin, R.S. Markiewicz, and A. Bansil. Effect of hole doping on the electronic structure of Tl2201. *Physica C*, 460–462:428–429, 2007.

[34] H. Lin, S. Sahrakorpi, R.S. Markiewicz, and A. Bansil. Raising Bi-O bands above the Fermi energy level of hole-doped $Bi_2Sr_2CaCu_2o_{8+\delta}$ and other cuprate superconductors. *Physical Review Letters*, 96:097001, 2006.

[35] J.C. Campuzano, M.R. Norman, and M. Randeria. *Photoemission in the High-T_C Superconductors, Volume II*. Springer, Berlin, 2004.

[36] A.P. Mackenzie, S.R. Julian, D.C. Sinclair, and C.T. Lin. Normal-state magnetotransport in superconducting $Tl_2Ba_2CuO_{6+\delta}$ to millikelvin temperatures. *Physical Review B*, 53:5848–5855, 1996.

[37] T. Mishonov and M. Stoev. LCAO model for 3D Fermi surface of high-T_C cuprate $Tl2Ba_2CuO_{6+\delta}$. *Preprint*, condmat:0504290, 2006.

[38] O.K. Andersen, A.I. Liechtenstein, O. Jepsen, and F. Paulsen. LDA energy bands, low-energy hamiltonians, t',t'',$t_\perp(k)$, and j. *Journal of Physics and Chemistry of Solids*, 56:1573–1591, 1995.

[39] M.R. Norman, H. Ding, M. Randeria, J.C. Campuzano, T. Yokoya, T. Takeuchi, T. Takahashi, T. Mochiku, K. Kadowaki, P. Guptasarma, and D.G. Hinks. Destruction of the Fermi surface in underdoped high-T_C superconductors. *Nature*, 392:157–160, 1998.

[40] J. Mesot, M. Randeria, M.R. Norman, A. Kaminski, H.M. Fretwell, J.C. Campuzano, H. Ding, T. Takeuchi, T. Sato, T. Yokoya, T. Takahashi, I. Chong, T. Terashima, M. Takano, T. Mochiku, and K. Kadowaki. Determination of the Fermi surface in high T_c superconductors by angle-resolved photoemission spectroscopy. *Physical Review B*, 63:224516, 2001.

[41] A. Kanigel et al. Evolution of the pseudogap from Fermi arcs to the nodal liquid. *Nature Physics*, 2:447–451, 2006.

[42] H. Ding, M.R. Norman, J.C. Campuzano, M. Randeria, A.F. Bellman, T. Yokoya, T. Takahashi, T. Mochiku, and K. Kadowaki. Angle-resolved photoemission spectroscopy study of the superconducting gap anisotropy in $Bi_2Sr_2Ca_1Cu_2O_{8+\delta}$. *Physical Review B*, 54:9678, 1996.

[43] H. Matsui, T. Sato, S.-C. Wang, H.-B. Yang, H. Ding, T. Fujii, T. Watanabe, and A. Matsuda. BCS-like Bogoliubov quasiparticles in high-T_C superconductors observed by angle-resolved photoemission spectroscopy. *Physical Review Letters*, 90:217002, 2003.

[44] D.L. Feng, A. Damascelli, K.M. Shen, N. Motoyama, D.H. Lu, H. Eisaki, K. Shimizu, J.-I. Shimoyama, K. Kishio, N. Kaneko, M. Greven, G.D. Gu, X.J. Zhou, C. Kim, F. Ronning, N.P. Armitage, and Z.-X. Shen. Electronic structure of the trilayer cuprate superconductor $Bi_2Sr_2Ca_2Cu_3O_{10+\delta}$. *Physical Review Letters*, 88:107001, 2002.

[45] N.J.C. Ingle et al. Quantitative analysis of Sr_2RuO_4 angle-resolved photoemission spectra: many-body interactions in a model Fermi liquid. *Physical Review B*, 72:205114, 2005.

[46] A. Damascelli, D.H. Lu, and Z.-X. Shen. From Mott insulator to overdoped superconductor: evolution of the electronic structure of cuprates studied by ARPES. *Journal of Electron Spectroscopy and Related Phenomena*, 117–118:165–187, 2001.

[47] X.J. Zhou, T. Cuk, T. Devereaux, N. Nagaosa, and Z.-X. Shen. *Handbook of High-Temperature Superconductivity: Theory and Experiment*, chapter Angle-resolved photoemission spectroscopy on electronic structure and electron-phonon coupling in cuprate superconductors. Springer, Berlin, 2007.

[48] A. Kaminski, S. Rosenkranz, H.M. Fretwell, J. Mesot, M. Randeria, J.C. Campuzano, M.R. Norman, Z.Z. Li, H. Raffy, T. Sato, T. Takahashi, and K. Kadowaki. Identifying the background signal in angle-resolved photoemission spectra of high-tempertature cuprate superconductors. *Physical Review B*, 69:212509, 2004.

[49] K. Yang et al. Normal-state electronic structure in the heavily overdoped regime of $Bi_{1.74}Pb_{0.38}Sr_{1.88}CuO_{6+\delta}$ single-layer cuprate superconductors. *Physical Review B*, 73:144507, 2006.

[50] C.C. Tsuei and J.R. Kirtley. Pairing symmetry in cuprate superconductors. *Review of Modern Physics*, 72:969–1016, 2000.

[51] A. Kaminski et al. Momentum anisotropy of the scattering rate in cuprate superconductors. *Physical Review B*, 71:014517, 2005.

[52] K.M. Shen et al. Nodal quasiparticles and antinodal charge ordering in $Ca_{2-x}Na_xCuO_2Cl_2$. *Science*, 307:901–904, 2005.

[53] A.P. Mackenzie, S.R. Julian, A.J. Diver, G.J. McMullan, M.P. Ray, G.G. Lonzarich, Y. Maeno, S. Nishizaki, and T. Fujita. Quantum oscillations in the layered perovskite superconductor Sr_2RuO_4. *Physical Review Letters*, 76:3786–9, 1996.

[54] C. Bergemann, S.R. Julian, A.P. Mackenzie, S. Nishizaki, and Y. Maeno. Detailed topography of the Fermi surface of Sr_2RuO_4. *Physical Review Letters*, 84:2662–5, 2000.

[55] A. Damascelli, D.H. Lu, K.M. Shen, N.P. Armitage, R. Ronning, D.L. Feng, C. Kim, and Z.-X. Shen. Fermi surface, surface states and surface reconstruction in Sr_2RuO_4. *Physical Review Letters*, 85:5194–5197, 2000.

[56] A. Liebsch. Fermi surface, surface states and surface reconstruction in Sr_2RuO_4. *Physical Review Letters*, 87:239701, 2000.

[57] A. Damascelli, K.M. Shen, D.H. Lu, and Z.-X. Shen. Fermi surface, surface states and surface reconstruction in Sr_2RuO_4. *Physical Review Letters*, 87:239702, 2001.

[58] K.M. Shen et al. Surface electronic structure of Sr_2RuO_4. *Physical Review B (Rapid Commun.)*, 64:180502 (R), 2001.

[59] M. Abdel-Jawad, M.P. Kennett, L. Balicas, A. Carrington, A.P. Mackenzie, R.H. McKenzie, and N.E. Hussey. Anisotropic scattering and anomalous transport in a high-temperature superconductor. *Nature Physics*, 2:821, 2006.

[60] J.A. Slezak and J.C. Davis. Invited talk within the focused session, "The electronic properties of overdoped cuprates: The clean gateway to high-T_C superconductivity.

[61] J.E. Hoffman, K. McElroy, D.-H. Lee, K.M. Lang, H. Eisaki, S. Uchida, and J.C. Davis. Imaging quasiparticle interference in $Bi_2Sr_2CaCu_2O_{8+\delta}$. *Science*, 297:1148–1151, 2002.

[62] N. Gedik, M. Langner, J. Orenstein, S. Ono, Y. Abe, and Y. Ando. Abrupt transition in quasiparticle dynamics at optimal doping in a cuprate superconductor system. *Physical Review Letters*, 95:117005, 2005.

[63] F. Carbone et al. Doping dependence of the redistribution of optical spectral weight in $Bi_2Sr_2CaCu_2O_{8+\delta}$. *Physical Review B*, 74:064510, 2006.

[64] Y.C. Ma and N.L. Wang. Infrared scattering rate of overdoped $Tl_2Ba_2CuO_{6+\delta}$. *Physical Review B*, 73:144503, 2006.

[65] E. Abrahams and C.M. Varma. What angle-resolved photoemission experiments tell about the microscopic theory for high-temperature superconductors. *Proceedings of the National Academy of Sciences of the United States of America*, 97:5714–5716, 2000.

[66] L. Zhu, P.J. Hirschfeld, and D.J. Scalapino. Elastic forward scattering in the cuprate superconducting state. *Physical Review B*, 70:214503, 2004.

[67] K. Wakabayashi, T.M. Rice, and M. Sigrist. Enhanced coherence of antinodal quasiparticles in a dirty d-wave superconductor. *Physical Review B*, 72:214517, 2005.

[68] M. Vojta, Y. Zhang, and S. Sachdev. Quantum phase transitions in d-wave superconductors. *Physical Review Letters*, 85:4940–4943, 2000.

[69] A. Kopp, A. Ghosal, and S. Chakravaty. Competing ferromagnetism in high-temperature copper oxide superconductors. *Proceedings of the National Academy of Sciences of the United States of America*, 104:6123–6127, 2007.

[70] R.-H. He et al. Hidden itinerant-spin phase in heavily overdoped $La_{2-x}Sr_xCuO_4$ superconductors revealed by dilute Fe doping: A combined neutron scattering and angle-resolved photoemission study. *Physical Review Letters*, 107:127002, 2011.

[71] J.L. Tallon and J.W. Loram. The doping dependence of T^*—what is the real high-T_C phase diagram? *Physica C*, 349:53–68, 2001.

[72] S. Sahrakorpi, M. Lindroos, R.S. Markiewicz, and A. Bansil. Evolution of midgap states and residual three dimensionality in $La_{2-x}Sr_xCuO_4$. *Physical Review Letters*, 95:157601, 2005.

[73] A. Bansil, M. Lindroos, S. Sahrakorpi, and R.S. Markiewicz. Influence of the third dimension of quasi-two-dimensional cuprate superconductors on angle-resolved photoemission spectra. *Physical Review B*, 71:012503, 2005.

[74] S.H. Pan, J.P. O'Neal, R.L. Badzey, C. Chamon, H. Ding, J.R. Engelbrecht, Z. Wang, H. Eisaki, S. Uchida, A.K. Gupta, K.-W. Ng, W.E. Hudson, K.M. Lang, and J.C. Davis. Microscopic electric inhomogeneity in the high-T_C superconductor $Bi_2Sr_2Ca_1Cu_2O_{8+x}$. *Nature*, 413:282–285, 2001.

[75] M.C. Schabel et al. Angle-resolved photoemission on untwinned $YBa_2Cu_3O_{6.95}$. I. Electronic structure and dispersion relations of surface and bulk bands. *Physical Review B*, 57:6090–6106, 1998.

[76] D.H. Lu et al. Superconducting gap and strong in-plane anisotropy in untwinned $YBa_2Cu_3O_{7-\delta}$. *Physical Review Letters*, 86:4370–4374, 2001.

[77] V.B. Zablotnyy et al. Momentum and temperature dependence of renormalization effects in the high-temperature superconductor $YBa_2Cu_3O_{7-\delta}$. *Physical Review B*, 76:064519, 2007.

[78] F.F. Balakirev et al. Fermi surface reconstruction at optimum doping in high-T_C superconductors. *preprint*, arxiv.org/abs:0710.4612, 2007.

[79] I. Elfimov, G. Sawatzky, and A. Damascelli. Fermi pockets and correlation effects in underdoped $YBa_2Cu_3O_{6.5}$. *Physical Review B*, 77:060504(R), 2008.

[80] A. Carrington and E.A. Yelland. Band-structure calculations of Fermi-surface pockets in ortho-II $YBa_2Cu_3O_{6.5}$. *Physical Review B*, 76:140508(R), 2007.

[81] N. Harrison, R.D. McDonald, and J. Singleton. Cuprate Fermi orbits and Fermi arcs: The effect of short-range antiferromagnetic order. *Physical Review Letters*, 99:205406, 2007.

[82] W.-Q. Chen, K.-Y. Yang, T.M. Rice, and F.C. Zhang. Quantum oscillations in magnetic field induced antiferromagnetic phase of underdoped cuprates: Application to ortho-II $YBa_2Cu_3O_{6.5}$. *Europhysics Letters*, 82:17004, 2008.

[83] A.J. Millis and M. Norman. Antiphase stripe order as the origin of electron pockets observed in 1/8 hole-doped cuprates. *Physical Review B*, 76:220503(R), 2007.

[84] S. Chakravarty and H.-Y. Kee. Fermi pockets and quantum oscillations of the Hall coefficient in high-temperature superconductors. *Proceedings of the National Academy of Sciences of the United States of America*, 105:8835–8839, 2008.

[85] A.S. Alexandrov. Theory of quantum magneto-oscillations in underdoped cuprate superconductors. *Journal of Physics: Condensed Matter*, 20:192202, 2008.

[86] A. Melikyan and O. Vafek. Quantum oscillations in the mixed state of d-wave superconductors. *Physical Review B*, 78:020502(R), 2008.

[87] R. Hesper, L.H. Tjeng, A. Heeres, and G. Sawatzky. Photoemission evidence of electronic stabilization of polar surfaces in K_3C_{60}. *Physical Review B*, 62:16040–16055, 2000.

[88] D.J. Derro et al. Nanoscale one-dimensional scattering resonances in the CuO chains of $YBa_2Cu_3O_{6+x}$. *Physical Review Letters*, 88:097002, 2002.

[89] R. Liang, D.A. Bonn, and W.N. Hardy. Evaluation of CuO_2 plane hole doping in $YBa_2Cu_3O_{6+x}$ single crystals. *Physical Review B*, 73:180505, 2006.

[90] T. Kondo et al. Dual character of the electronic structure of $YBa_2Cu_4O_8$: The conduction bands of CuO_2 planes and CuO chains. *Physical Review Letters*, 98:157002, 2007.

[91] T. Ohta, A. Bostwick, T. Seyller, K. Horn, and E. Rotenberg. Controlling the electronic structure of bilayer graphene. *Science*, 313:951–954, 2006.

[92] O.P. Sushkov, G.A. Sawatzky, R. Eder, and H. Eskes. Hole photoproduction in insulating copper oxide. *Physical Review B*, 56:11769–11776, 1997.

[93] H. Eskes and R. Eder. Hubbard model versus t–J model: The one-particle spectrum. *Physical Review B*, 54:14226–14229, 1996.

[94] F. Reinert, G. Nicolay, S. Schmidt, D. Ehm, and S. Hüfner. Direct measurements of the $l-$gap surface states on the (1 1 1) face of noble metals by photoelectron spectroscopy. *Physical Review B*, 63:115415, 2001.

[95] P. Heimann, H. Neddermeyer, and Roloff H.F. Ultraviolet photoemission from intrinsic surface states of the noble metals. *Journal of Physics C: Solid State Physics*, 10:L17, 1977.

[96] S.D. Kevan and Gaylord R.H. High-resolution photoemission study of the electronic structure of the noble-metal (1 1 1) surfaces. *Physical Review B*, 36:5809, 1987.

[97] R. Paniago, R. Matzdorf, G. Meister, and A. Goldmann. Temperature dependence of Shockley-type surface energy bands on Cu(1 1 1), Ag(1 1 1) and Au(1 1 1). *Surface Science*, 336:122, 1995.

[98] J.H. Moore, C.C. Davis, and M.A. Coplan. *Building Scientific Apparatus*. Perseus Books, Cambridge, Massachusetts, 2003.

[99] A.L. Fetter and J.D. Walecka. *Theoretical Mechanics of Particles and Continua*. McGraw Hill, New York, 1980.

[100] D.C. Jiles. *Introduction to Magnetism and Magnetic Materials*. CRC Press, Boca Raton, Florida, 1998.

[101] R.H. Todd, D.K. Allen, and L. Alting. *Fundamental Principles of Manufacturing Processes*. Industrial Press, New York, 1994.

[102] R.H. Todd, D.K. Allen, and L. Alting. *Manufacturing Processes Reference Guide*. Industrial Press, New York, 1994.

[103] C. Dürr et al. Angle-resolved photoemission spectroscopy of $Sr_2CuO_2Cl_2$. *Physical Review B*, 63:014505, 2000.

[104] R.L. Powell and W.A. Blanpied. *Thermal Conductivity of Metals and Alloys at Low Temperatures*. U.S. Government Printing Office, Washington, D.C., 1954.

[105] L.J. Salerno and P. Kittel. *Handbook for Cryogenic Engineering*, chapter Thermal Contact Conductance. Taylor and Francis, London, 1998.

[106] L.J. Salerno, P. Kittel, and A.L. Spivak. Thermal conductance of pressed OFHC copper contacts at liquid helium temperatures. In *Thermal Conductivity 18, Proceedings of the 18th International Thermal Conductivity Conference*, 1984.

[107] D. Halliday, R. Resnick, and J. Walker. *Fundamentals of Physics, 5^{th} Edition*. John Wiley and Sons, Hoboken, New Jersey, 1997.

[108] T.H.K. Frederking, Y.C. Wu, and B.W. Clement. Effects of interfacial instability on film boiling of saturated liquid helium I above a horizontal surface. *American Institute of Chemical Engineers Journal*, 12:238–244, 1966.

[109] R. Berman. Some experiments on thermal contact at low temperatures. *Journal of Applied Physics*, 27:318, 1956.

[110] R.J. Corruccini and J.J. Gniewek. *Thermal Expansion of Technical Solids at Low Temperatures*. U.S. Government Printing Office, Washington, D.C., 1961.

[111] NTN Corporation. *Ball and Roller Bearings*. NTN Corporation, Osaka, Japan, 1995.

[112] T.M. Crandell. *CNC Machining and Programming: An Introduction, 2^{nd} Edition*. Industrial Press, New York, 2003.

[113] E. Oberg, F.D. Jones, H.L. Horton, and H.H. Ryffell. *Machinery's Handbook, 26^{th} Edition*. Industrial Press, New York, 2000.

[114] J.R. Davis. *Concise Metals Engineering Data Book*. ASM International, Materials Park, Ohio, 1997.

[115] C.W. Kennedy, E.G. Hoffman, and S. Bond. *Inspection and Gaging*. Industrial Press, New York, 1987.

[116] B. Dasgupta and T.S. Mruthyunjaya. The Stewart platform manipulator: a review. *Mechanism and Machine Theory*, 35:15–40, 2000.

[117] P.A.P. Lindberg, Z.-X. Shen, D.S. Dessau, B.O. Wells, D.B. Mitzi, I. Lindau, W.E. Spicer, and A. Kapitulnik. Energy dispersions of single-crystalline $Bi_{2.0}Sr_{1.8}Ca_{0.8}La_{0.3}Cu_{2.1}O_{8+\delta}$ superconductors determined using angle-resolved photelectron spectroscopy. *Physical Review B*, 40:5169–5171, 1989.

[118] Janis Research Company. ST-400 ultra high vacuum cryostat. Janis product information is found at www.janis.com. The company is located at 2

Jewel Drive, Wilmington, Massachusetts, +1 978 657-8750, 2010. The ST-400 is non-magnetic, is ultra-high-vacuum compatible, and can be cooled below 2K.